Applied Computational Electromagnetics Society

Journal

December 2012

Vol. 27 No. 12

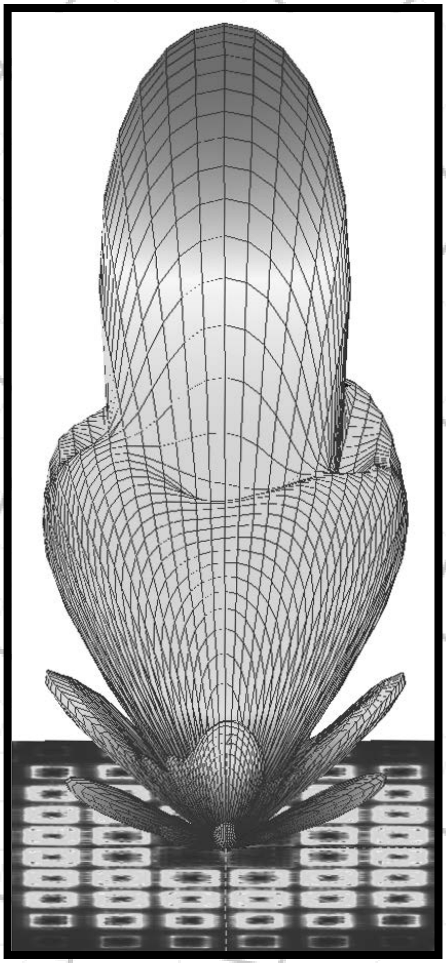

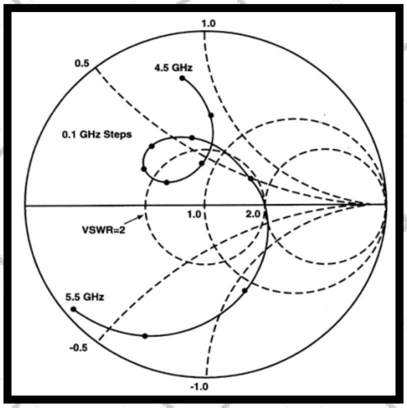

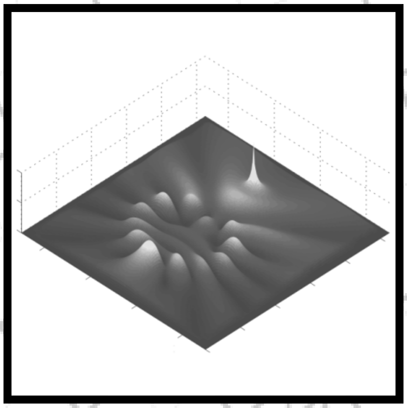

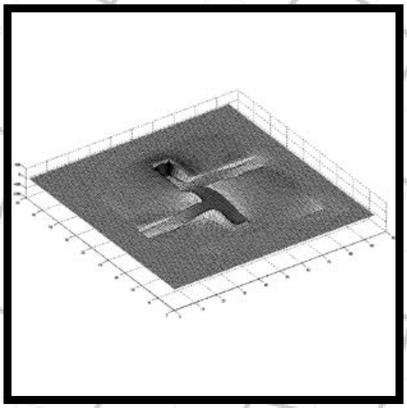

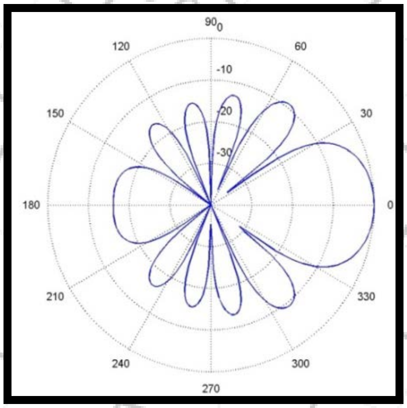

ISSN 1054-4887

GENERAL PURPOSE AND SCOPE: The Applied Computational Electromagnetics Society ***(ACES)*** Journal hereinafter known as the ***ACES Journal*** is devoted to the exchange of information in computational electromagnetics, to the advancement of the state-of-the art, and the promotion of related technical activities. The primary objective of the information exchange is to inform the scientific community on the developments of new computational electromagnetics tools and their use in electrical engineering, physics, or related areas. The technical activities promoted by this publication include code validation, performance analysis, and input/output standardization; code or technique optimization and error minimization; innovations in solution technique or in data input/output; identification of new applications for electromagnetics modeling codes and techniques; integration of computational electromagnetics techniques with new computer architectures; and correlation of computational parameters with physical mechanisms.

SUBMISSIONS: The ***ACES Journal*** welcomes original, previously unpublished papers, relating to applied computational electromagnetics. Typical papers will represent the computational electromagnetics aspects of research in electrical engineering, physics, or related disciplines. However, papers which represent research in applied computational electromagnetics itself are equally acceptable.

Manuscripts are to be submitted through the upload system of ***ACES*** web site http://aces.ee.olemiss.edu See "Information for Authors" on inside of back cover and at ***ACES*** web site. For additional information contact the Editor-in-Chief:

Dr. Atef Elsherbeni
Department of Electrical Engineering
The University of Mississippi
University, MS 386377 USA
Phone: 662-915-5382
Email: atef@olemiss.edu

SUBSCRIPTIONS: All members of the Applied Computational Electromagnetics Society are entitled to access and download the ***ACES Journal*** any published journal article available at http://aces.ee.olemiss.edu. Printed issues of the ***ACES Journal*** are delivered to institutional members. Each author of published papers receives a printed issue of the ***ACES Journal*** in which the paper is published.

Back issues, when available, are $50 each. Subscription to ***ACES*** is through the web site. Orders for back issues of the ***ACES Journal*** and change of address requests should be sent directly to ***ACES*** office at:

Department of Electrical Engineering
The University of Mississippi
University, MS 386377 USA
Phone: 662-915-7231
Email: aglisson@olemiss.edu

Allow four weeks advance notice for change of address. Claims for missing issues will not be honored because of insufficient notice, or address change, or loss in the mail unless the ***ACES*** office is notified within 60 days for USA and Canadian subscribers, or 90 days for subscribers in other countries, from the last day of the month of publication. For information regarding reprints of individual papers or other materials, see "Information for Authors".

LIABILITY. Neither ***ACES***, nor the ***ACES Journal*** editors, are responsible for any consequence of misinformation or claims, express or implied, in any published material in an ***ACES Journal*** issue. This also applies to advertising, for which only camera-ready copies are accepted. Authors are responsible for information contained in their papers. If any material submitted for publication includes material which has already been published elsewhere, it is the author's responsibility to obtain written permission to reproduce such material.

APPLIED COMPUTATIONAL ELECTROMAGNETICS SOCIETY JOURNAL

December 2012
Vol. 27 No. 12
ISSN 1054-4887

The ACES Journal is abstracted in INSPEC, in Engineering Index, DTIC, Science Citation Index Expanded, the Research Alert, and to Current Contents/Engineering, Computing & Technology.

The illustrations on the front cover have been obtained from the research groups at the Department of Electrical Engineering, The University of Mississippi.

THE APPLIED COMPUTATIONAL ELECTROMAGNETICS SOCIETY
http://aces.ee.olemiss.edu

EDITOR-IN-CHIEF

Atef Elsherbeni
University of Mississippi, EE Dept.
University, MS 38677, USA

ASSOCIATE EDITORS-IN-CHIEF

Sami Barmada
University of Pisa. EE Dept.
Pisa, Italy, 56126

Fan Yang
University of Mississippi, EE Dept.
University, MS 38677, USA

Mohamed Bakr
McMaster University, ECE Dept.
Hamilton, ON, L8S 4K1, Canada

Yasushi Kanai
Niigata Inst. of Technology
Kashiwazaki, Japan

Mohammed Hadi
Kuwait University, EE Dept.
Safat, Kuwait

Mohamed Abouzahra
MIT Lincoln Laboratory
Lexington, MA, USA

Alistair Duffy
De Montfort University
Leicester, UK

EDITORIAL ASSISTANTS

Matthew J. Inman
University of Mississippi, EE Dept.
University, MS 38677, USA

Anne Graham
University of Mississippi, EE Dept.
University, MS 38677, USA

EMERITUS EDITORS-IN-CHIEF

Duncan C. Baker
EE Dept. U. of Pretoria
0002 Pretoria, South Africa

Allen Glisson
University of Mississippi, EE Dept.
University, MS 38677, USA

David E. Stein
USAF Scientific Advisory Board
Washington, DC 20330, USA

Robert M. Bevensee
Box 812
Alamo, CA 94507-0516, USA

Ahmed Kishk
University of Mississippi, EE Dept.
University, MS 38677, USA

EMERITUS ASSOCIATE EDITORS-IN-CHIEF

Alexander Yakovlev
University of Mississippi, EE Dept.
University, MS 38677, USA

Erdem Topsakal
Mississippi State University, EE Dept.
Mississippi State, MS 39762, USA

EMERITUS EDITORIAL ASSISTANTS

Khaled ElMaghoub
University of Mississippi, EE Dept.
University, MS 38677, USA

Mohamed Al Sharkawy
Arab Academy for Science and
Technology, ECE Dept.
Alexandria, Egypt

Christina Bonnington
University of Mississippi, EE Dept.
University, MS 38677, USA

DECEMBER 2012 REVIEWERS

Ahmed Abdelrahman
Shuaib Ahmed
Shirook Ali
Ahmed Attiya
Mohamed Bakr
Sami Barmada
Said El-Khamy
Christophe Fumeaux
Josefa Gomez
Mourad Ibrahim
Haixin Liu
Zahéra Mekkioui
Antonino Musolino
Alain Reineix
Binay Sarkar
Morteza Shahpari
Margarita Tecpoyotl-Torres

THE APPLIED COMPUTATIONAL ELECTROMAGNETICS SOCIETY

JOURNAL

Vol. 27 No. 12 December 2012

TABLE OF CONTENTS

A Hybrid 3DMLUV-ACA Method for Scattering from a 3-D PEC Object above a 2-D Gaussian Dielectric Rough Surface

C. Li[1], S. Y. He[1], G. Q. Zhu[1], Z. Zhang[2], F. S. Deng[3], B.X Xiao[4]

[1] School of Electronic Information
Wuhan University, Wuhan, 430079, China
whunpredestiny@gmail.com, siyuanhi@gmail.com, gqzhu@whu.edu.cn

[2] HuaZhong Agricultural University, Wuhan Hubei 430079, China
zhangzhe203@163.com

[3] Wuhan Maritime Communication Research Institute, Wuhan Hubei 430079, China
dengfs2009@gmail.com

[4] Geophysics Engineering Center, Chang Jiang University, Jingzhou Hubei 434023, China
npredestiny@yahoo.com

Abstract**—** The bistatic electromagnetic scattering from the composite model of a three-dimensional (3-D) arbitrarily shaped object located above a two -dimensional (2-D) Gaussian rough surface is analyzed in this work. The object suited above is assumed to be a perfect electric conductor (PEC) while the rough surface is dielectric. Firstly, the Poggio, Miller, Chang, Harrington, Wu and Tsai (PMCHWT) integral equations, electric field integral equation (EFIE) are implemented and extended on the rough surface and on the surface of the object respectively. Then, the method of moments (MoM) combined with Galerkin method is introduced to discretize the integral equations to the matrix form using RWG basis function. Due to the memory requirement and computational complexity of traditional MOM are $O(N^2)$ (N is the number of unknowns), the rank based 3-D Multilevel UV method (3DMLUV) is employed to reduce memory and CPU time overhead. The 3DMLUV has been successfully applied in the scattering of PEC targets, however, when the object or rough surface become dielectric, the fast fill-in method proposed in Reference [19] often breaks down due to the oscillatory nature of the gradient of Green's function. Therefore, the ACA is applied to speed up the filling of the impedance entries required in 3DMLUV because of its algebraic nature. The efficiency and accuracy of the proposed method are demonstrated in a variety of scattering problems.

Index Terms - Composite model, bistatic scattering, PMCHWT, 3DMLUV, ACA

I. INTRODUCTION

Electromagnetic (EM) scattering from an object above a rough surface has attracted much interest during recent years, because of its extensive applications to remote sensing, target recognition, radar surveillance and so on [1-7]. MoM has been widely used to numerically simulate scattering from composite model of the object and the underlying rough surface. Yet, after discretized with basis function and tested, the conventional MoM results in a dense impedance matrix. Consequently, the storage, impedance matrix fill-in, and matrix-vector multiplication operations are of $O(N^2)$ complexity, where N is the number of unknowns. To overcome these disadvantages, a number of techniques have been successfully developed to dramatically reduced memory and computational cost with the iterative solution of surface integral equations (SIEs), such as Multilevel fast multipole method (MLFMM) [8-11,13], the adaptive integral method (AIM) [12]. The mathematical basis of MLFMM algorithm is addition theorem. By the addition theorem, the dyadic Green function can be represented in a

Submitted On: Nov. 1, 2011
Accepted On: Oct. 8, 2012

formula in which the observation point and source point are separate. Based on the formula, MLFMM has succeeded in reducing the numerical complexity of memory to $O(N)$ and CPU time to $O(N\log N)$. AIM is FFT-based and for volume integral equations (VIE), it achieve the complexity of $O(N\log N)$.

In this paper, we present an accurate method of moments (MoM) solution of the PMCHWT and EFIE surface integral equations for scattering by 3-D, arbitrarily shaped, homogeneous objects above a 2-D rough surface using hybrid 3DMLUV-ACA method. The object is assumed to be a perfect electric conductor while the rough surface is characterized with Gaussian statistics for surface height and for surface autocorrelation function.

The 3DMLUV method is developed by Deng using EM-interaction-based sampling algorithm. It is an efficient technique to analyze large scale scattering problems and show a computation complexity of $O(N\log N)$. The details of the 3DMLUV can be found in[5,19]. However, before the EM-interaction-based sampling algorithm is used, the original far-field interaction submatrix must be given. When the object or rough surface becomes dielectric, the fast setup method proposed in Reference [19] fails due to the oscillatory nature of the gradient of Green's function. The ACA method [14-16] is purely algebraic; hence, its implementation is integral equation kernel (the gradient of Green's function) independent. Therefore, the ACA method is a perfect choice to speed up the filling of the impedance entries required in 3DMLUV.

The remainder of the paper is organized as follows. In section Ⅱ, we present the implementation of the PMCHWT and EFIE integral equations. The Galerkin method is utilized, where RWG functions are used as both basis and testing functions. The 3DMLUV-ACA is briefly presented. In section Ⅲ, the numerical results are shown, the accuracy of the proposed method is validated first. Finally, bistatic radar cross-section (RCS) of the object/rough surface and difference radar cross-section (d-RCS) [21] of the object are calculated. The influence of the rough surface root mean square (RMS) height, the medium permittivity and the altitude of the object on the scattering characteristic are investigated.

The time factor $\exp(j\omega t)$ is used in this paper and will be suppressed below.

II. THEORY

A. MoM formulation of PMCHWT and EFIE integral equation

As shown in Fig. 1, a 3-D object (PEC) is located above a 2-D random rough surface (Dielectric) and the tapered wave ($\boldsymbol{E}_i$, $\boldsymbol{H}_i$) is employed to avoid rough surface edge scattering effects [22].

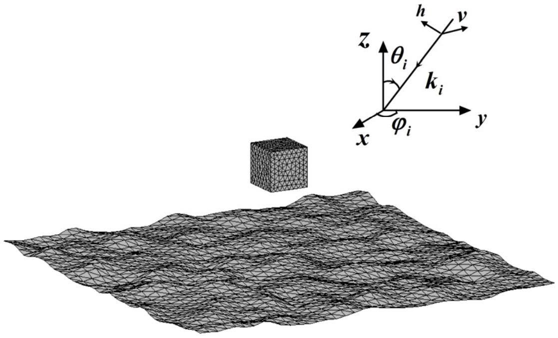

Fig. 1. Composite scattering model of target and rough surface.

The air space, the space object occupied and the space under rough surface are denoted by Region0, Region1 and Region2 while the surface of the object and the rough surface are indicated as S_1 and S_2. The three regions have permittivity and permeability given by ε_0 and μ_0, ε_1 and μ_1, ε_2 and μ_2, respectively. The electric and magnetic fields in Region 0, Region1 and Region2 are $\boldsymbol{E}_0, \boldsymbol{H}_0, \boldsymbol{E}_1, \boldsymbol{H}_1$ and $\boldsymbol{E}_2, \boldsymbol{H}_2$. Since the object is assumed to be PEC, $\boldsymbol{E}_1, \boldsymbol{H}_1$ are all equal to zero.

Using the surface equivalence theorem, the equivalent electric and magnetic current on rough surface and the surface of objects are $\boldsymbol{J}_s, \boldsymbol{M}_s, \boldsymbol{J}_o$ respectively. So the electric and magnetic fields at an arbitrary point $\boldsymbol{r}$ in Region 0 are

$$\begin{aligned}\boldsymbol{E}_0(\boldsymbol{r}) &= \mathrm{Z}_0\boldsymbol{L}_0(\boldsymbol{J}_s) - \boldsymbol{K}_0(\boldsymbol{M}_s)\\ &+\mathrm{Z}_0\boldsymbol{L}_0(\boldsymbol{J}_o) + \boldsymbol{E}_i(\boldsymbol{r})\end{aligned}, \tag{1a}$$

$$\begin{aligned}\boldsymbol{H}_0(\boldsymbol{r}) &= \frac{1}{\mathrm{Z}_0}\boldsymbol{L}_0(\boldsymbol{M}_s) + \boldsymbol{K}_0(\boldsymbol{J}_s)\\ &+ \boldsymbol{K}_0(\boldsymbol{J}_o) + \boldsymbol{H}_i(\boldsymbol{r})\end{aligned}. \tag{1b}$$

Similarly, the electric and magnetic fields in Region 2 are

$$\boldsymbol{E}_2(\boldsymbol{r}) = \mathrm{Z}_2\boldsymbol{L}_2(-\boldsymbol{J}_s) - \boldsymbol{K}_2(-\boldsymbol{M}_s)\,, \qquad (1c)$$

$$\boldsymbol{H}_2(\boldsymbol{r}) = \frac{1}{\mathrm{Z}_2}\boldsymbol{L}_2(-\boldsymbol{M}_s) + \boldsymbol{K}_2(-\boldsymbol{J}_s)\ , \qquad (1d)$$

where operators $\boldsymbol{L}$ and $\boldsymbol{K}$ are given by

$$\boldsymbol{L}_{0,2}(\boldsymbol{X}) = -jk\int[\boldsymbol{X} + \frac{1}{k^2}\nabla(\nabla\cdot\boldsymbol{X})]\mathrm{G}_{0,2}dS', \quad (2a)$$

$$\boldsymbol{K}_{0,2}(\boldsymbol{X}) = -\int \boldsymbol{X}\times\nabla\mathrm{G}_{0,2}dS'\ . \qquad (2b)$$

The vector $\boldsymbol{X}$ represents the surface electric current $\boldsymbol{J}$ and/or the surface magnetic current $\boldsymbol{M}$ on surface S_1 or on surface S_2. $\mathrm{G}_i = \exp(-jk_i\,|\boldsymbol{r}-\boldsymbol{r}'|)/4\pi\,|\boldsymbol{r}-\boldsymbol{r}'|$ is the Green function in homogeneous isotropic medium. $k_i = \omega\sqrt{\varepsilon_i\mu_i}$ is the wave number in Region i. Thus, by equating the tangential component of the electric field $\boldsymbol{E}_0$ to zero, on surface S_1, we get

$$\begin{aligned}&[\mathrm{Z}_0\boldsymbol{L}_0(\boldsymbol{J}_s) - \boldsymbol{K}_0(\boldsymbol{M}_s) + \mathrm{Z}_0\boldsymbol{L}_0(\boldsymbol{J}_o)]\,|_{\tan}\\ &= -\boldsymbol{E}_i(\boldsymbol{r})\,|_{\tan}\end{aligned}\ . \qquad (3a)$$

Then, upon equating the tangential component of the electric fields ($\boldsymbol{E}_0$ and $\boldsymbol{E}_2$) and magnetic fields ($\boldsymbol{H}_0$ and $\boldsymbol{H}_2$), on surface S_2, we get

$$\begin{aligned}&[\mathrm{Z}_0\boldsymbol{L}_0(\boldsymbol{J}_s) - \boldsymbol{K}_0(\boldsymbol{M}_s) + \mathrm{Z}_0\boldsymbol{L}_0(\boldsymbol{J}_o)\\ &+\mathrm{Z}_2\boldsymbol{L}_2(\boldsymbol{J}_s) - \boldsymbol{K}_2(\boldsymbol{M}_s)]\,|_{\tan} = -\boldsymbol{E}_i(\boldsymbol{r})\,|_{\tan}\end{aligned}, \qquad (3b)$$

$$\begin{aligned}&[\frac{1}{\mathrm{Z}_0}\boldsymbol{L}_0(\boldsymbol{M}_s) + \boldsymbol{K}_0(\boldsymbol{J}_s) + \boldsymbol{K}_0(\boldsymbol{J}_o)\\ &+\frac{1}{\mathrm{Z}_2}\boldsymbol{L}_2(\boldsymbol{M}_s) + \boldsymbol{K}_2(\boldsymbol{J}_s)]\,|_{\tan} = -\boldsymbol{H}_i(\boldsymbol{r})\,|_{\tan}\end{aligned}\ . \qquad (3c)$$

The equivalent electric and magnetic current $\boldsymbol{J}_s, \boldsymbol{M}_s, \boldsymbol{J}_o$ are approximated by using the RWG vector basis function $\boldsymbol{f}(\boldsymbol{r})$ [23] as follows:

$$\boldsymbol{J}_s(\boldsymbol{r}) = \sum_{n=1}^{P_1}\mathrm{I}_{1n}\boldsymbol{f}_{1n}(\boldsymbol{r})\,, \qquad (4a)$$

$$\boldsymbol{M}_s(\boldsymbol{r}) = \sum_{n=1}^{P_1}\mathrm{I}_{2n}\boldsymbol{f}_{1n}(\boldsymbol{r})\,, \qquad (4b)$$

$$\boldsymbol{J}_o(\boldsymbol{r}) = \sum_{m=1}^{P_2}\mathrm{I}_{3m}\boldsymbol{f}_{2m}(\boldsymbol{r})\ , \qquad (4c)$$

the P_1 and P_2 are the number of unknown coefficients. Upon applying Galerkin's method, the original integral equations are thus transformed into a set of linear equations given by:

$$\begin{bmatrix}\overline{\overline{\boldsymbol{Z}}}{}_{ss}^{EJ} & \overline{\overline{\boldsymbol{Z}}}{}_{ss}^{EM} & \overline{\overline{\boldsymbol{Z}}}{}_{os}^{EJ}\\ \overline{\overline{\boldsymbol{Z}}}{}_{ss}^{HJ} & \overline{\overline{\boldsymbol{Z}}}{}_{ss}^{HM} & \overline{\overline{\boldsymbol{Z}}}{}_{os}^{HJ}\\ \overline{\overline{\boldsymbol{Z}}}{}_{so}^{EJ} & \overline{\overline{\boldsymbol{Z}}}{}_{so}^{EM} & \overline{\overline{\boldsymbol{Z}}}{}_{oo}^{EJ}\end{bmatrix}\begin{bmatrix}\overline{\boldsymbol{I}}_1\\ \overline{\boldsymbol{I}}_2\\ \overline{\boldsymbol{I}}_3\end{bmatrix} = \begin{bmatrix}\overline{\boldsymbol{V}}{}_s^E\\ \overline{\boldsymbol{V}}{}_s^H\\ \overline{\boldsymbol{V}}{}_o^E\end{bmatrix}\ . \qquad (5)$$

where $\overline{\overline{\boldsymbol{Z}}}{}_{ss}^{EJ}$, $\overline{\overline{\boldsymbol{Z}}}{}_{ss}^{EM}$, $\overline{\overline{\boldsymbol{Z}}}{}_{ss}^{HJ}$, $\overline{\overline{\boldsymbol{Z}}}{}_{ss}^{HM}$ and $\overline{\overline{\boldsymbol{Z}}}{}_{oo}^{EJ}$ are the impedance submatrices of the rough surface and the object, respectively. The total impedance matrix is complicated by the interactions between the object and rough surface represented by $\overline{\overline{\boldsymbol{Z}}}{}_{os}^{EJ}$, $\overline{\overline{\boldsymbol{Z}}}{}_{os}^{HM}$ and $\overline{\overline{\boldsymbol{Z}}}{}_{so}^{EJ}$, $\overline{\overline{\boldsymbol{Z}}}{}_{so}^{EM}$. It should be pointed out that, not all of the nine submatrices will be calculated. By using the symmetrical relationship, only six of them will be calculated explicitly, which are $\overline{\overline{\boldsymbol{Z}}}{}_{ss}^{EJ}$, $\overline{\overline{\boldsymbol{Z}}}{}_{ss}^{EM}$, $\overline{\overline{\boldsymbol{Z}}}{}_{ss}^{HM}$, $\overline{\overline{\boldsymbol{Z}}}{}_{oo}^{EJ}$, $\overline{\overline{\boldsymbol{Z}}}{}_{so}^{EJ}$, $\overline{\overline{\boldsymbol{Z}}}{}_{so}^{EM}$. The Bicgstable [20] iterative method will be used to solve equation (5).

B. Tapered incident wave

The tapered incident wave is given by

$$\begin{aligned}\boldsymbol{E}_i &= \exp[-jk(z\cos\theta_i + x\sin\theta_i\cos\phi_i\\ &+y\sin\theta_i\sin\phi_i)\,(1+\omega)]\cdot\exp[-t_x - t_y]\end{aligned}, \qquad (6)$$

where

$$t_x = \frac{(x\cos\theta_i\cos\phi_i + y\cos\theta_i\sin\phi_i + z\sin\theta_i)^2}{g^2\cos^2\theta_i}, \qquad (7a)$$

$$t_y = \frac{(-x\sin\phi_i + y\cos\phi_i)^2}{g^2}\,, \qquad (7b)$$

$$\omega = \frac{1}{k^2}\left(\frac{2t_x - 1}{g^2\cos^2\theta_i} + \frac{2t_y - 1}{g^2}\right), \qquad (7c)$$

the θ_i, φ_i are incident angles and g is the tapering parameter. In order to avoid the rough surface edge scattering effects, g must be chosen deliberately with respect to the rough surface length. In this paper, g is taken as $g = L/4$.

C. The Calculation of the RCS and DRCS

Considering the approximation of the Green's function and the gradient of Green's function in the far field regions as:

$$G(\boldsymbol{r},\boldsymbol{r}^{'}) \approx \frac{\exp(-jkr)}{4r}\exp(jk(\boldsymbol{k}_s \cdot \boldsymbol{r}^{'})), \tag{8}$$

$$\nabla G(\boldsymbol{r},\boldsymbol{r}^{'}) \approx -jkG(\boldsymbol{r},\boldsymbol{r}^{'})\boldsymbol{k}_s. \tag{9}$$

Where

$\boldsymbol{k}_S = \boldsymbol{x}\sin\theta_s\cos\varphi_s + \boldsymbol{y}\sin\theta_s\sin\varphi_s + \boldsymbol{z}\cos\theta_s$, $\boldsymbol{r}$ and $\boldsymbol{r}^{'}$ are the field and source point. θ_s and φ_s are the scattering angles.

The scattered electric field $\boldsymbol{E}_s$ can be calculated by (1a) (after minusing the incident electric field), where the far field approximation (8) and (9) will be used. Defining the difference induced electric and magnetic current as $\boldsymbol{J}_{sd}$ and $\boldsymbol{M}_{sd}$ on the rough surface, the difference electric field can be calculated by:

$$\boldsymbol{E}_{sd}(\boldsymbol{r}) = \mathrm{Z}_0\boldsymbol{L}_0(\boldsymbol{J}_{sd}) - \boldsymbol{K}_0(\boldsymbol{M}_{sd}) + \mathrm{Z}_0\boldsymbol{L}_0(\boldsymbol{J}_o), \tag{10}$$

Then, the RCS σ and d-RCS σ_d can be given by:

$$\sigma = \lim_{r\to\infty} 4\pi r^2 \frac{|\boldsymbol{E}_s|^2}{|\boldsymbol{E}_i|^2}, \tag{11a}$$

$$\sigma_d = \lim_{r\to\infty} 4\pi r^2 \frac{|\boldsymbol{E}_{sd}|^2}{|\boldsymbol{E}_i|^2}. \tag{11b}$$

D. Fast fill-in method using ACA

When the bottom rough surface is dielectric, for surface integral equations (SIEs), there are two kinds of operators, i.e. the L operator and K operator. The 3DMLUV method fill in the submatrix elements of $\overline{\overline{Z}}^{sub}_{m\times n}$ with the fast method in [19]. Whereas in [19], the target are all assumed to be PEC. So they do not take the K operator into consideration. After discretized by RWG basis function and tested using Galerkin method, the K operator in submatrix $\overline{\overline{\boldsymbol{Z}}}^{EM}_{ss}$ is as follow:

$$\begin{aligned}[\overline{\overline{\boldsymbol{Z}}}^{EM}_{ss}]_{m,n} = -(&\frac{l_m}{2}\boldsymbol{\rho}_m^{+}(\boldsymbol{r}_m^{c+})\cdot\boldsymbol{H}_{mn}(\boldsymbol{r}_m^{c+}) \\ &+\frac{l_m}{2}\boldsymbol{\rho}_m^{-}(r_m^{c-})\cdot\boldsymbol{H}_{mn}(\boldsymbol{r}_m^{c-}))\end{aligned}, \tag{13}$$

$$\boldsymbol{H}_{mn}(\boldsymbol{r}_m^{c\pm}) = \int \boldsymbol{f}_n(r^{'})\times\nabla G(\boldsymbol{r}_m^{c\pm},\boldsymbol{r}^{'})ds^{'}, \tag{14}$$

where all the symbols have the same meaning as in [23]. Then the normalized area coordinate [23] is introduced to calculate $\boldsymbol{H}_{mn}(\boldsymbol{r}_m^{c\pm})$.

$$\begin{aligned}&\boldsymbol{H}_{mn}(\boldsymbol{r}_m^{c\pm}) = \int \boldsymbol{f}_n(\boldsymbol{r}^{'})\times\nabla G(\boldsymbol{r}_m^{c\pm},\boldsymbol{r}^{'})ds^{'} \\ &= l_n\int(\xi^{'}\boldsymbol{r}_{n1}^{+} + \eta^{'}\boldsymbol{r}_{n2}^{+} + \zeta^{'}\boldsymbol{r}_{n3}^{+} - \boldsymbol{r}_n^{+})\times\nabla G(\boldsymbol{r}_m^{c+},\boldsymbol{r}^{'})d\xi^{'}d\eta^{'} \\ &-l_n\int(\xi^{'}\boldsymbol{r}_{n1}^{-} + \eta^{'}\boldsymbol{r}_{n2}^{-} + \zeta^{'}\boldsymbol{r}_{n3}^{-} - \boldsymbol{r}_n^{-})\times\nabla G(\boldsymbol{r}_m^{c+},\boldsymbol{r}^{'})d\xi^{'}d\eta^{'}\end{aligned} .(15)$$

therefore, the integrals in (14) can be obtained by calculating the following four integrals:

$$I^{m\pm n\pm} = \int_0^1\int_0^{1-\eta^{'}} \nabla G(r_m^{c\pm},r^{'})d\xi^{'}d\eta^{'}, \tag{16}$$

$$I_\xi^{m\pm n\pm} = \int_0^1\int_0^{1-\eta^{'}} \xi^{'}\nabla G(r_m^{c\pm},r^{'})d\xi^{'}d\eta^{'}, \tag{17}$$

$$I_\eta^{m\pm n\pm} = \int_0^1\int_0^{1-\eta^{'}} \eta^{'}\nabla G(r_m^{c\pm},r^{'})d\xi^{'}d\eta^{'}, \tag{18}$$

$$I_\zeta^{m\pm n\pm} = \int_0^1\int_0^{1-\eta^{'}} \zeta^{'}\nabla G(r_m^{c\pm},r^{'})d\xi^{'}d\eta^{'}. \tag{19}$$

To the far interaction, the approximate relation is given by

$$I_\xi^{m\pm n\pm} = I_\eta^{m\pm n\pm} = I_\zeta^{m\pm n\pm} = \frac{1}{3}I^{m\pm n\pm}. \tag{20}$$

Then, equation (13) can be written as:

$$\begin{aligned}[\overline{\overline{\boldsymbol{Z}}}^{EM}_{ss}]_{m,n} = -\{&\frac{l_m}{2}\boldsymbol{\rho}_m^{+}(\boldsymbol{r}_m^{c+})\cdot \\ &[(\frac{1}{3}l_n\boldsymbol{r}_{n1}^{+} + \frac{1}{3}l_n\boldsymbol{r}_{n2}^{+} + \frac{1}{3}l_n\boldsymbol{r}_{n3}^{+} - l_n\boldsymbol{r}_n^{+})I^{m+n+} \\ &-(\frac{1}{3}l_n\boldsymbol{r}_{n1}^{-} + \frac{1}{3}l_n\boldsymbol{r}_{n2}^{-} + \frac{1}{3}l_n\boldsymbol{r}_{n3}^{-} - l_n\boldsymbol{r}_n^{-})I^{m+n-}] \\ &+\frac{l_m}{2}\boldsymbol{\rho}_m^{-}(r_m^{c-})\cdot[(\frac{1}{3}l_n\boldsymbol{r}_{n1}^{+} + \frac{1}{3}l_n\boldsymbol{r}_{n2}^{+} + \frac{1}{3}l_n\boldsymbol{r}_{n3}^{+} - l_n\boldsymbol{r}_n^{+})I^{m-n+} \\ &-(\frac{1}{3}l_n\boldsymbol{r}_{n1}^{-} + \frac{1}{3}l_n\boldsymbol{r}_{n2}^{-} + \frac{1}{3}l_n\boldsymbol{r}_{n3}^{-} - l_n\boldsymbol{r}_n^{-})I^{m-n-}]\}\end{aligned} \tag{21}$$

Due to the oscillatory nature of the gradient of Green's function in (16-19), the fast fill-in method proposed in reference [19] breaks down. Therefore, The X, Y, and Z component of (16) will be calculated by ACA method. Because the oscillatory kernel has little impact on ACA. The ACA method has been described in detail in [14-16] and need not be repeated here.

E. The architecture of 3DMLUV-ACA

To present a whole picture of the implementation of 3DMLUV-ACA, we employ a presentation from coarser to finer considerations. Figure 2 shows the architecture of 3DMLUV, where FFI stands for far-field interaction, NFI stands for near-field interaction, MVM stands for matrix-vector multiplication and SVD stands for singular value decomposition. The criterion used to define the FFI and NFI is discussed in detail in [8].

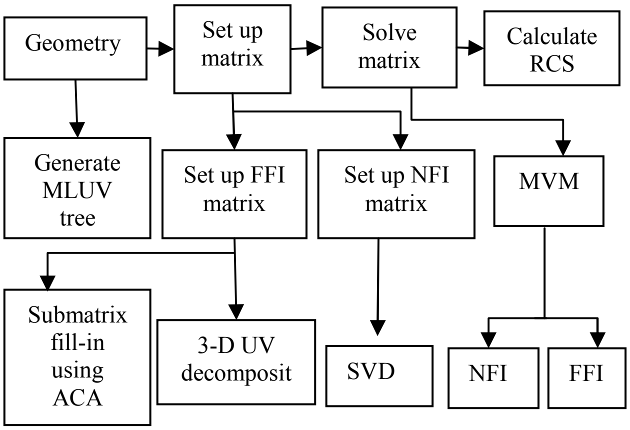

Fig. 2. The architecture of the 3DMLUV-ACA.

Before the UV decomposition is implemented, the FFI submatrix $\overline{\overline{Z}}_{m\times n}^{sub}$ must be calculated, the ACA method is used to speed up the filling as discussed above. Then, the FFI submatrix $\overline{\overline{Z}}_{m\times n}^{sub}$ with low rank r could be approximated by product of a U and V matrix

$$\overline{\overline{Z}}_{m\times n}^{sub} = \overline{\overline{U}}_{m\times r}\overline{\overline{V}}_{r\times n}\ , \tag{12}$$

where $r << \min(m,n)$. Only $\overline{\overline{U}}_{m\times r}$ and $\overline{\overline{V}}_{r\times n}$ will be stored in memory. Thus, the requirement of storage memory descends from $m\times n$ to $r\times(m+n)$. Moreover, during matrix-vector multiplication in iterative method, the original $\overline{\overline{Z}}_{m\times n}^{sub}\overline{I}_{n\times 1}^{sub}$ will be substituted by $\overline{\overline{U}}_{m\times r}\overline{\overline{V}}_{r\times n}\overline{I}_{n\times 1}^{sub}$, which greatly reduce the computational complexity.

III. RESULS AND DEICUSSIONS

A. Accuracy and efficiency

The CPU employed below is Intel Core I7 2.8GHz processor with 2G Bytes of RAM.

To validate the 3DMLUV solution of PMCHWT integral equations, for plane wave with $\theta_i = 0^\circ, \varphi_i = 90^\circ$, the VV-polarized bistatic RCS of a dielectric sphere with radius of $r = 3\lambda$ (λ is the wavelength in free space) in free space is calculated and compared with Mie series in Fig. 3. The relative permittivity $\varepsilon_r = 4$ and the number of unknowns is 86,400. For efficiency analysis, the MLFMM is also used to calculate the scattering of the same sphere The memory requirement and computational time consumed are compared in Table 1.

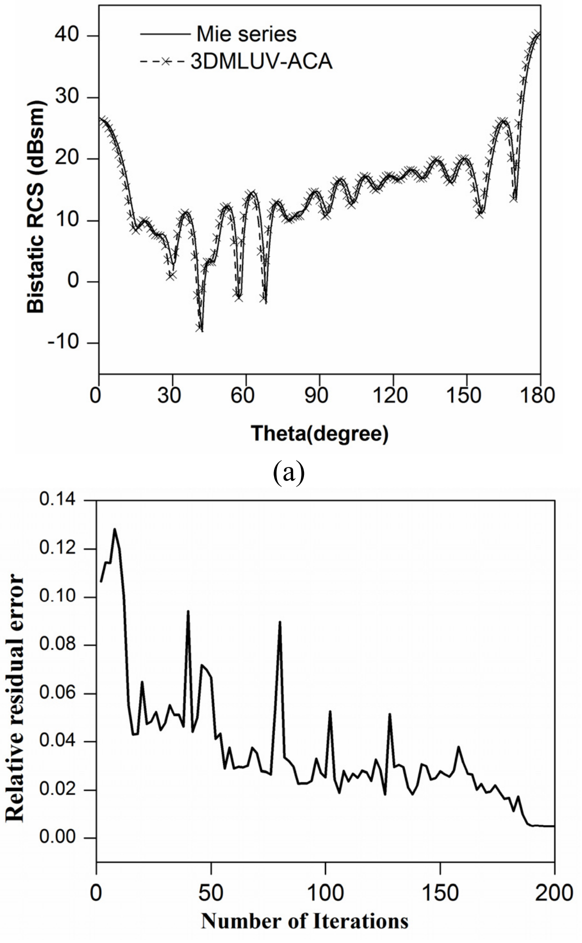

(a)

(b)

Fig. 3. (a) Bistatic RCS of a dielectric sphere; (b) Number of iterations.

Table 1: Memory Requirements and Relative Computational Time.

Method	Unknowns	Memory(MB)	Time(s)
MLFMM	86,400	978	2027
3DMLUV	86,400	946	2160

From Fig. 3 and Table 1, it can be concluded that 3DMLUV-ACA not only show a high computation accuracy but also is highly efficient. The memory 3DMLUV method needed is even lower than the MLFMM method. But because of the fill-in time consumed by 3DMLUV, the computation time needed is slightly more than MLFMM method.

B. Statistic composite EM scattering

In this section, statistic composite scattering is presented and discussed by making 100 Monte Carlo simulations of the rough surface. The tapered incident wave with $\theta_i = 30^\circ, \varphi_i = 90^\circ$ is used for all experiments below.

Case 1: Given surface length $L_x = L_y = 16\lambda$, correlation length $l_x = l_y = 0.5\lambda$, RMS height $h = 0.04\lambda$, the relative dielectric permittivity $\varepsilon_r = 2.5 - 0.18j$. let a PEC cube with side length of $a = 2\lambda$ lie at altitudes of $d = 2\lambda, 10\lambda$ respectively. Figure 4 presents the VV-polarized DRCS. Because the object at the lower altitude has more intense interaction with the underlying rough surface, the DRCS for $d = 2\lambda$ is generally larger than that for $d = 10\lambda$.

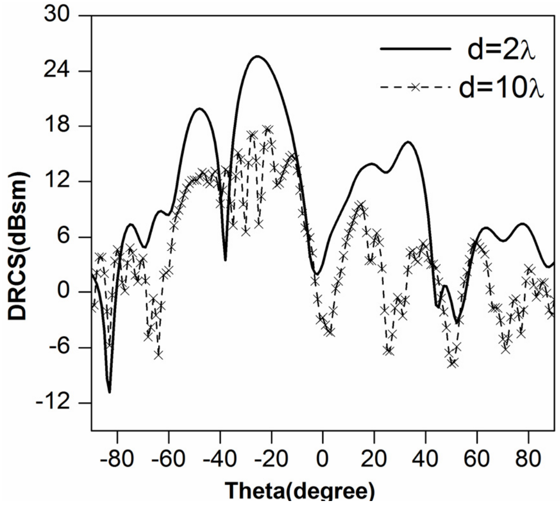

Fig. 4. DRCS of the cube above rough surface for different altitude.

Case 2: Considering a cylinder with a radius of $R = 1\lambda$ and a length of $H = 3\lambda$ lie at an altitude of $d = 3\lambda$ above the dielectric Gaussian rough surface. The rough surface has the same parameters as in Case 1 except that the RMS heights vary as $h = 0.01\lambda, 0.02\lambda, 0.08\lambda$. Figure 5 gives the VV-polarize RCS. It is obviously that the composite bistatic RCS is closely correlated with RMS heights. The composite RCS appears as a peak near $\theta_s = -30^\circ$, which is more significant for the smoother surface with lower value of h. And the incoherent scattering increases while the coherent scattering decreases as the roughness increases.

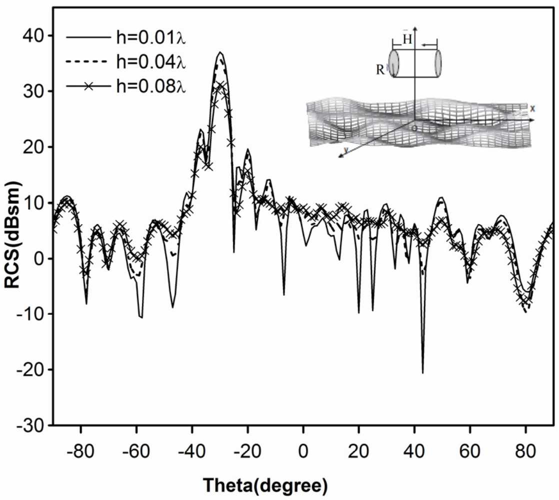

Fig. 5. RCS of the cylinder above rough surface for different RMS heights.

Case 3: let a PEC sphere with radius of $r = 1.5\lambda$ lie at an altitude of $d = 3\lambda$ above a Gaussian dielectric rough surface. The rough surface has the same parameters as in Case 1. Figure 6 presents the composite HH-polarized bistatic RCS and DRCS for different permittivities. The imaginary part of the permittivity is kept the same while the real part of the permittivity vary as 2.5, 5 and 10.

From Fig. 6, we can see that the permittivity also has an important influence on the scattering characteristic. The surface with higher permittivity has higher reflectance. So the composite RCS and DRCS is larger for rough surface with higher permittivity.

IV. CONCLUSION

The 3DMLUV/ACA method is proposed to simulate the scattering from the dielectric objects. By investigating the bistatic electromagnetic scattering from the composite model of a 3-D arbitrarily shaped object located above a 2-D Gaussian dielectric rough surface, this method is proved to be accurate and highly efficient. Furthermore, due to the algebraic nature of 3DMLUV/ACA, this method can be easily extended to the composite scattering of dielectric object located above the dielectric rough surface with a few modifications.

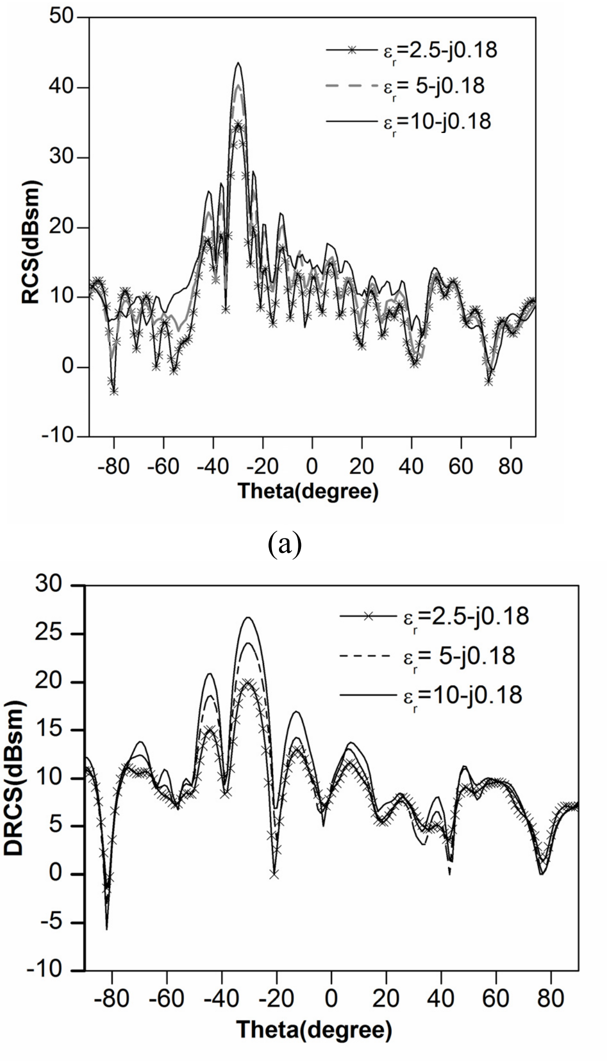

(a)

(b)

Fig. 6. RCS and DRCS of the sphere above rough surface for different permittivities.

ACKNOWLEDGMENT

This work was supported by the National Science Foundation of China (Grant No. 61001059, Grant No.41140034), the China Postdoctoral Science Foundation, and the Fundamental Research Funds for the Central Universities.

REFERENCES

[1] E. A. Shtager, “An Estimation of Sea Surface Influence on Radar Reflectivity of Ships,” *IEEE Trans. Antennas Propagat.,* vol. 47, no. 10, pp. 1623-1627, Oct. 1999.

[2] R. J. Burkholder, M. R. Pino, and F. Obelleiro, “A Monte Carlo Study of the Rough Sea Surface Influence on the Radar Scattering from 2-D Ships,” *IEEE Trans. on Antennas Propagat. Mag.*, vol. 43, no. 2, 25-33, Apr. 2001.

[3] M. R. Pino, R. J. Burkholder and F. Obelleiro, “Spectral Acceleration of the Generalized Forward-Backward Method,” *IEEE Trans. Antennas Propagat.*, vol. 50, no. 6, pp.785-797, Jun. 2002.

[4] K. Jamil., R. J. Burkholder, “Radar Scattering from a Rolling Target Floating on a Time-evolving Rough Sea Surface,” *IEEE Trans. Geosci. Remote Sens.*, vol. 44, no. 11, pp. 3330-3337, 2006.

[5] F.S. Deng, S.Y. He, H.T. Chen, W.D. Hu, W.X. Yu, and G.-Q. Zhu, Numerical Simulat-ion of Vector Wave Scattering from the Target and Rough Surface Composite Model with 3-D Multilevel UV Method, *IEEE Trans. Antennas Propagat.*, vol. 58 , pp. 1625-1634, 2010

[6] S. Y. He, C. Li, F. Zhang, G. Q. Zhu, W. D. Hu, W. X. Yu, “An Improved MM-PO Method with UV Technique for Scattering from an Electrically Large Ship on a Rough Sea Surface at Low Grazing Angle,” *Applied Computational Electromagnetics Society (ACES) Journal*, vol. 26, no. 2, pp. 87-95, February 2011.

[7] J. Li, L. X. Guo, H. Zeng, “FDTD Investigation on Electromagnetic Scattering from Two-Dimensional Layered Rough Surfaces,” *Applied Computational Electromagnetics Society (ACES) Journal*, vol. 25, no. 5, pp. 450 - 475, May 2010.

[8] C. C. Lu and W. C. Chew, “A Multilevel Algorithm for Solving a Boundary Integral Equation of Wave Scattering,” *Microw. Opt. Tech. Lett.*, vol. 7, no. 10, pp. 456-461, Jul. 1994.

[9] J. M. Song and W. C. Chew, “Multilevel Fast Multipole Algorithm for Solving Combined Field Integral Equation of Electromagnetic Scattering,” *Microw. Opt. Tech. Lett.*, vol. 10, no. 1, pp. 14-19, Sep. 1995.

[10] H. Zhao, J. Hu, and Z. Nie, “Parallelization of MLFMA with Composite Load Partition Criteria and Asynchronous Communication,” *Applied Computational Electromagnetic Society (ACES) Journal*, vol. 25, no. 2, pp. 167-173, 2010.

[11] H. Fangjing, Z. Nie, and J. Hu, "An Efficient Parallel Multilevel Fast Multipole Algorithm for Large-Scale Scattering Problems," *Applied Computational Electromagnetic Society (ACES) Journal*, vol. 25, no. 4, pp. 381-387, 2010.

[12] E. Bleszynski, M. Bleszynski, and T. Jaroszewicz, "AIM: Adaptive Integral Method for Solving Large-scale Electromagnetic Scattering and Radiation Problems," *Radio Sci.*, vol. 31, no. 5, pp. 1225-1251, May 1996.

[13] M. Li, H. Chen, C. Li, R. Chen, C. Ong, "Hybrid UV/MLFMA Analysis of Scattering by PEC Targets above a Lossy Half-Space," *Applied Computational Electromagnetics Society (ACES) Journal*, vol. 26, no. 1, pp. 17 - 25, January 2011.

[14] K. Z. Zhao, M. N. Vouvakis, and J. F. Lee, "The Adaptive Cross Approximation Algorithm for Accelerated Method of Moments Computations of EMC Problems," *IEEE Trans. Electromagn. Compat.*, vol. 47, no. 4, pp. 763-773, Nov. 2005.

[15] Z. Liu, R. Chen, J. Chen, Z. Fan, "Using Adaptive Cross Approximation for Efficient Calculation of Monostatic Scattering with Multiple Incident Angles," *Applied Computational Electromagnetics Society (ACES) Journal*, vol. 26, no. 4, pp. 325-333, April 2011.

[16] R. S. Chen, Z. H. Fan, Y. Y. An, M. M. Zhu, K. W. Leung, "Modified Adaptive Cross Approximation Algorithm for Analysis of Electromagnetic Problems," *Applied Computational Electromagnetics Society (ACES) Journal*, vol. 26, no. 2, pp. 160-169, February 2011.

[17] L. Tsang, D. Chen, P. Xu, Q. Li, and V. Jandhyala, "Wave Scattering with the UV Multilevel Partitioning Method: 1. Two-dimensional Problem of Perfect Electric Conductor Surface Scattering," *Radio Sci.*, vol. 39, no. 5, pp. RS5010, 2004.

[18] L.Tsang, Q. Li, P. Xu et al, "Wave Scattering with the UV Multilevel Partitioning Method: 2. Three-dimensional Problem of Nonpenetrable Surface Scattering," *Radio Sci.*, vol. 39, no. 5, RS5011, 2004.

[19] H. T. Chen, J. X. Luo and G. Q. Zhu, "Using UV Technique to Accelerate the MM-PO Method for Three-dimensional Radiation and Scattering Problem," *Microwave Opt. Technol. Lett.*, vol. 48, no. 8, pp.1615 -1618, 2006.

[20] E. Topsakal, R. Kindt, K. Sertel and J. Volakis, "Evaluation of the BiCGSTAB(l) Algorithm for Finite-element/Boundary-integral Method," *IEEE Trans. Antennas Propagat. Mag.*, vol. 43, no. 6, pp.124- 131, Dec.2001.

[21] H. X. Ye, Y. Q. Jin, "Fast Iterative Approach to Difference Scattering from the Object Above a Rough Surface," *IEEE Trans. Geosci. Remote Sens.*, vol. 44, no. 1, pp. 108-115, Jan. 2006.

[22] H. X. Ye, Y. Q. Jin, "Parameterization of the Tapered Incident Wave for Numerical Simulation of Electromagnetic Scattering from Rough Surface," *IEEE Trans. Antennas Propagat.,* vol. 53 no. 3, pp. 1234-1237, Mar. 2005.

[23] S. M. Rao, D. R.Wilton, and A.W. Glisson, "Electromagnetic Scattering by Surfaces of Arbitrary Shape," *IEEE Trans. Antennas Propagat.*, vol. AP-30, pp. 409-418, May 1982.

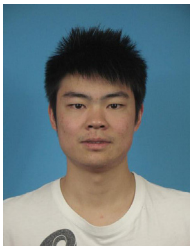

C. Li was born in 1986. He received the B.S degree in information countermeasure technology from North University of China, Taiyuan, in 2008. He is currently working towards the Ph.D degree in Radio Physics at Wuhan University, Wuhan, China. His current research interests are electromagnetic inverse scattering, computational electromagnetic method, microwave imaging and time domain echo analysis.

S. Y. He was born in 1982. She received the telecommunication engineering degree and the Ph.D. degree in Radio Physics from Wuhan University, Wuhan, China, in 2003 and 2009, respectively. She is currently a associate professor in Wuhan Universtiy. From 2005 to 2006, she was a Research Assistant in Wireless Communications Research Centre, City University of Hong Kong. Her research interests include EM theory and its application, computational electromagnetic, and radar imaging.

A Hybrid ACA-FDM for Electromagnetic Scattering from PEC Targets

Xinlei Chen, Changqing Gu, Xiaoqiao Deng, Bingzheng Xu, Zhuo Li, and Zhenyi Niu

College of Electronic and Information Engineering
Nanjing University of Aeronautics and Astronautics, Nanjing 210016, China
gucq@nuaa.edu.cn

Abstract **─** In this paper, the adaptive cross approximation (ACA) algorithm is combined with the fast dipole method (FDM) to solve the electromagnetic scattering from perfect electric conducting (PEC) targets. In the ACA-FDM, the ACA and the FDM are employed to deal with the near-group pairs and the far-group pairs respectively. Compared with the conventional FDM, the submatrices related to the interactions of the near-group pairs are efficiently compressed by the ACA, so the ACA-FDM saves CPU time and memory requirement, when the criterion for the far-group pairs becomes stricter in order to obtain relatively high accurate solutions. Numerical results about the electromagnetic scattering from PEC targets are given to demonstrate the merits of the ACA-FDM.

Index Terms **─** Electromagnetic scattering, equivalent dipole method (EDM), fast dipole method (FDM), adaptive cross approximation (ACA).

I. INTRODUCTION

The method of moments (MoM) has been widely used to solve electromagnetic scattering problems. However, the computational complexity and memory storage of the conventional MoM which leads to a dense matrix equation are both $O(N^2)$ for matrix iterative solvers, where N is the number of unknowns. Both the matrix-fill and matrix-solve processes are expensive. Fortunately, many methods have been developed in order to overcome this problem through these years, such as multilevel fast multipole algorithm (MLFMA) [1-2], adaptive integral method (AIM) [3-4], pre-corrected fast Fourier transform (P-FFT) method [5-6] and adaptive cross approximation (ACA) algorithm [7-12].

Recently, the equivalent dipole method (EDM) [13-14] based on the commonly used Rao-Wilton-Glisson (RWG) [15] basis function has been developed to simplify the MoM impedance matrix element filling procedure. In the EDM, each RWG element is viewed as a dipole model with an equivalent moment, and the mutual impedance elements is replaced by the interactions of equivalent dipoles, which has a simple closed canonical form. However, the computational complexity and memory storage of the EDM don’t change, which are still $O(N^2)$. More recently, the fast dipole method (FDM) [16-17] is proposed to mitigate this problem. Through a simple Taylor's series expansion of all the terms including R in the formulation of EDM, the FDM can achieve the separation of the field dipole and source dipole. Therefore the complexity of interactions between two far groups such as group i and j can be reduced from $O(N_i N_j)$ to $O(N_i + N_j)$, where N_i and N_j are the number of the dipoles in group i and j, respectively.

However, in order to get good solutions, the FDM has to choose stricter criterion for far-group pairs. In other words, the number of near-group pairs must increase. Although the near group interactions can be efficiently calculated by the EDM, they will still lead to rapidly increase in memory requirement and CPU time in the matrix-vector products (MVPs). In this work, the adaptive cross approximation (ACA) algorithm [8] is employed to deal with the near group interactions. The ACA is purely algebraic in nature and relatively easy to implement. Also, it does not require knowing all the impedances of

Submitted On: May 14, 2012
Accepted On: Oct. 8, 2012

submatrices. For a relatively high accuracy the hybrid ACA-FDM saves memory requirement and CPU time than the conventional FDM.

The remainder of the paper is organized as follows. In Section II, the basic principle of the FDM is presented. Then we describe how the ACA is combined with the FDM in detail. In Section III, some numerical results about the bistatic radar cross section (RCS) are given to verify the efficiency and accuracy of the new method. Finally, conclusions are drawn in Section IV.

II. FORMULATIONS

A. Basic Principles of the FDM

For perfect electric conducting (PEC) targets, the equivalent dipole method (EDM) [13-14] views each RWG element as a small dipole and the mutual impedance is replaced by the interaction between two dipoles when the distance of the two dipoles is beyond a appropriate threshold distance (typically 0.2 λ ~0.5 λ). Considering two well-separated dipoles (the *m*th dipole and the *n*th dipole), the relevant impedance element for electric field integral equation (EFIE) and magnetic field integral equation (MFIE) can be calculated by [13-14]

$$Z_{mn}^{E} = jk\eta \mathbf{m}_m \cdot \bar{\mathbf{G}}(\mathbf{R}) \cdot \mathbf{m}_n \tag{1}$$

$$Z_{mn}^{M} = jk\eta \mathbf{m}'_m \cdot \mathbf{G}(\mathbf{R}) \times \mathbf{m}_n \tag{2}$$

where

$$\begin{aligned}\bar{\mathbf{G}}(\mathbf{R}) = \frac{e^{-jkR}}{4\pi R}\Bigg[&\bar{\mathbf{I}}\left(1+\frac{1}{jkR}+\frac{1}{(jkR)^2}\right)\\ &-\hat{\mathbf{R}}\hat{\mathbf{R}}\left(1+\frac{3}{jkR}+\frac{3}{(jkR)^2}\right)\Bigg]\end{aligned} \tag{3}$$

$$\mathbf{G}(\mathbf{R}) = \frac{e^{-jkR}}{4\pi R}\left(1+\frac{1}{jkR}\right)\hat{\mathbf{R}} \tag{4}$$

In (1)~(4), $\mathbf{m}_m = l_m(\mathbf{r}_m^{c-} - \mathbf{r}_m^{c+})$ and $\mathbf{m}_n = l_n(\mathbf{r}_n^{c-} - \mathbf{r}_n^{c+})$ are the equivalent dipole moments of the *m*th and *n*th RWG elements. $\mathbf{m}'_m = \mathbf{m}_m \times \hat{\mathbf{n}}_m$. $\mathbf{r}_m^{c\pm}(\mathbf{r}_n^{c\pm})$ is the position vector of the centroid of two adjacent triangular patches $T_m^{\pm}(T_n^{\pm})$, and $l_m(l_n)$ is the length of the common edge of $T_m^{\pm}(T_n^{\pm})$. $\hat{\mathbf{n}}_m = (\hat{\mathbf{n}}_m^{+} + \hat{\mathbf{n}}_m^{-}) \big/ \left|\hat{\mathbf{n}}_m^{+} + \hat{\mathbf{n}}_m^{-}\right|$ is the average normal vector, and $\hat{\mathbf{n}}_m^{\pm}$ represent the unit normal vectors of $T_m^{\pm}$. $\mathbf{r}_n = (\mathbf{r}_n^{c+} + \mathbf{r}_n^{c-})/2$ and $\mathbf{r}_m = (\mathbf{r}_m^{c+} + \mathbf{r}_m^{c-})/2$ respectively represent the position vectors of the *n*th and *m*th dipoles' centers (see Fig. 1). $\mathbf{R} = \mathbf{r}_{mn} = \mathbf{r}_m - \mathbf{r}_n$, $R = \left|\mathbf{R}\right|$, $\hat{\mathbf{R}} = \mathbf{R}/R$. η and k are the impedance and wavenumber of the free space.

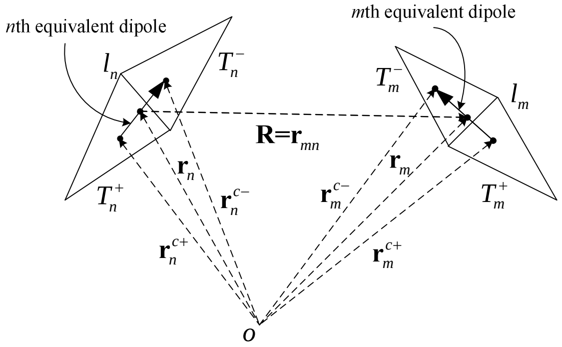

Fig. 1. Geometry of the *m*th and *n*th RWG elements and their equivalent dipole models [16].

It can be seen from (1) and (2) that the calculation of mutual impedance elements of both EFIE and MFIE in the EDM is very simple. However, it don't change the memory cost and matrix-solve time. The fast dipole method (FDM) [16-17] can mitigate this problem. In the FDM, the target is grouped with equally sized cubes, then all dipoles are assigned to individual cubes. The FDM is used in those far-group pairs. We use $D(i,j) = \max\{|x_i - x_j|, |y_i - y_j|, |z_i - z_j|\}/\Delta$ to define the distance between two groups i and j , in which (x_i, y_i, z_i) and (x_j, y_j, z_j) are the coordinates of the centroid of group i and group j , Δ is the side length of the group. A given integer D_b ($D_b \geqslant 1$) is used to decide if the two groups are far-group pair. If $D(i,j) > D_b$, the two groups are a far-group pair. It can be found that the FDM will give more accurate solutions with the increment of D_b, so D_b can be used to control the accuracy of the FDM.

Now, we consider two dipoles m and n that respectively belongs to group j and i , and suppose the two groups are a far-group pair. The impedance element can be represented as (1) and (2) for EFIE and MFIE. The distance between the two dipoles can be written as

$$\mathbf{R} = \mathbf{r}_{ji} + \mathbf{r}_{mj} - \mathbf{r}_{ni} = \mathbf{r}_{mp} - \mathbf{r}_{np} \tag{5}$$

where $\mathbf{r}_{ji} = \mathbf{r}_{o_j} - \mathbf{r}_{o_i}$, $\mathbf{r}_{mj} = \mathbf{r}_m - \mathbf{r}_{o_j}$, $\mathbf{r}_{ni} = \mathbf{r}_n - \mathbf{r}_{o_i}$. $\mathbf{r}_{mp} = \mathbf{r}_m - \mathbf{r}_p$, $\mathbf{r}_{np} = \mathbf{r}_n - \mathbf{r}_p$, $\mathbf{r}_p = \left(\mathbf{r}_{o_j} + \mathbf{r}_{o_i}\right)/2$. $\mathbf{r}_{o_i}$ and

$\mathbf{r}_{o_j}$ are the center positions of group i and j shown in Fig. 2.

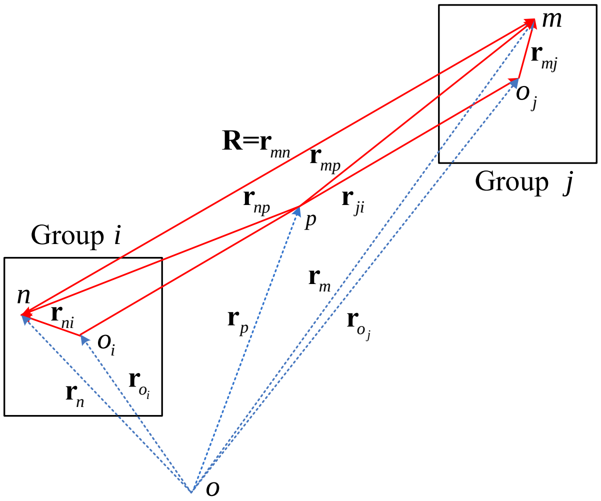

Fig. 2. The mth and nth RWG elements and the groups they belong to [16].

R^{α} (α =1,-1,-2,-3) in (3) and (4) can be expanded using the Taylor series as [17]

$$R^{\alpha}=\left|\mathbf{r}_{ji}+\mathbf{r}_{mj}-\mathbf{r}_{ni}\right|^{\alpha}$$
$$=r_{ji}^{\alpha}\left[1+\left(\frac{2\hat{\mathbf{r}}_{ji}\cdot\mathbf{r}_{mj}}{r_{ji}}+\frac{r_{mj}^2}{r_{ji}^2}\right)+\left(\frac{2\hat{\mathbf{r}}_{ij}\cdot\mathbf{r}_{ni}}{r_{ij}}+\frac{r_{ni}^2}{r_{ij}^2}\right)-\frac{2\mathbf{r}_{mj}\cdot\mathbf{r}_{ni}}{r_{ji}^2}\right]^{\frac{\alpha}{2}}$$
$$\approx R_m^{(\alpha)}+R_n^{(\alpha)} \tag{6}$$

where

$$R_m^{(\alpha)}=r_{ji}^{\alpha}\left[\frac{1}{2}+\alpha\left(\frac{\hat{\mathbf{r}}_{ji}\cdot\mathbf{r}_{mj}}{r_{ji}}+\frac{r_{mj}^2+(\alpha-2)\left(\hat{\mathbf{r}}_{ji}\cdot\mathbf{r}_{mj}\right)^2}{2r_{ji}^2}\right)\right] \tag{7}$$

$$R_n^{(\alpha)}=r_{ij}^{\alpha}\left[\frac{1}{2}+\alpha\left(\frac{\hat{\mathbf{r}}_{ij}\cdot\mathbf{r}_{ni}}{r_{ij}}+\frac{r_{ni}^2+(\alpha-2)\left(\hat{\mathbf{r}}_{ij}\cdot\mathbf{r}_{ni}\right)^2}{2r_{ij}^2}\right)\right] \tag{8}$$

The dyad $\hat{\mathbf{R}}\hat{\mathbf{R}}$ in (3) can be approximated as [17]

$$\hat{\mathbf{R}}\hat{\mathbf{R}}\approx\frac{1}{r_{ji}^2}[\mathbf{r}_{ji}\mathbf{r}_{ji}+(\mathbf{s}_m-\mathbf{s}_n)\mathbf{r}_{ji}+\mathbf{r}_{ji}(\mathbf{s}_m-\mathbf{s}_n)]$$
$$=\overline{\mathbf{T}}_m+\overline{\mathbf{T}}_n \tag{9}$$

in which

$$\overline{\mathbf{T}}_m=\frac{1}{r_{ji}^2}\left[\frac{1}{2}\mathbf{r}_{ji}\mathbf{r}_{ji}+\mathbf{s}_m\mathbf{r}_{ji}+\mathbf{r}_{ji}\mathbf{s}_m\right] \tag{10}$$

$$\overline{\mathbf{T}}_n=\frac{1}{r_{ij}^2}\left[\frac{1}{2}\mathbf{r}_{ij}\mathbf{r}_{ij}+\mathbf{s}_n\mathbf{r}_{ij}+\mathbf{r}_{ij}\mathbf{s}_n\right] \tag{11}$$

$$\mathbf{s}_m=\mathbf{r}_{mj}-\mathbf{r}_{mj}\cdot\hat{\mathbf{r}}_{ji}\hat{\mathbf{r}}_{ji} \tag{12}$$

$$\mathbf{s}_n=\mathbf{r}_{ni}-\mathbf{r}_{ni}\cdot\hat{\mathbf{r}}_{ij}\hat{\mathbf{r}}_{ij} \tag{13}$$

Substituting (6) (α =1,-1,-2,-3) and (9) into (1), and substituting (6) (α =1,-2,-3) and (5) into (2), the impedance element in the FDM for EFIE and MFIE can be obtained.

$$Z_{mn}^E\approx\frac{jk\eta}{4\pi}\mathbf{M}_m\cdot\left[\overline{\mathbf{I}}(A_m+A_n)-(\overline{\mathbf{T}}_m+\overline{\mathbf{T}}_n)(B_m+B_n)\right]\cdot\mathbf{M}_n$$
$$=\frac{jk\eta}{4\pi}\Big[\left(A_m\mathbf{M}_m-B_m\mathbf{M}_m\cdot\overline{\mathbf{T}}_m\right)\cdot\mathbf{M}_n \tag{14}$$
$$+\mathbf{M}_m\cdot\left(A_n\mathbf{M}_n-B_n\overline{\mathbf{T}}_n\cdot\mathbf{M}_n\right)-\left(\mathbf{M}_m\cdot\overline{\mathbf{T}}_m\right)\cdot\left(B_n\mathbf{M}_n\right)$$
$$-\left(B_m\mathbf{M}_m\right)\cdot\left(\overline{\mathbf{T}}_n\cdot\mathbf{M}_n\right)\Big]$$

$$Z_{mn}^M\approx\frac{jk\eta}{4\pi}\mathbf{M}'_m\cdot(C_m+C_n)\left(\mathbf{r}_{mp}-\mathbf{r}_{np}\right)\times\mathbf{M}_n$$
$$=\frac{jk\eta}{4\pi}\Big[\left(C_m\mathbf{M}'_m\times\mathbf{r}_{mp}\right)\cdot\mathbf{M}_n$$
$$+\left(\mathbf{M}'_m\times\mathbf{r}_{mp}\right)\cdot\left(C_n\mathbf{M}_n\right) \tag{15}$$
$$+\left(C_m\mathbf{M}'_m\right)\cdot\left(\mathbf{M}_n\times\mathbf{r}_{np}\right)$$
$$+\mathbf{M}'_m\cdot\left(C_n\mathbf{M}_n\times\mathbf{r}_{np}\right)\Big]$$

where

$$A_u=R_u^{(-1)}+\left(jk\right)^{-1}R_u^{(-2)}+\left(jk\right)^{-2}R_u^{(-3)} \tag{16}$$

$$B_u=R_u^{(-1)}+3\left(jk\right)^{-1}R_u^{(-2)}+3\left(jk\right)^{-2}R_u^{(-3)} \tag{17}$$

$$C_u=R_u^{(-2)}+\left(jk\right)^{-1}R_u^{(-3)} \tag{18}$$

$$\mathbf{M}_u=\mathbf{m}_u e^{-jkR_u^{(1)}} \tag{19}$$

$$\mathbf{M}'_u=\mathbf{m}'_u e^{-jkR_u^{(1)}} \tag{20}$$

for $u=m,n$

Now we discuss how the FDM can efficiently calculate the MVPs for a far-group pair (such as group j and i). We suppose the two groups contain N_j and N_i dipoles, respectively. For a iterative solver such as GMRES, the MVP between far groups j and i

$$\mathbf{V}_j=\mathbf{Z}_{ji}\mathbf{I}_i \tag{21}$$

need be computed, where $\mathbf{Z}_{ji}$ are the impedance submatrix between groups j and i, whose size is $N_j\times N_i$, $\mathbf{I}_i$ with a size of $N_i\times 1$ is the current subvector, $\mathbf{V}_j$ with a size of $N_j\times 1$ is the result of $\mathbf{Z}_{ji}\mathbf{I}_i$. The complexity of (21) is $O(N_iN_j)$. When the FDM is used to calculate these interactions between groups j and i, an element v_m of $\mathbf{V}_j$ for EFIE and MFIE can be approximatively represented as follows.

$$\begin{aligned} v_m^E &= \sum_{n=1}^{N_i} Z_{mn}^E I_n \\ &\approx \frac{jk\eta}{4\pi}\Bigg[\left(A_m\mathbf{M}_m - B_m\mathbf{M}_m \cdot \overline{\mathbf{T}}_m\right)\cdot \sum_{n=1}^{N_i}\mathbf{M}_n I_n \\ &\quad +\mathbf{M}_m \cdot \sum_{n=1}^{N_i}\left(A_n\mathbf{M}_n - B_n\overline{\mathbf{T}}_n\cdot\mathbf{M}_n\right) I_n \\ &\quad -\left(\mathbf{M}_m\cdot\overline{\mathbf{T}}_m\right)\cdot\sum_{n=1}^{N_i}\left(B_n\mathbf{M}_n\right)I_n \\ &\quad -\left(B_m\mathbf{M}_m\right)\cdot\sum_{n=1}^{N_i}\left(\overline{\mathbf{T}}_n\cdot\mathbf{M}_n\right)I_n\Bigg] \end{aligned} \tag{22}$$

$$\begin{aligned} v_m^M &= \sum_{n=1}^{N_i} Z_{mn}^M I_n \\ &\approx \frac{jk\eta}{4\pi}\Bigg[\left(C_m\mathbf{M}'_m \times \mathbf{r}_{mp}\right)\cdot \sum_{n=1}^{N_i}\mathbf{M}_n I_n \\ &\quad +\left(\mathbf{M}'_m\times\mathbf{r}_{mp}\right)\cdot\sum_{n=1}^{N_i}\left(C_n\mathbf{M}_n\right)I_n \\ &\quad +\left(C_m\mathbf{M}'_m\right)\cdot\sum_{n=1}^{N_i}\left(\mathbf{M}_n\times\mathbf{r}_{np}\right)I_n \\ &\quad +\mathbf{M}'_m\cdot\sum_{n=1}^{N_i}\left(C_n\mathbf{M}_n\times\mathbf{r}_{np}\right)I_n\Bigg] \end{aligned} \tag{23}$$

Now we consider a term in (22) as an example to illustrate how the FDM works. It can be found that

$$\left(A_m\mathbf{M}_m - B_m\mathbf{M}_m\cdot\overline{\mathbf{T}}_m\right)\cdot\sum_{n=1}^{N_i}\mathbf{M}_n I_n \tag{24}$$

achieves the separation of *m* and *n*. Therefore, the result $\sum_{n=1}^{N_i}\mathbf{M}_n I_n$ is independent of *m*. For different dipole *m* in group *j*, $\sum_{n=1}^{N_i}\mathbf{M}_n I_n$ can be reused, so it only need be calculated once. All other terms in (22) and (23) can be handled in the same way. Thus the complexity of (21) is reduced to $O(N_i + N_j)$ by the FDM.

B. The ACA-FDM

It is easy to know that the error brought by the FDM is decreasing with the increment of D_b. However, with the increase in D_b the near region increases quickly, which will increase memory and CPU time requirement. In this article, the adaptive cross approximation (ACA) [8] is employed in the near region to mitigate this problem. The ACA algorithm is a matrix decomposition algorithm which only requires partial impedance elements of original matrices and easy to implement, which can be efficiently calculated by the EDM.

Considering two near groups such as group i and group j ($1 < D(i,j) \le D_b$) which include N_i and N_j dipoles, respectively. The interactions $\mathbf{Z}_{ji}$ between the two groups can be approximated by the ACA as

$$\mathbf{Z}_{ji} \approx \mathbf{U}_{ji}\mathbf{V}_{ji} \tag{25}$$

where r denotes the effective rank of the submatrix $\mathbf{Z}_{ji}$. $\mathbf{U}_{ji}$ is a matrix of size $N_j \times r$, and $\mathbf{V}_{ji}$ is a matrix of size $r \times N_i$. The goal of the ACA is to achieve error matrix

$$\left\|\mathbf{R}_{ji}\right\|_F = \left\|\mathbf{Z}_{ji} - \mathbf{U}_{ji}\mathbf{V}_{ji}\right\|_F \le \varepsilon\left\|\mathbf{Z}_{ji}\right\|_F \tag{26}$$

where ε is a given tolerance, and $\|\bullet\|_F$ represents the matrix Frobenius norm. The accuracy of the ACA can be easily controlled by a given tolerance ε. According to [8], a tolerance of 10^{-2} can give accurate results, which is used in the ACA region in this paper.

The detail of the ACA algorithm [8] is presented as follows.

□ Initialization $\tilde{\mathbf{R}} = 0$, $\left\|\tilde{\mathbf{Z}}^{(0)}\right\|^2 = 0$, $k = 1$.

□ Find I_k : if ($k = 1$) $I_k = 1$; else $I_k : \left|\tilde{\mathbf{R}}(I_k, J_{k-1})\right| = \max_i(\left|\tilde{\mathbf{R}}(i, J_{k-1})\right|)$, $i \ne I_1, \cdots, I_{k-1}$.

□ $\tilde{\mathbf{R}}(I_k,:) = \mathbf{Z}(I_k,:) - \sum_{l=1}^{k-1}(\mathbf{u}_l)_{I_k}\mathbf{v}_l$.

□ Find J_k : $\left|\tilde{\mathbf{R}}(I_k, J_k)\right| = \max_j(\left|\tilde{\mathbf{R}}(I_k, j)\right|)$, $j \ne J_1, \cdots, J_{k-1}$.

□ $\mathbf{v}_k = \tilde{\mathbf{R}}(I_k,:)/\tilde{\mathbf{R}}(I_k, J_k)$.

□ $\tilde{\mathbf{R}}(:, J_k) = \mathbf{Z}(:, J_k) - \sum_{l=1}^{k-1}(\mathbf{v}_l)_{J_k}\mathbf{u}_l$.

□ $\mathbf{u}_k = \tilde{\mathbf{R}}(:, J_k)$.

□ $\left\|\tilde{\mathbf{Z}}^{(k)}\right\|^2 = \left\|\tilde{\mathbf{Z}}^{(k-1)}\right\|^2 + 2\sum_{j=1}^{k-1}\left|\mathbf{u}_j^T\mathbf{u}_k\right|\left|\mathbf{v}_j^T\mathbf{v}_j\right| + \left\|\mathbf{u}_k\right\|^2\left\|\mathbf{v}_k\right\|^2$.

□ Check convergence: if ($\left\|\mathbf{u}_k\right\|\left\|\mathbf{v}_k\right\| \le \varepsilon\left\|\tilde{\mathbf{Z}}^{(k)}\right\|$), end iteration; else $k = k + 1$ and goto □.

The MVP related to the two near groups *j* and *i* can be approximatively represented as

$$\mathbf{Z}_{ji}\mathbf{I}_i \approx \mathbf{U}_{ji}\left(\mathbf{V}_{ji}\mathbf{I}_i\right) \tag{27}$$

Clearly, the complexity of (27) is $O(r(N_i + N_j))$. Moreover, $\mathbf{U}_{ji}$ and $\mathbf{V}_{ji}$ are stored instead of $\mathbf{Z}_{ji}$, so the complexity of memory requirement is also reduced to $O(r(N_i + N_j))$.

In ACA-FDM, the ACA and the FDM are used to deal with the near-group pairs and the far-group pairs, respectively. Thus both near-group pairs and far-group pairs can be efficiently calculated in the ACA-FDM. Compared with the conventional FDM, the performance of the near-group interactions are improved by the ACA.

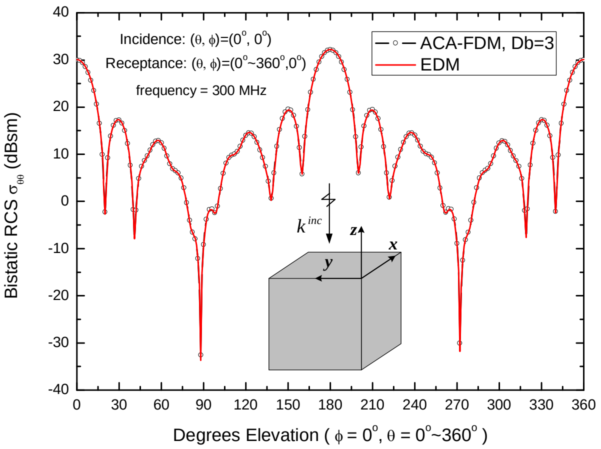

Fig. 3. Bistatic RCSs of a 3 m×3 m×3 m PEC cube.

III. NUMERICAL RESULTS

In this section, the ACA-FDM is implemented in the RCS calculations. All the simulations are performed on a personal computer with the Intel(R) Pentium(R) Dual-Core CPU E5500 with 2.8 GHz (only one core is used) and 2.0 GB RAM. The combined field integral equation (CFIE) (combination parameter is 0.5) is used. The GMRES iterative solver is employed to obtain an identical residual error ≤ 0.01. The block diagonal preconditioner (BDP) is used in all the simulations. All the targets are discretized into triangular patches with an average edge length of 0.1λ. In this paper, the threshold distance of the EDM is chosen as 0.2λ. All the objects are illuminated by a $\hat{\mathbf{x}}$-polarized plane wave with the incident direction of $(\theta,\phi)=(0^\circ,0^\circ)$

First we consider the scattering problem of a PEC cube with side length of 2.5 m. The cube is divided into 12228 triangular patches, and the total number of unknowns is 18342. All the unknowns are divided into 218 nonempty groups and the size of each group is 0.45λ. Figure 3 gives the bistatic RCSs for *θθ* polarization calculated by the ACA-FDM (D_b=3) and the EDM. Results show good agreement.

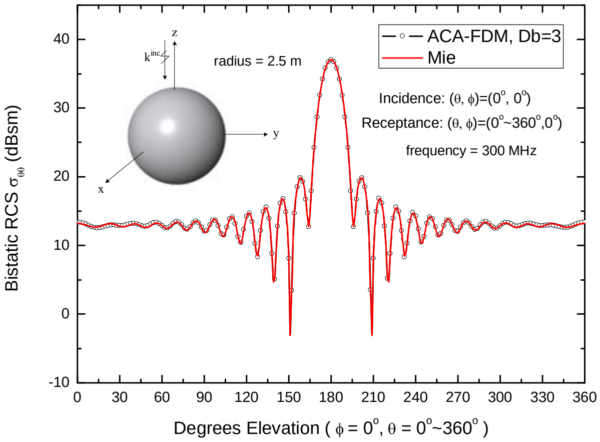

Fig. 4. Bistatic RCSs of a PEC sphere of radius 2.5 m.

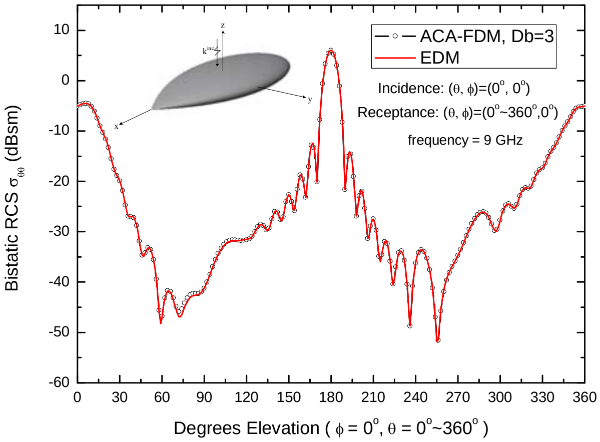

Fig. 5. Bistatic RCSs of a 252.3744-mm PEC NASA almond.

The second problem is a PEC sphere with radius 3 m. The sphere is meshed into 19260 triangular patches and there are total 28890 unknowns. All the unknowns are divided into 409 nonempty groups and the size of each group is 0.55λ. The bistatic RCSs in *θθ* polarization are shown in Fig. 4. The result obtained by the ACA-FDM (D_b=3) agrees well with the Mie series solution, which is exact and used as a reference.

Finally, the bistatic RCSs of a 252.3744-mm PEC NASA almond are calculated. The almond is divided into 8808 triangular patches and the number of unknowns is 13212. Totally 102 nonempty groups with the size of 0.65 λ are obtained. The bistatic RCS in $\theta\theta$ polarization calculated by the ACA-FDM (D_b=3) is compared with the EDM shown in Fig. 5.

Table 1: Comparison of CPU time and memory cost for different D_b values

Problem 1: cube		
D_b	FDM/ACA-FDM	
	Time (s)	RAM (MB)
1	61/61	135/135
2	75/66	363/194
3	97/73	706/270
Problem 2: sphere		
D_b	FDM/ACA-FDM	
	Time (s)	RAM (MB)
1	159/159	280/280
2	188/166	745/386
3	236/182	1434/523
Problem 3: almond		
D_b	FDM/ACA-FDM	
	Time (s)	RAM (MB)
1	38/38	229/229
2	57/42	504/273
3	76/45	775/310

The memory requirements and CPU time for the simulations above are summarized in Table 1. From Table 1, it can be found that the ACA-FDM saves CPU time and memory requirement than the conventional FDM, when D_b (>1) is chosen as the same value for the two methods. When D_b=1, the ACA-FDM is the same as the conventional FDM, because the ACA algorithm is only used to handle the nonadjacent groups. As shown in Fig. 3~5, we can find that the CFIE (combination parameter is 0.5) solved by the ACA-FDM (D_b=3) can give good RCS solutions for the three examples. However, it is worth mentioning that the stricter criterion D_b of the ACA-FDM may be required when more complex or larger targets are calculated, or when larger group size is chosen.

IV. CONCLUSION

In this article, a hybrid ACA-FDM is implemented to accelerate solving the electromagnetic scattering from PEC targets. In the ACA-FDM, the ACA and the FDM are used to deal with the near-group pairs and the far-group pairs, respectively. Profiting from the use of ACA algorithm in the near region, the ACA-FDM saves memory and CPU time than the FDM when the criteria for the far region becomes stricter.

ACKNOWLEDGMENT

The work was supported by the National Nature Science Foundation of China under Grant No. 61071019, the Funding of Jiangsu Innovation Program for Graduate Education under Grant No. CXZZ11_0229, and the Fundamental Research Funds for the Central Universities.

REFERENCES

[1] J. M. Song and W. C. Chew, “Multilevel Fast-Multipole Algorithm for Solving Combined Field Integral Equations of Electromagnetic Scattering,” *Microwave Opt. Technol. Lett.*, vol. 10, no. 1, pp. 14-19, 1995.

[2] J. M. Song, C. C. Lu, and W. C. Chew, “Multilevel Fast Multipole Algorithm for Electromagnetic Scattering by Large Complex Objects,” *IEEE Trans. Antennas Propagat.*, vol. 45, no. 10, pp. 1488-1493, 1997.

[3] E. Bleszynski, M. Bleszynski, and T. Jaroszewicz, “AIM: Adaptive Integral Method for Solving Large-scale Electromagnetic Scattering and Radiation Problems,” *Radio Sci*, vol. 31, no. 5, pp. 1225-1251, 1996.

[4] C. F. Wang, F. Ling, J. Song, and J.-M. Jin, “Adaptive Integral Solution of Combined Field Integral Equation,” *Microw. Opt. Technol. Lett.*, vol. 19, no. 5, pp. 321-328, 1998.

[5] J. K. White, J. R. Phillips and T. Korsmeyer, “Comparing Precorrected-FFT Method and Fast Multipole Algorithms for Solving Three-dimensional Potential Integral Equations,” *Proc Cocrado Conf Iterative Methods, Proceedings*, 1994.

[6] J. R. Phillips and J. K. White, “A Precorrected-FFT Method for Electrostatic Analysis of Complicated 3-D Structures,” *IEEE Trans. Computer-Adided Design Integr Circuits Syst.*, vol. 16, no. 10, pp. 1059-1072, 1997.

[7] M. Bebendorf, “Approximation of Boundary Element Matrices,” *Numer. Math*, vol. 86, no. 4, pp. 565-589, 2000.

[8] K. Zhao, M. N. Vouvakis, and J.-F. Lee, “The Adaptive Cross Approximation Algorithm for Accelerated Method of Moments Computations of EMC,” *IEEE Trans. Electromagn. Compat.*, vol. 47, no. 4, pp. 763-773, 2005.

[9] Z. Liu, R. Chen, J. Chen, Z. Fan, "Using Adaptive Cross Approximation for Efficient Calculation of Monostatic Scattering with Multiple Incident Angles," *Applied Computational Electromagnetics Society (ACES) Journal*, vol. 26, no. 4, pp. 325-333, 2011.

[10] R. S. Chen, Z. H. Fan, Y. Y. An, M. M. Zhu, K. W. Leung, "Modified Adaptive Cross Approximation Algorithm for Analysis of Electromagnetic Problems," *Applied Computational Electromagnetics Society (ACES) Journal*, vol. 26, no. 2, pp. 160-169, 2011.

[11] M. Chen, R. S. Chen, X. Q. Hu, "Augmented MLFMM for Analysis of Scattering from PEC Object with Fine Structures," *Applied Computational Electromagnetics Society (ACES) Journal*, vol. 26, no. 5, pp. 418-428, 2011.

[12] T. Wan, R. Chen, X. Hu, Y. Chen, Y. Shen, "Efficient Direct Solution of EFIE for Electrically Large Scattering Problems using H-LDLT and PE Basis Function," *Applied Computational Electromagnetics Society (ACES) Journal*, vol. 26, no. 7, pp. 561-571, July 2011.

[13] J. Yeo, S. Koksoy, V. V. S. Prakash, and R. Mittra, "Efficient Generation of Method of Moments Matrices using the Characteristic Function Method," *IEEE Trans. Antennas Propag.*, vol. 52, no. 12, pp. 3405-3410, 2004.

[14] J. Yuan, C. Gu and G. Han, "Efficient Generation of Method of Moments Matrices using Equivalent Dipole-moment Method," *IEEE Antennas and Wireless Propag. Lett.*, vol. 8, pp. 716-719, 2009.

[15] S. M. Rao, D. R. Wilton, and A. W. Glisson, "Electromagnetic Scattering by Surfaces of Arbitrary Shape," *IEEE Trans. Antennas Propag.*, vol. 30, no. 3, pp. 409-418, 1982.

[16] X. Chen, C. Gu, Z. Niu and Z. Li, "Fast Dipole Method for Electromagnetic Scattering from Perfect Electric Conducting Targets," *IEEE Trans. Antennas Propag.*, vol. 60, no. 2, pp. 1186-1191, 2012.

[17] X. Chen, Z. Li, Z. Niu, and C. Gu, "Analysis of Electromagnetic Scattering from PEC Targets using Improved Fast Dipole Method," *Journal of Electromagnetic Waves and Applications*, vol. 25, no. 16, pp. 2254-2263, 2011.

A Novel Single-Sided Wideband Metamaterial

Da-Lin Jin, Jing-Song Hong, and Han Xiong

Institute of Applied Physics
University of Electronic Science and Technology, Chengdu, 610054, China
jindalinyu@163.com, cemlab@uestc.edu.cn, xiong1226han@126.com

Abstract **—** A simplified structure made of double P-like rings (DPLs), printed on only one side of a dielectric substrate was proposed. A metamaterial sample is investigated numerically and experimentally. The results clearly show that the negative refraction occurs at the transmission band, and one very wide left-handed passband is obtained. A circuit model is also carried out to be a further analysis of the DPLs unit cell.

Index Terms **—**P-rings, left-handed material (LHM), metamaterials, double negative (DNG), wideband metamaterials.

I. INTRODUCTION

Metamaterials is a sort of artificial composite material, in which both the electric permittivity (ε) and the magnetic permeability (μ) are negative. Since Smith first experimented the combination of split ring resonators (SRRs) and continuous wires [1, 2], LHMs have attracted a great amount of attention from researchers in view of their novel characteristics and fabrications [3-10]. Then many structures are proposed, such as, symmetrical-rings [11], Ω-shaped [7], and S-shaped [12, 13]. SRRs are magnetoelectric particles making bianisotropic materials where the rod induced electric resonance and split-ring provided magnetic resonance. The Ω-shaped geometries are printed in reverse directions, yielding a material, in which electric and magnetic effects are separate like the SRRs. Then Chen proposed the symmetric S-shaped configuration, in which there is no obvious electric and magnetic response. Most of above-mentioned structures are printed on both sides of the substrates and has a narrow band, which faced many problems from fabrication and application.

In contrast, we proposed a novel single-sided double P-like left-handed metamaterial. The unit cell of the DPLs structure was introduced detailly, in which bandwidth is extended and the loss is very low. From an experimental point of view, this structure can be easily fabricated and used in real-life applications. The DNG passband is obtained by overlapping the negative permeability and the permittivity. The electric and magnetic resonances can be easily tuned by the parameters, such as width, length, and distances. Then the negative permittivity can coincide with the negative permeability by tuning these variables. The two rods induced the electric response, and the magnetic response is due to antiparallel current distribution between two rings and the adjacent wires [14]. Using the scattering parameters, obtained by HFSS, the complex constitutive effective parameters of the metamaterial are retrieved. A sample is fabricated and tested in a waveguide measurement setup. Also, an equivalent circuit of the unit cell is given to verify the results.

II. UNIT-CELL DESIGN AND SIMULATION

The unit cell of the DPLs is shown in Fig. 1, where the metallic strip is printed on one side of $h=0.508mm$ thick substrate Rogers5880 (ε_r=2.2) and the metallization is a 0.018 mm copper. Dimensions of the unit cell are: a=5.05mm, b=4.5mm, c=2.5mm, $a1$=1.3mm, $w1$=$w2$=0.3mm, $b1$=3.5mm, L=2.575mm, s=0.1mm, $s1$=$s2$=0.2mm. In order to verify the DPLs, numerical simulations were first carried out using HFSS. The electromagnetic wave is incident along the x direction with an electric field polarized in the y direction. This structure can be stacked along

Submitted On: July 4, 2012
Accepted On: Nov. 10, 2012

z direction without space as it is printed on only one side of the dielectric medium. The novel method simplified the manufacturing process.

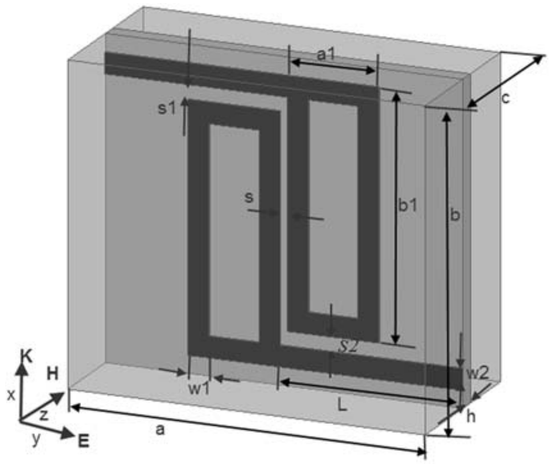

Fig. 1. Geometry of the double-P unit cell.

There are many known methods to retrieve constitutive parameters of metamaterials [2,15-18], scattering parameters are used mostly to obtain impedance z and effective refractive index n. The refractive index and the wave impedance can be related as follows:

$$n=\frac{1}{kd}\cos^{-1}\left(\frac{1-S_{11}^{2}+S_{21}^{2}}{2S_{21}}\right),\ z=\sqrt{\frac{(1+S_{11})^{2}+S_{21}^{2}}{(1-S_{11})^{2}+S_{21}^{2}}} \qquad (1)$$

Then we can calculate the $\varepsilon = n/z$ and $\mu = nz$. It must be mentioned that most of the retrieval procedures obtained the *z* and *n* used only one unit cell and assumed the results of period structures will be the same as for a single unit cell.

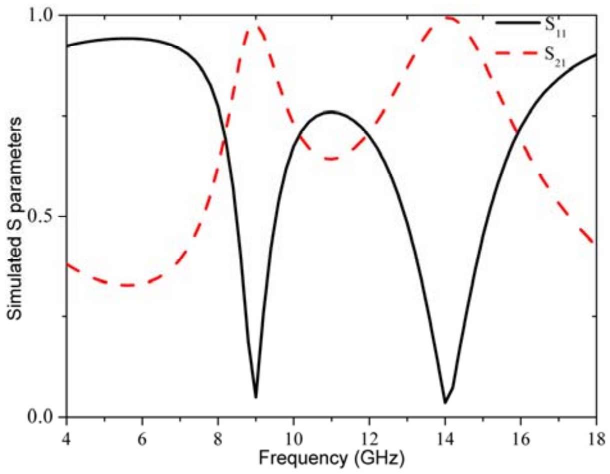

Fig. 2. The simulated S parameters.

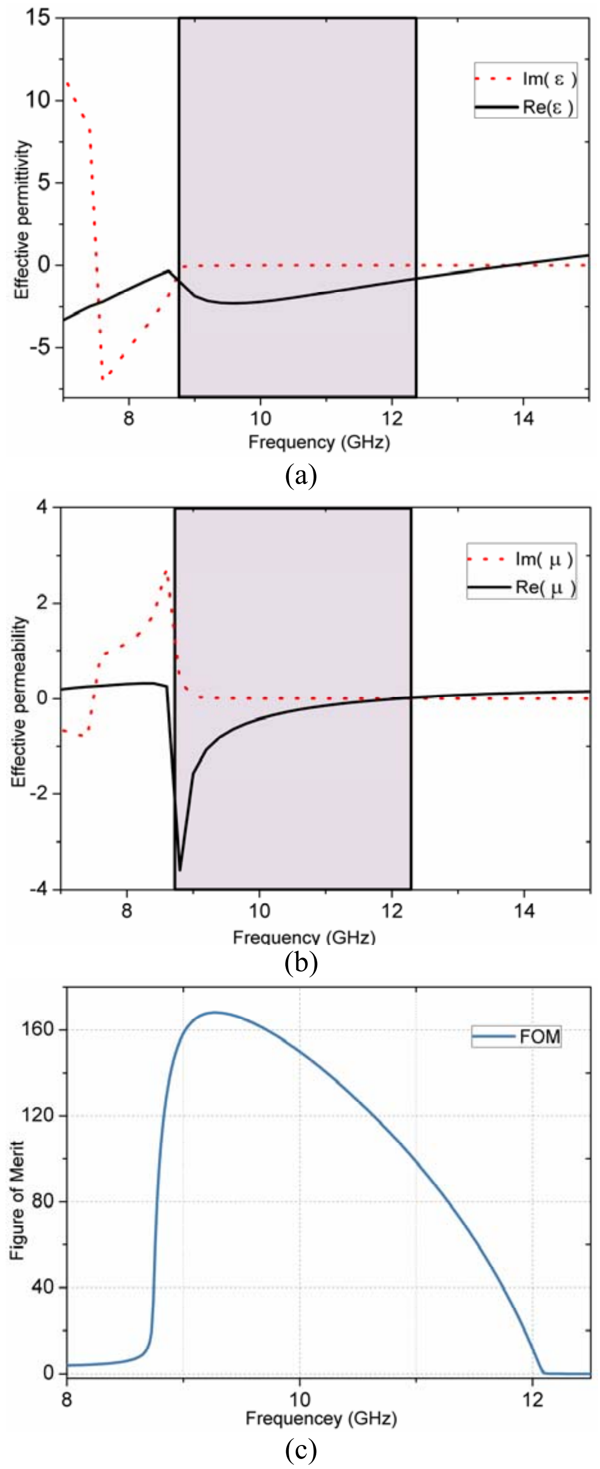

(a)

(b)

(c)

Fig. 3. Retrieved effective parameters. Real (solid line) and imaginary (dashed line) part. (a) permittivity, (b) permeability, (c) figure of merit for the unit cell.

The simulated reflection and transmission spectra are given in Fig. 2, as we can see, at the low frequency side, the transmission is high and approaches 0.98 near 9GHz. Figure 3 clearly depicts the retrieved effective parameters. The effective permittivity is negative in 7.8-13.5GHz, while the effective permeability is negative in 8.75-12.2GHz, respectively. By overlapping the negative permittivity and the permeability, we obtain a wide negative frequency passband, and the relative frequency band is 33.5%. From Fig. 3(c), the figure of merit (FOM), which is a factor of loss and defined as $\left|\mathrm{Re}(n)/\mathrm{Im}(n)\right|$, is from 168 to 14.3 for the DNG band (8.75-12.2GHz). And outside the passband, the FOM is near zero. This indicates that this left-handed metamaterial performs well in the DNG band and can be a good candidate for the potential real-life applications. The equivalent circuit of the unit cell is also given in Fig. 4. The electric and magnetic resonant behaviours are due to a number of capacitances and inductances within this structure, where the C_i (i=1,2,3) are the gap capacitances, L_1 and L_2 are the inductances of the two lines, L_{p1}, L_{p2} and *Cp1, Cp2* are the inductances and capacitances of the two rings.

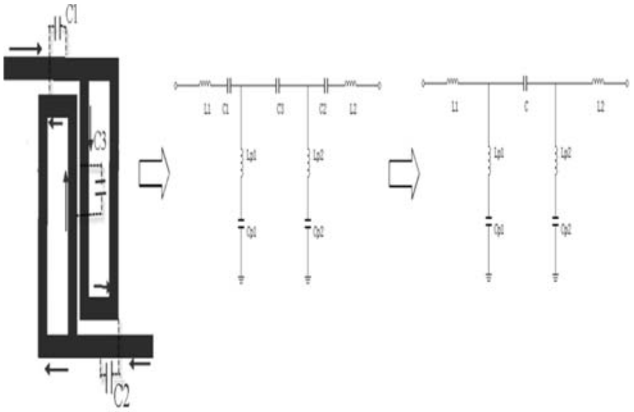

Fig. 4. The equivalent circuit of the unit cell.

The current distribution of the unit cell at 10GHz is given in Fig. 5, which confirms the equivalent circuit analysis in Fig. 4. As one can see in Fig. 5, there exist three gaps in this structure, on two sides of these gaps (*s, s1, s2*), the currents is antiparallel which induced the magnetic response. And the electric response is attributed to the plasma-electron oscillations of the two cut wires.

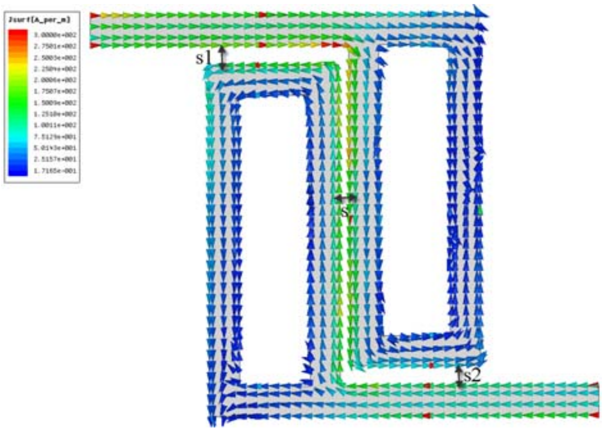

Fig. 5. Surface current distribution for the double P-like structure at 10GHz.

Here, with detailed simulations, the dependence of the magnetic resonance f_m and the electric resonance f_e is shown in Fig. 6. As shown in Fig. 6(a), 6(b), and 6(c), f_m and f_e are linear functions of 1/a1, 1/b1, and 1/L. Figure 6(d) shows that f_m is proportional to s and f_e is inversely proportional to s while it changes from 0.1 mm to 0.5 mm.

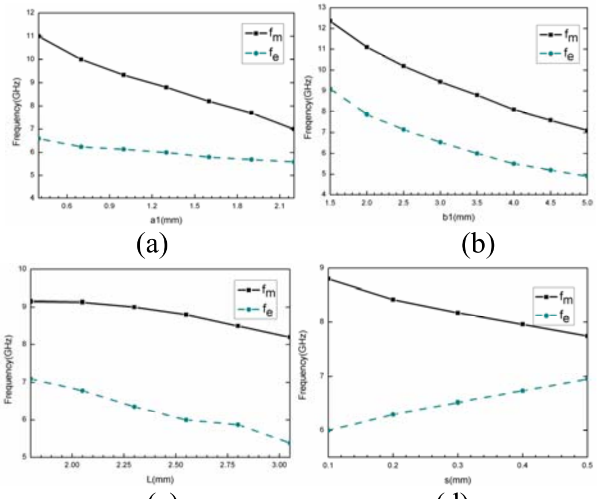

(a) (b)

(c) (d)

Fig. 6. Magnetic resonance frequency f_m and electric resonance f_e versus (a) the width of the ring, (b) the height of the ring, (c) the length of the branch, (d)the distance of the two P-like rings.

III. EXPERIMENT VERIFICATION

The proposed double P-shaped resonator was also manufactured and tested. In practical fabrications, periodic array is 2 unit cells along *x* and *y* direction. And there is no need for spacers between stacked layers in *z* direction. The sample is put into a standard waveguide BJ100. Scattering parameters were measured by Agilent E8361A [19, 20]. The measured S_{11} and S_{21} parameters are shown in Fig. 7. The transmission peak is near the 9 GHz respectively. A closer view of fabricated sample and its direction inside the waveguide are also depicted in Fig. 7.

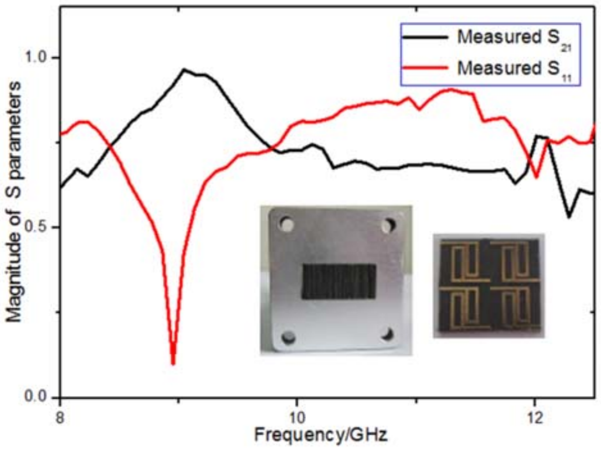

Fig. 7. Measured S parameters.

Figure 8 illustrates the real part and the imagery part of the permittivity and the permeability. It can be seen that the real part of effective permittivity is negative in 8.8-12.5GHz, while the real part of effective permeability is negative in 8.8-12.2GHz. Thus, the DNG band is 8.8-11.8GHz. Comparing the simulated DPL unit cell, the refraction index is negative in 8.75-12.2GHz. Note the measured DNG band is narrower than the simulated one. The difference may be caused by the fabrication error, such as the layers are not precisely parallel and the cut-wires did not touch the waveguide wall completely.

IV. CONCLUSION

A novel single-sided double P-shaped resonator has been proposed. Both the numerical simulation and the experiment have confirmed the obvious transmission peak and the negative effective permittivity, permeability, and the negative refraction index happened around the resonant frequency peak. In addition, this single-sided structure has a wide band and can be easily fabricated. Thus, this novel geometry can be used in various potential real-life applications and this manufactured LHM can be a good candidate for being used optical metamaterial.

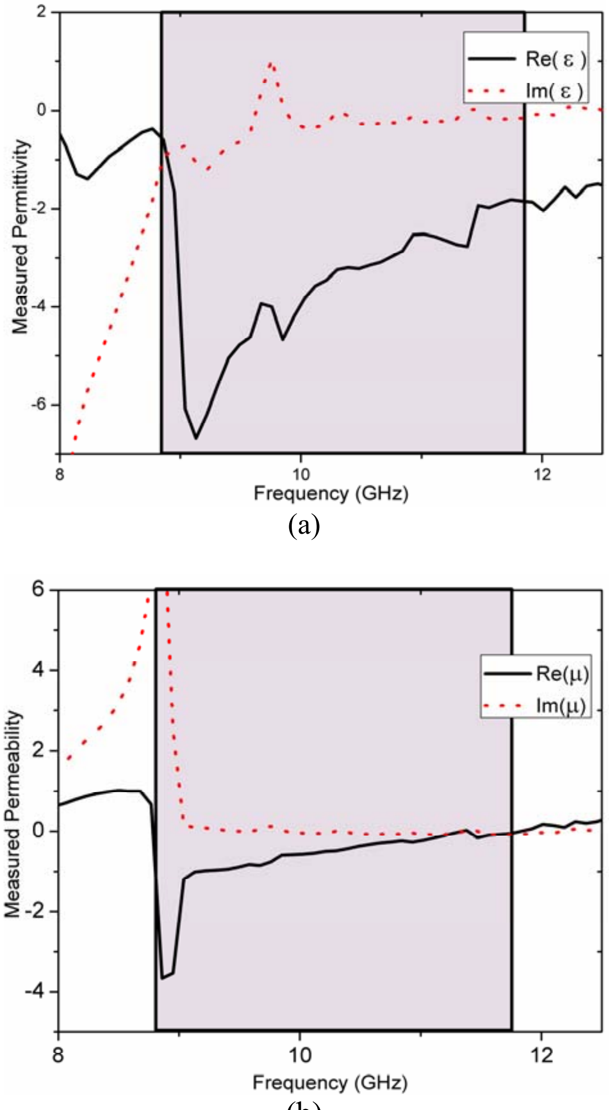

(a)

(b)

Fig. 8. Measured effective parameters.

ACKNOWLEDGMENT

This work was supported by the National Natural Science Foundation of China (No. 61172115 and No. 60872029), the High-Tech Research and Development Program of China (No. 2008AA01Z206), the Aeronautics Foundation of China (No. 20100180003), and the Fundamental Research Funds for the Central Universities (No. ZYGX2009J037).

REFERENCES

[1] D. R. Smith, W. J. Padilla, D. C. Vier, S. C. Nemat-Nasser, and S. Schultz, “Composite Medium with Simultaneously Negative Permeability and Permittivity,” *Phys. Rev. Lett.,* vol. 84, no. 18, pp. 4184-4187, May 2000.

[2] D. R. Smith, D. C. Vier, N. Kroll, and S. Schultz, “Direct Calculation of Permeability and Permittivity for a Left-Handed Metamaterial,” *Appl. Phys. Lett.,* vol. 77, no. 14, pp. 2246-2248, Oct. 2000.

[3] J. Valentine, S. Zhang, T. Zentgraf, E. Ulin-Avila, D. A. Genov, G. Bartal, and X. Zhang, “Three-Dimensional Optical Metamaterial with a Negative Refractive Index,” *Nature*, vol. 455, pp. 376-U32, 2008.

[4] M. C. Tang, S. Q. Xiao, D. Wang, J. Xiong, K. Chen, and B. Z. Wang, “Negative Index of Reflection in Planar Metamaterial Composed of Single Split-Ring Resonators,” *Applied Computational Electromagnetics Society (ACES) Journal,* vol. 26, no. 3, pp. 250-258, Mar. 2011.

[5] A. V. Kildishev and U. K. Chettiar, “Cascading Optical Negative Index Metamaterials,” *Applied Computational Electromagnetics Society (ACES) Journal,* vol. 22, pp. 172-183, Mar. 2007.

[6] M. R. I. Faruque, M. T. Islam, and N. Misran, "Evaluation of EM Absorption in Human Head with Metamaterial Attachment," *Applied Computational Electromagnetics Society (ACES) Journal*, vol. 25, pp. 1097-1107, 2010.

[7] J. Huangfu, L. Ran, H. Chen, X. Zhang, K. Chen, T. M. Grzegorczyk, and J. A. Kong, “Experimental Confirmation of Negative Refractive Index of a Metamaterial Composed of Ω-like Metallic Patterns,” *Appl.Phys. Lett.,* vol. 84, no. 9, pp. 1537-1539, Mar. 2004.

[8] D. L. Jin, J. S. Hong, H. Xiong, “Dual Wideband Antenna for WLAN/WiMAX and Satellite System Applications Based on a Metamaterial Transmission Line,” *Chin. Phys. Lett.,* vol. 29, no. 10, pp. 104101-104101-3, Oct. 2012.

[9] M. Fallah, A. A. Heydari, A. R. Mallahzadeh, and F. H. Kashani, “Design and SAR Reduction of the Vest Antenna using Metamaterial for Broadband Applications,” *Applied Computational Electromagnetics Society (ACES) Journal*, vol. 26, pp. 141-152, 2011.

[10] A. V. Kildishev, and U. K. Chettiar, “Cascading Optical Negative Index Metamaterial,” *Applied Computational Electromagnetics Society (ACES) Journal*, vol. 25, no. 8, pp. 696-702, Aug. 2010.

[11] T. M. Grzegorczyk, C. D. Moss, J. Lu, X. D. Chen, J. Pacheco, Jr., and J. A. Kong, “Properties of Left-Handed Metamaterials: Transmission, Backward Phase, Negative Refraction, and Focusing,” *IEEE Trans. Microw. Theory Tech.,* vol. 53, no. 9, pp. 2956-2967, Sept. 2005.

[12] H. Chen, L. Ran, J. Huangfu, X. Zhang, K. Chen, T. M. Grzegorczyk, and J. A. Kong, “Left-Handed Materials Composed of Only S-Shaped Resonators,” *Phys. Rev. E,* vol. 70, no. 5, pp. 57605-57605-4, Nov. 2004.

[13] M. F. Khan, M. J. Mughal, and M. Bilal, "Effective Permeability of an S-Shaped Resonator," *Microw. Opt. Technol. Lett.,* vol. 54, pp. 282-286, 2012.

[14] Z. Dong, M. Xu, S. Lei, H. Liu, T. Li, F. Wang, and S. Zhu, “Negative Refraction with Magnetic Resonance in a Metallic Double-Ring Metamaterial,” *Appl. Phys. Lett.,* vol. 92, no. 6, pp. 064101-064101-3, Feb. 2008.

[15] D. R. Smith, D. C. Vier, T. Koschny, and C. M. Soukoulis, “Electromagnetic Parameter Retrieval from Inhomogeneous Metamaterials,” *Phys. Rev. E*, vol. 71, 2005.

[16] G. Lubkowski, R. Schuhmann, and T. Weiland, “Extraction of Effective Metamaterial Parameters by Parameter Fitting of Dispersive Models,” *Microw. Opt. Technol. Lett.,* vol. 49, no. 2, pp. 285-288, Feb. 2007.

[17] R. Zhao, T. Koschny, and C. M. Soukoulis, “Chiral Metamaterials: Retrieval of the Effective Parameters With and Without Substrate,” *Opt. Exp.*, vol. 18, pp. 14553-14567, 2010.

[18] X. D. Chen, T. M. Grzegorczyk, B. I. Wu, J. Pacheco, and J. A. Kong, “Robust Method to Retrieve the Constitutive Effective Parameters of Metamaterials,” *Phy. Rev. E*, vol. 70, 2004.

[19] R. W. Ziolkowski, “Author Reply to Comments on "Design, Fabrication, and Testing of Double Negative Metamaterials”,” *IEEE Trans. Antennas Propag.,* vol. 53, no. 2, pp. 891-892, Feb. 2005.

[20] H. Chen, J. Zhang, Y. Bai, Y. Luo, L. Ran, Q. Jiang, and J. A. Kong, “Experimental Retrieval of the Effective Parameters of Metamaterials based on a Waveguide Method,” *Opt. Exp.,* vol. 14, no. 26, Dec. 2006.

Da-lin Jin was born in Sichuan, China. She received her B.S. degree in Electronics Information Science and Technology from Chengdu University of Information Technology in 2010. She is a graduate student major in Radio Physics in the University of Electronic Science and Technology of China now. Her research interests include left-handed metamaterials technology and the applications of antenna with metamaterials.

Jing-song Hong received the B.Sc. degree in electromagnetics from Lanzhou University, China, in 1991, and the M.Sc. and Ph. D. degrees in electrical engineering from the University of Electronic Science and Technology of China (UESTC), in 2000 and 2005, respectively. He is now a professor with UESTC. From 1991 to 1993, he was a Circuit Designer with the Jingjiang Radar Factory, Chengdu, China. From 1993 to 1997, he was a Testing Engineer with SAE Magnetics (HK) Ltd, Guangdong, China. From 1999 to 2002, he was a Research Assistant with the City University of Hong Kong. His research interest includes the use of numerical techniques in electromagnetics and the use of microwave methods for materials characterization and processing.

Han Xiong was born in HuBei. He received his M.Sc. from Yunnan Normal University in 2010. He is a doctor in Radio Physics of the University of Electronic Science and Technology of China now. His research interests include antenna technology and metamaterials.

Photonics Bandgap Computations using Novel Periodic Meshless Methods

Hooman Razmjoo [1], Masoud Movahhedi [2], Ali Aminian [2], and Tinh Quoc Bui [3]

[1] Department of Electrical Engineering
Shiraz University, Shiraz, Iran
H.razmjoo@gmail.com

[2] Department of Electrical Engineering
Shahid Bahonar University of Kerman, Kerman, Iran
Aminian129@gmail.com, Movahhedi@ieee.org

[3] Department of Civil Engineering
University of Siegen, Siegen, D-57076, Germany
Tinh.buiquoc@gmail.com

Abstract **—** Although many numerical methods have been developed to calculate photonic bandgap structure properties, but always improvement in numerical methods is necessary to have more efficient, accurate and flexible techniques. In the present work, novel periodic meshless shape functions including so-called direct and radial shape functions are presented. The meshless approaches, based on these periodic shape functions as real-space methods, can be used for simulation of periodic structures, like photonics bandgap structures, straightforwardly. The results on band structures derived from the proposed methods are then presented, discussed and compared with those available in the literature, and a very good agreement is seen. It shows that the proposed techniques are very promising to be robust techniques in the simulation of periodic structures such as photonic problems.

Index Terms **—** Meshless methods, photonics bandgap, periodic shape functions.

I. INTRODUCTION

Accurate simulation of bandgap structures is indispensable development of various opto-electromagnetic devices [1], [2]. The major groups of the band structure materials have periodic constructions. It is common to analyze periodic geometries by assuming that the structure extends to infinity in one or more directions. Sometimes, this is done in order to simplify the analysis. But the infinite structure can also be viewed as the ideal structure because there are no truncation edges present to possibly degrade the electromagnetic performance. When the structure extends to infinity, it is possible to analyze the electromagnetic performance by considering only one period of the geometrical pattern, i.e. a unit cell. Periodicity and antiperiodicity geometry aspects can be able to reduce the complexities of studied domain of the device [3].

One of the well-known techniques in analyzing photonics bandgap problems is the plane wave method. But this conventional technique has convergence problem arising from the abrupt change in the value of dielectric function across

Submitted On: Aug. 24, 2012
Accepted On: Nov. 8, 2012

the interface between matrix and inclusion [4]. Thus, real-space numerical methods have also been tried for more efficient calculations of photonic band structures. Among them, the periodic finite-difference time-domain (FDTD) method [3] and the periodic finite element method (FEM) [5] are commonly used. The main advantage of using the FEM for infinite periodic analysis compared to the FDTD is the ease of use unstructured grids that can model complex structures with large variation in length scale as well as elements that can better conform to curved boundaries. The computation accuracy of the FEM, however, depends upon the quality of the used mesh. In addition, the meshing process is also known as a very complex and time consuming task.

Unlike the conventional element-based numerical methods, meshless methods expand the field quantities around a set of scattered nodes that can be randomly placed spatially in a problem domain [6]. As a result, their numerical accuracies are independent on the connectivity laws of the grid nodes. In addition, any irregular shape of interface between materials is easily recognized in meshless modeling by simply putting nodes along the interface, e.g., photonic crystals or other metamaterials which they can have any arbitrary shape dielectrics. One of the other unique potential applications for meshless methods is that the methods may be well-suited to adaptive computation which is needed in some devices like liquid crystal materials. Owing to these distinctive features, meshless methods have been introduced as robust and flexible computational methods in a variety of engineering areas, confidently.

To our best knowledge, a few studies have been done on using meshless methods for analyzing periodic structures. This is due to this fact that the shape functions are usually global in the conventional meshless methods and introducing periodic boundary conditions are inherently different from other methods. So, for solving this problem in meshless approach, by implementing periodic shape functions, periodic boundary conditions can be imposed spontaneous. In [7], the author proposed a technique for constructing periodic mean least-square (MLS) shape functions. But as it is known, MLS shape functions do not have the delta function property and thus imposing essential boundary conditions would not be performed, straightforwardly. On the other hand, recently, some other approximations or shape functions, called direct shape functions (DSFs), have been proposed which can be created directly and be more efficient [8], [9]. In this work, a new technique is introduced to generate periodic meshless shape functions. The proposed technique is applied to DSFs and shape functions used in radial point interpolation method (RPIM) [6] to obtain periodic shape functions. Then, the proposed periodic shape functions are employed to calculate the eigenvalues and the eigenfunctions of the electric field in a photonic bandgap structure.

II. PERIODIC SHAPE FUNCTION CONSTRUCTION

Here, we introduce a simple technique to construct inherently suitable shape functions for periodicity. Our proposed technique is enforced on the weighting or basis functions then it would be affected on the shape functions, straightforwardly. In Fig. 1, a periodic domain with generic parallelogram cell is shown. The lattice vector $\vec{L}$ is denoted by

$$\vec{L} = n_1\vec{a}_1 + n_2\vec{a}_2 \tag{1}$$

where $\vec{a}_1$, $\vec{a}_2$ are primitive lattice vectors and n_1, n_2 are integers. In meshless approach, a unit cell is discretized by a set of nodes $i = 1,2,\cdots,N$. Because of periodic nature of the structure, the field will change in a periodic manner in the problem domain. So

$$u(X) = u(X + \vec{L}) \tag{2}$$

for any point X in the unit cell. In periodic approach, dual points of a node such as X should be found, first. It can be easily performed using the components of the lattice vector as

$$X'_{pq} = X + pn_1\vec{a}_1 + qn_2\vec{a}_2 \tag{3}$$

where $p,q = -M,-M+1,\cdots,M-1,M$ and M is a large integer. X'_{00} is actual point and the others X'_{pq} are named dual points. So in fact, there are too many dual points for each point in the unit cell. But, it should be noted that only those dual points which are located in the neighbour cells are usually important. For example, in a tetrahedron cell, there are eight neighbour cells. In the parallelogram cell, the lattice vector has two components $\vec{a}_1$ and $\vec{a}_2$ and each point has eight dual points, i.e., 3^2-1 in the neighbour cells. These points can be obtained from (3) by setting $p,q=-1,0,1$. It should be carefully noted, although, in a generic periodic structure like Fig. 1, there are some dual points, but generally only a few numbers of them must be considered. In fact, the others have a considerably remote distance from X_I which is obvious and recognizable. For example in Fig. 1, for point *X* there are eight dual points in the neighbour cells, but only three nearer dual points should be considered. For example, let the considered point be in the lower left corner of the tetrahedron. It is clear that the dual point which is in the top cell, does not have a distance smaller than the actual distance.

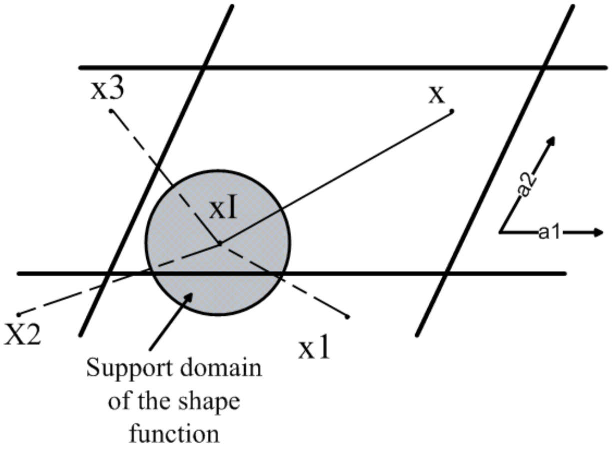

Fig. 1. A generic point in one of the shape function support domains in a unit cell. An actual point *X* and its three dual points, i.e. X_1, X_2, X_3, are shown. To determine the periodic shape function corresponding to X_I in point *X*, the shortest distance or the shortest line, i.e. dash line shown in the figure, must be used.

According to the lattice structure, the number of dual points is clear and we cannot increase or decrease them. Also, the number of dual points considered must be obtained carefully and exactly.

As it is known, in the meshless methods corresponding to each scattered node, there is a weighting or basis function $W_i(X)$. For example, in direct meshless method proposed in [8] it is as

$$W_i(X)=\exp(-\alpha|X-X_i|) \qquad (4)$$

where X is the vector of space coordinates, i.e. $X^T=[x,y]$ (for 2D problems), and X_i is the space coordinate of the node that related to the weighting function. α is a positive independent coefficient. In proposed approach to have a periodic weighting function, a modification on (4) should be performed. By introducing

$$X_{nearest}=X_{nm} \quad \text{if} \quad |X_{\mathrm{mn}}-X_i| \le |X_{\mathrm{pq}}-X_i| \qquad (5)$$

Then a periodic weighting function can be proposed as

$$W_i(X)=\exp(-\alpha|X_{nearest}-X_i|) \qquad (6)$$

Above formula means that to construct a periodic shape function at a generic point *X*, first, the points of *X* should be obtained and then the nearest point to the center of the shape function, according to (5), would be used instead of *X* in the conventional basis function formula. This idea comes from this fact that the field in nonperiodic structures at X_i has a small influence on aloof points from X_i; or in other words, the shape functions $N_i(X)$ would be vanished far away from X_i. Whereas in periodic structures, an aloof point may have a dual point which can be closed to X_i. On the other hand, because any point has the same value of its dual points, so its dual distance can be replaced instead of the actual distance in formulas.

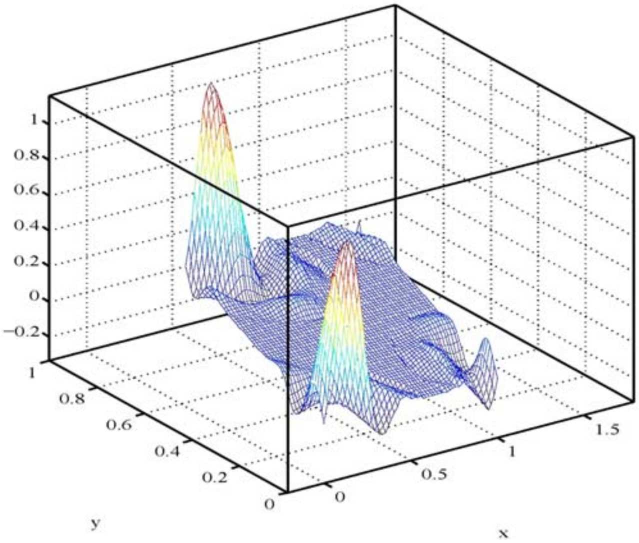

(a)

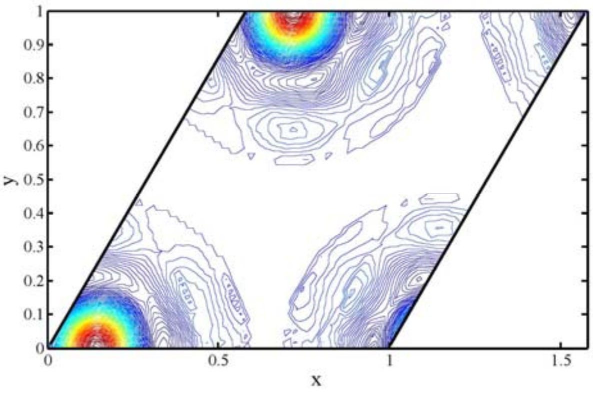

(b)

Fig. 2. The shape function corresponding to a node near the lower left corner. a) 3D demonstration. b) Equal-value contour plot.

This approach can be applied to other meshless shape functions, straightforwardly. In the case of periodic local radial point interpolation method (RPIM) shape functions [6], the support domain of the point of interest must be first determined. For example for a node in the near lower left corner of a lattice, we first find scattered nodes in the support domain of node *X*, then node *X* is translated to $X+\vec{a}_1$ and node search is applied again. The same procedure is repeated for $X+\vec{a}_2$ and for $X+\vec{a}_1+\vec{a}_2$ where $\vec{a}_1,\vec{a}_2$ are primitive lattice vectors. After determining the support domain, the periodic RPIM approximation can be written as

$$u(X)=\sum_i a_i R_i(X) \tag{7}$$

where $R_i(X)$ is the regular radial basis function except for the definition of distance where the new definition of distance discussed above is used, and a_i are unknown coefficients. By letting *u(X)* passes through each scattered node in the support domain, the unknown coefficients can be determined.

Here, the introduced technique is used to make periodic local radial shape function. Figure 2 shows one of the shape functions near the lower left corner of the parallelogram. Periodic nature of the shape function is appeared, clearly, in this figure. The shape function has non-vanishing values near all the four corners as a result of dual point technique. By using these periodic shape functions, meshless method can simulate an indicator unit cell without any other boundary conditions on the periodic boundaries.

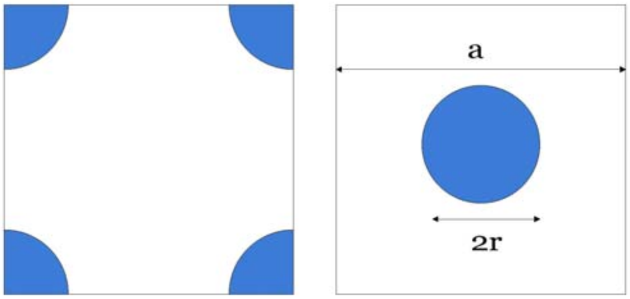

Fig. 3. Two different configurations for the unit cell used to model the desired structure.

III. NUMERICAL EXAMPLE

In this section, we attempt to validate our proposed techniques through numerical experiment by simulating a well-known problem in periodic structures literature. The problem considered is an array of dielectric rods in free space periodically arranged [1]. The structure is assumed to be infinite in *x* and *y* directions both, and is infinitely long in *z* direction. Since the dielectric rods are periodically arranged, and because the structure is infinite in both *x* and *y* directions, we can simply model it by a unit cell to which the proposed periodic meshless methods are employed to calculate its frequency band structures. This problem can be considered as a good test to measure the technique capability in simulating periodic and inhomogeneous regions.

According to the Floquet-Bloch theorem, each components of the electromagnetic fields can be expressed by the product of a periodic function *u(X)*, where *X* is spatial coordinate, and a plane wave with the wave vector $\vec{k}$, such as [7]

$$\varphi(X)=u(X)e^{-i\vec{k}.X} \tag{8}$$

By considering the periodic nature of the wave propagation, problem of obtaining electromagnetic fields is reduced to solving two equations for *u(X)*. For TE mode

$$-\left(\nabla+i\vec{k}\right)\frac{1}{\varepsilon(X)}.\left(\nabla-i\vec{k}\right)u(X)=\lambda u(X) \tag{9}$$

and for TM mode

$$-\left(\nabla+i\vec{k}\right)\left(\nabla-i\vec{k}\right)u(X)=\varepsilon(X).\lambda u(X) \tag{10}$$

where $\lambda=(\omega/c)^2$, c is the light velocity and ε is the relative permittivity of the medium.

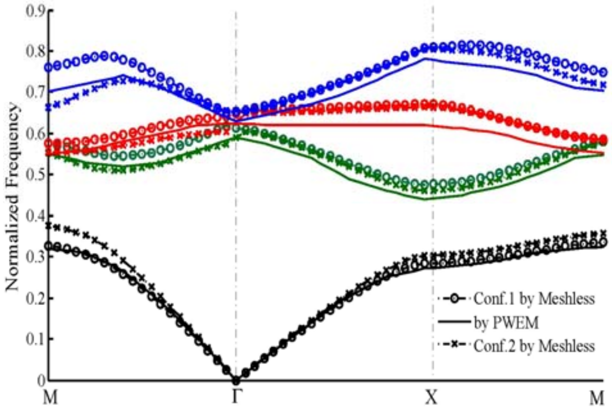

Fig. 4. Meshless results on band structures of square lattice composed of circular rods calculated by the periodic DSF for two configurations (TM mode).

In the meshless method, the field function, i.e., $\varphi(X)$ or *u(X)*, would be approximated

$$\tilde{u}(X)=\sum_{i=1}^{N_p} a_i.\psi_i(X) \tag{11}$$

where a_i are unknown constants, N_p denotes the number of nodes and ψ_i are periodic shape functions. Manipulations after putting equation (11) into equations (9) and (10) and forming Galerkin's formulations for them, result in matrix eigenequations as

$$[A][a]=\lambda[B][a] \tag{12}$$

where for TE mode

$$\begin{gathered}A_{ij}=\int_\Omega \frac{1}{\varepsilon(X)}\left(\nabla+i\vec{k}\right)\psi_i(X).\left(\nabla-i\vec{k}\right)\psi_j(X)d\Omega\\ B_{ij}=\int_\Omega \psi_i(X).\psi_i(X)d\Omega\end{gathered} \tag{13}$$

and for TM mode

$$\begin{gathered}A_{ij}=\int_\Omega \left(\nabla+i\vec{k}\right)\psi_i(X).\left(\nabla-i\vec{k}\right)\psi_j(X)d\Omega\\ B_{ij}=\int_\Omega \varepsilon(X)\psi_i(X).\psi_i(X)d\Omega\end{gathered} \tag{14}$$

The radius of the circular cross section, as shown in Fig. 3, is $r=0.2a$ for this example. Dielectric constants are $\varepsilon_m=1.0$ and $\varepsilon_1=8.9$ for matrix and rods, respectively. According to Bloch's state in periodic structures, the wave numbers in the Brillouin zone are only needed to be considered.

We use two different unit cells for this problem, one configuration with a rod in the center of the cell (Conf. 1) and in the other one the unit cell is chosen so that one quarter of four rods are in each corner of the lattice (Conf. 2), as shown in Fig. 3. Since these two problems are similar to each other, we expect that the frequency band diagrams obtained by applying periodic meshless methods to these two unit cells be the same, too. The results will show it is indeed the case. It can be considered as an initial criterion of the accuracy of the results. In this study we have used multi-quadrics (MQ) RPIM shape functions with shape parameters chosen as *q=0.98* and $\alpha_c=0.5$ [6]. Moreover, the problem domain is discretized by *417* nonuniform meshless nodes. For DSF approach, the shape parameter $\alpha=3/d_c$, where d_c is the average nodal spacing, is chosen with the same meshless nodes [8].

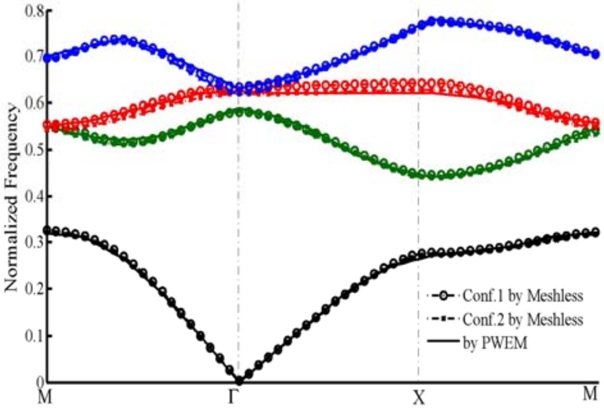

Fig. 5. Meshless results on band structures of square lattice composed of circular rods calculated by the periodic RPIM for two configurations (TM mode).

In this case, there exists a wide bandgap in TM modes as known in literature [7]. Meshless results on band structures also confirm the wide bandgap in TM modes as shown in Figs. 4 and 5 for both DSF and RPIM approaches, respectively. In these diagrams, the normalized frequency is drawn for different modes versus wave number, i.e., $\vec{k}$, in Brillouin zone. The results have a good agreement with those obtained by other methods such as the plan wave expansion method (PWEM) [10]. Although, the DSF meshless method accuracy is less than the accuracy of the RPIM meshless method, its simulation time is better than RPIM method as known as one of the advantages of direct meshless methods [8], [9]. Table 1 illustrates the consuming time for shape function construction in two comparable methods, the proposed method and the RPIM approach.

Table 1: Consuming time for two different meshless approach

	Computational time (sec)	
Number of nodes	**RPIM method**	**Direct method**
289	5	2
361	10	3
441	25	7
529	58	13
625	110	20

It can be seen, when the number of nodes increases, the RPIM method processing time increases, extremely. All simulations were performed on the same PC with a CPU of 2.4 GHz and a RAM of 2 GB.

IV. CONCLUSION

We have presented successfully a new 2D meshless method applicable to analyze any infinite periodic structures, like photonic crystals. The periodic radial and direct shape functions, as two advanced meshless shape functions, based on the proposed approach were introduced and a 2D photonic crystal structure was simulated. In this approach, any complex dielectric boundaries can be modeled only by putting nodes on the boundaries, effortlessly. The photonic bandgap structure was analyzed and the obtained results matched well with the reference solutions. It thus demonstrates that the periodic meshfree shape functions implemented are very efficient for the problems of periodicity. The periodic approach has been presented in 2D quadrilateral cell, but generally 3D cells could be possible.

Nevertheless, this paper presented a simple bandgap problem. But more complicate problems can be investigated in the future such as photonic crystals with nonlinear and anisotropic materials or application of the time-domain meshless method in photonic structures, etc. In the other words, the proposed method is applicable to each periodic structure with no limitations.

REFERENCES

[1] J. D. Joannopoulos, S. G. Johnson, J. N. Winn, and R. D. Meade, *Photonic Crystals: Modeling the Flow of Light.* Princeton University Press, 2008.

[2] K. Busch, “Photonic Band Structure Theory: Assessment and Perspectives,” *C. R. Physique*, vol. 3, pp. 53-66, 2002.

[3] Y. Hao and R. Mittra, *FDTD Modeling of Metamaterials, Theory and Applications*, Artech House Press, 2009.

[4] H. S. Sozuer, J. W. Haus, and R. Inguva, “Photonic Bands: Convergence Problems with the Planewave Method,” *Phys. Rev. B*, vol. 45, pp. 13962-13972, 1992.

[5] L. E. R. Petersson, and J. M. Jin, “A Three-Dimensional Time-Domain Finite-Element Formulation for Periodic Structures,” *IEEE Trans. Antennas Propag.*, vol. 54, no. 1, pp. 12-19, 2006.

[6] G. R. Liu and Y. T. Gu, *An Introduction to Meshfree Methods and their Programming,* Springer, New York, 2005.

[7] S. Jun, “Meshfree Implementation for the Real-Space Electronic-Structure Calculation of Crystalline Solids,” *Int. J. Numer. Meth. Eng,* vol. 59, pp. 1909-1923, 2004.

[8] H. Razmjoo, M. Movahhedi, and A. Hakimi, “A Modification on a Fast Meshless Method for Electromagnetic Field Computations,” *IET Sci. Meas. Technol,* vol. 5, no. 5, pp. 185-192, 2011.

[9] H. Razmjoo, M. Movahhedi, and A. Hakimi, “An Efficient Meshless Method based on a New Shape Function,” *Int. J. Numer. Model.*, vol. 23, no. 6, pp. 503-521, 2010.

[10] P. R. Villeneuve, M. Piche, “Photonic Band Gaps in Periodic Dielectric Structures,” *Progress in Quantum Electronics*, vol. 18, pp. 153-200, 1994.

Analysis of Thin Microstrip Antennas by Meshless Methods

B. Honarbakhsh[1], **A. Tavakoli**[1, 2]

[1]Department of Electrical Engineering
[2]Institute of Communications Technology and Applied Electromagnetics
Amirkabir University of Technology (Tehran Polytechnic), Tehran, IRAN
b_honarbakhsh@aut.ac.ir, tavakoli@aut.ac.ir

Abstract **─** In this paper, different meshless methods are applied to the analysis of microstrip antennas with thin substrate. Comparison is made between the performance of the methods with respect to convergence, CPU time and condition number of final coefficient matrix. The exact modal solution and method of moments are used for validation. The input impedance results of all methods are in agreement with each other.

Index Terms **─** LBIE, meshless, microstrip antenna, MLBE, MLPG.

I. INTRODUCTION

Meshless methods are powerful tools for numerical solution of partial differential equations (PDEs) [1]. Up to now, these methods have been widely used in mechanical engineering, but with limited use in electrical engineering [2]-[17]. Evidently, the purpose of meshless methods is elimination of mesh in discretization of operator equations. This goal necessitates the design of fitting strategies for scattered data in multidimensional spaces. This attempt resulted in the emergence of meshless shape functions with superb fitting capability. Consequently, expanding the unknown field variable over such functions not only makes it possible to solve problems meshfree, but also decreases the number of unknowns in the corresponding system of equations. In general but not necessarily, these two intrinsic benefits are accomplished at the expense of computational cost. In this work, we have applied different meshless methods such as *meshless local Petrov-Galerkin* (MLPG) [18], *local boundary integral equation* (LBIE) [19] and *meshless local boundary equation* (MLBE) [20] to the analysis of microstrip antennas with thin substrate. A rectangular-coax-fed, a square-line-fed and a two-element array antenna are analyzed. The aforementioned methods are compared with each other from the aspects of convergence, CPU time and condition number of the corresponding linear systems. In order to highlight the capabilities of meshless methods, various node arrangements for describing the problem domains are used including uniform, non-uniform and random. Clearly, by imposing a logical irregularity in accordance with the geometry and physical sense of a problem, the number of unknowns could be considerably decreased.

The results are validated by the exact modal solution for the coax-fed antenna case and the method of moments (MoM) for the others. It is observed that all meshless methods have essentially the same convergence rates. However, LBIE is seen to be the most well-conditioned and the MLBE the fastest.

II. MATHEMATICAL STATEMENT OF THE PROBLEM

Microstrip structures with thin substrate are *planar* microwave components [21]. By this assumption, variations normal to the substrate become negligible and consequently, Maxwell's equations simplify to a two-dimensional (2D) scalar Helmholtz equation with homogeneous Neumann boundary conditions. In addition, coax excitation ports can be well modeled by Dirac delta functions. Suppose a planar microstrip structure placed on the *x-y* plane, with the domain and boundary of Ω and $\Gamma(\equiv\partial\Omega)$, respectively.

Submitted On: June 3, 2012
Accepted On: Nov. 8, 2012

Based on these assumptions, the mathematical statement of the problem corresponding to a single feed antenna is:

$$\begin{cases} \left(\nabla^2 + k^2\right) E_z = j\omega\mu_0 \delta\left(\mathbf{x} - \mathbf{x}_p\right), & \mathbf{x} \in \Omega \\ \mathbf{n} \cdot \nabla E_z = 0, & \mathbf{x} \in \partial\Omega \end{cases}, \tag{1}$$

where E_z is the component of the electric field normal to the substrate, k is the propagation constant of the field inside the structure, ω is the working angular frequency, μ_0 is the magnetic permeability, $\mathbf{x}_p$ is the position of the excitation port and $\mathbf{n}$ is the normal vector to the boundary. Clearly, (1) can be equivalently written as:

$$\begin{cases} \left(\nabla^2 + k^2\right) u = 0, & \mathbf{x} \in \Omega \\ \mathbf{n} \cdot \nabla u = \bar{q}, & \mathbf{x} \in \Gamma \end{cases}, \tag{2}$$

with:

$$\begin{cases} u = E_z - j\omega\mu_0 \cdot \dfrac{j}{4} H_0^{(2)}\left(k\left|\mathbf{x} - \mathbf{x}_p\right|\right) \\ \bar{q} = -\mathbf{n} \cdot \nabla j\omega\mu_0 \cdot \dfrac{j}{4} H_0^{(2)}\left(k\left|\mathbf{x} - \mathbf{x}_p\right|\right) \end{cases}. \tag{3}$$

We have found that (2) is more proper for meshless discretization, so it is regarded as the mathematical statement of the problem. Our observations of different situations showed that meshless methods are incapable of handling abrupt changes, in the sense of convergence. In fact, we could not get a convergence solution of (1) unless we approximated the Dirac delta by a sharp bell-shaped function. Even by applying this trick, a series of difficulties could be encountered. For example, the sharpness should not exceed a certain level; otherwise, the number of nodes at the vicinity of the excitation should be sufficiently increased to track the function.

Equation (2) cannot be solved unless k is determined. Since in antenna applications a considerable amount of electromagnetic energy should be radiated in free space, the trivial value of the propagation constant in the substrate, i.e., $\omega(\varepsilon\mu)^{1/2}$, is incapable of modeling the behavior of the structure.

An *effective* value for propagation constant, k_{eff}, can be well estimated by the cavity method [22]. The electric field distribution on the antenna can be computed by solution of (2) based on k_{eff}. Once this is done, the input impedance at the antenna port can be evaluated by:

$$Z_{in} = -h \cdot E_z\left(\mathbf{x}_p\right) / I\left(\mathbf{x}_p\right), \tag{4}$$

where h is the height of substrate and I the source current defined as:

$$I\left(\mathbf{x}_p\right) = \begin{cases} 1, & \mathbf{x} = \mathbf{x}_p \\ 0, & \mathbf{x} \neq \mathbf{x}_p \end{cases}. \tag{5}$$

In general, this procedure is iterative but in most of the cases sufficient accuracy is achieved at the second run.

III. CHOICES OF MESHLESS METHODS

Meshless methods are classified as *weighted residual methods*. Therefore, by changing the form of residual statement and/or kind of weighting function, different meshless methods can be generated [23]. Two equivalent *global* weak statements of (2), neglecting imposition of boundary conditions, are:

$$\begin{cases} \displaystyle\int_\Gamma w u_{,n} d\Gamma - \int_\Omega \nabla w \cdot \nabla u d\Omega + k^2 \int_\Omega w u d\Omega = 0 \\ \displaystyle\int_\Gamma \left(w u_{,n} - u w_{,n}\right) d\Gamma + \int_\Omega \left(\nabla^2 + k^2\right) w u d\Omega = 0 \end{cases}, \tag{6}$$

where w is the weighting function and $_{,n} = \partial/\partial n$. Based on these forms, three meshless methods can be developed:

A. MLPG5

This method is based on the first form of (6) with the Heaviside step function as weighting and leads to:

$$\int_\Gamma u_{,n} d\Gamma + k^2 \int_\Omega u d\Omega = 0. \tag{7}$$

Although this choice of weighting function is the simplest one, an extensive study in [23] showed its better performance in comparison with more complicated weights such as MLS shape functions, in the sense of convergence. In this work, hereafter, by MLPG we mean MLPG5.

B. LBIE

This method is based on the second form of (6) with the Green's function of the PDE as weighting, leading to:

$$\begin{cases} \displaystyle\int_\Gamma \left(w u_{,n} - u w_{,n}\right) d\Gamma + u(\mathbf{x}) = 0 \\ w(x, y) = \dfrac{j}{4} H_0^{(2)}\left(k\sqrt{x^2 + y^2}\right) \end{cases}. \tag{8}$$

The LBIE method makes it possible to impose the essential boundary conditions by the weak statement of the problem, which is an important capability. Thus, all of the Dirichlet, Neumann and Robin boundary conditions could be directly imposed by this method.

C. MLBE

This one is our developed method and similar to the LBIE is based on the second form of (6) but with a *proper homogeneous solution* of the differential equation as weighting and leads to:

$$\begin{cases}\int_{\Gamma}\left(wu_{,n}-uw_{,n}\right)d\Gamma=0\\ w(x,y)=\sin\left[k\left(x+y\right)/\sqrt{2}+\pi/4\right]\end{cases}. \qquad (9)$$

In this method, w should be selected such that imposition of boundary conditions becomes possible. Clearly, MLBE preserves the valuable properties of the LBIE while removing singular integrands. Further details of the MLBE method are reported in [20].

It is worth mentioning that all of these three meshless methods have a similar benefit over the others in the sense that, they reduce the computational complexity by transforming domain integrals to boundary integrals. For the problem at hand, this happens completely for the LBIE and MLBE cases, although in the case of MLPG one domain integral remains. On the other hand, LBIE requires singular integration arising from the presence of the Green's function which is in contrast to MLPG and MLBE. Thus, we can expect the MLBE to be the fastest.

IV. MESHLESS DISCRETIZATION AND SOLUTION

Only MLPG method is considered in this section. Generalization to other methods is straightforward. Meshless discretization can be considered as a four stage process.

First, the domain and boundary of the problem is represented by a sufficient number of nodes, e.g., N nodes. A sample 2D domain with its nodal description is depicted in Fig. 1.

Second, the global weak statement of the problem is applied to *local sub-domains*. In the case of (2), this leads to:

$$\int_{L_{si}}u_{,n}d\Gamma+k^{2}\int_{\Omega_{si}}ud\Omega=-\int_{\Gamma_{si}}\bar{q}d\Gamma. \qquad (10)$$

Third, the unknown field variable, i.e. u, is expanded over a set of meshless shape functions with unknown coefficients. Let $\left\{\varphi_i\right\}_{i=1}^{N}$ be the aforementioned set. Therefore:

$$u^{h}\left(\mathbf{x}\right)=\mathbf{\Phi}^{T}\left(\mathbf{x}\right)\cdot\hat{\mathbf{u}}=\sum_{i=1}^{N}\varphi_{i}\left(\mathbf{x}\right)\widehat{u_{i}}, \qquad (11)$$

in which $\hat{\mathbf{u}}=\left[\widehat{u_1}\ \ldots\ \widehat{u_N}\right]^{T}$ and u^{h} is the approximated/interpolated value of u.

Fourth, in the local weak statement of the problem, i.e. (10), u is replaced by its equivalent expansion, i.e. (11). This completes the meshless discretization. The immediate result of the last step is formation of the following system of equations:

$$\mathbf{K}\hat{\mathbf{u}}=\mathbf{f}, \qquad (12)$$

where $\hat{\mathbf{u}}$ is unknown, and entries of $\mathbf{K}$ and $\mathbf{f}$ are given by:

$$\begin{cases}K_{ij}=\int_{L_{si}}\varphi_{j,n}d\Gamma+k^{2}\int_{\Omega_{si}}\varphi_{j}d\Omega\\ f_{i}=-\int_{\Gamma_{si}}\bar{q}d\Gamma\end{cases}. \qquad (13)$$

Once $\hat{\mathbf{u}}$ is computed, the unknown function u and thus, E_z can be approximated/interpolated at any point in the problem domain and on its boundary.

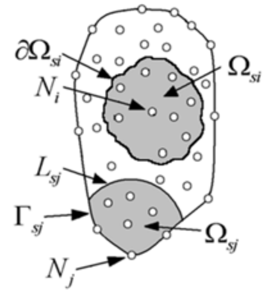

Fig. 1. Nodal geometry description of a sample 2D problem and definitions: N_i: ith node at $\mathbf{x}_i$, Ω_{si}: ith local domain, $\partial\Omega_{si}$: ith local boundary, L_{sj}: non-intersecting part of $\partial\Omega_{sj}$, Γ_{sj}: intersecting part of $\partial\Omega_{sj}$, $\partial\Omega_{sj}=L_{sj}\cup\Gamma_{sj}$.

V. NUMERICAL RESULTS

In this section, the selected meshless methods are applied to the selected microstrip antennas. The single-element antennas are depicted in Fig. 2. The two-element array antenna is constructed from the two coax-fed antennas that are 4 cm apart. In all cases $\varepsilon_r = 2.62$, $h = 1.6$ mm, *loss tangent* = 10^{-3} and $\sigma = 5.8\times10^7$ (S/m).

Thin-plate spline (TPS) functions of 9th order are used for construction of meshless shape functions [1]. Local sub-domains are rectangles with side length of d. For all uniform node distributions, $d = 1.0d_r$, where d_r is the radial nodal distance. For non-uniform and random cases, $d = 1.2d_r$, where d_r is computed based on uniform node arrangement.

For error estimate we used the relative error defined as:

$$r_e\left(u_m, u_{m+1}\right) = \left\|u_m - u_{m+1}\right\| / \left\|u_m\right\|, \tag{14}$$

where u_m is the field variable of the mth pass and $\|u\| = \left(\int_\Omega |u|^2\, d\Omega\right)^{1/2}$.

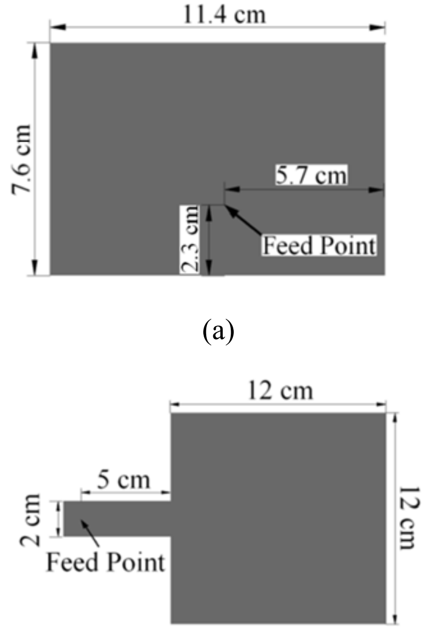

(a)

(b)

Fig. 2. Geometrical description of (a) coax-fed antenna, (b) line-fed antenna.

For the coax-fed antenna, the problem has an analytical modal solution which is regarded as the exact solution [24]. In this case, convergence curves, CPU time and condition numbers of the coefficient matrices for different methods versus number of unknowns are depicted in Fig. 3, based on uniform node arrangements.

This problem is also solved by random node arrangement via the MLBE method. The nodal description and the corresponding electric field distribution on the patch, reconstructed at 5400 nodes, are represented in Figs. 4(a) and 4(b), respectively. The computed S-parameters based on uniform and random node arrangements are reported in Fig. 4(c).

The input impedance and the corresponding S-parameters are shown in Fig. 5 and Fig. 6 for coax-fed and line-fed antennas, respectively, all based on uniform node arrangements. The line-fed case is also simulated by non-uniform node arrangement via the MLBE method. The nodal description and the corresponding electric field distribution, reconstructed at 7440 nodes, are shown in Figs. 7(a) and 7(b), respectively. In addition, the computed S-parameters based on uniform and non-uniform node arrangements are depicted in Fig. 7(c). It is worth mentioning that by this irregularity, the number of nodes is reduced from 374 to 214, without a considerable effect on S_{11}.

Finally, the S-parameters of the two-element array antenna are reported in Fig. 8. All simulations are performed on an Intel(R) Core(TM)2 CPU with 4 GB RAM.

VI. CONCLUSION

In this paper, MLPG, meshless LBIE and MLBE methods are compared by applying to thin microstrip antennas. The results are validated by the exact solution for the coax-fed antenna and the MoM for line-fed and a two-element array. It is observed that all the meshless methods have essentially the same convergence rate, with LBIE possessing the least condition number and MLBE the least CPU time.

ACKNOWLEDGMENT

The authors appreciate Prof. M. Dehghan for inputs in meshfree methods and encouragements.

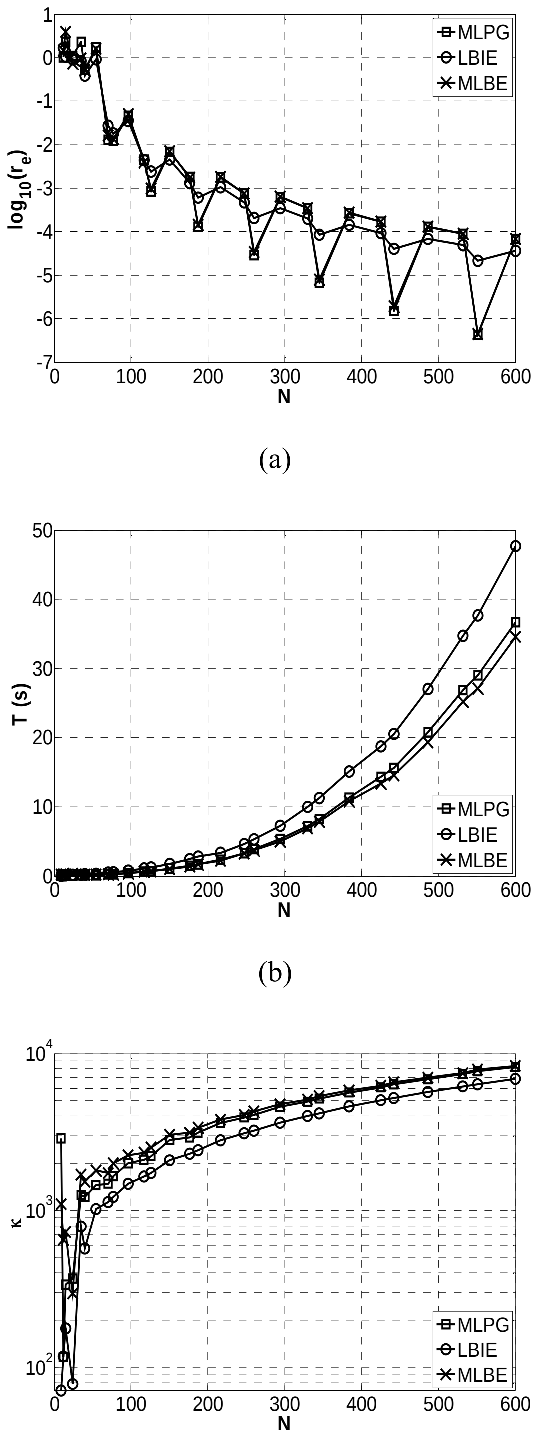

(a)

(b)

(c)

Fig. 3. Coax-fed antenna: (a) convergence curves, (b) computational complexity, (c) condition numbers.

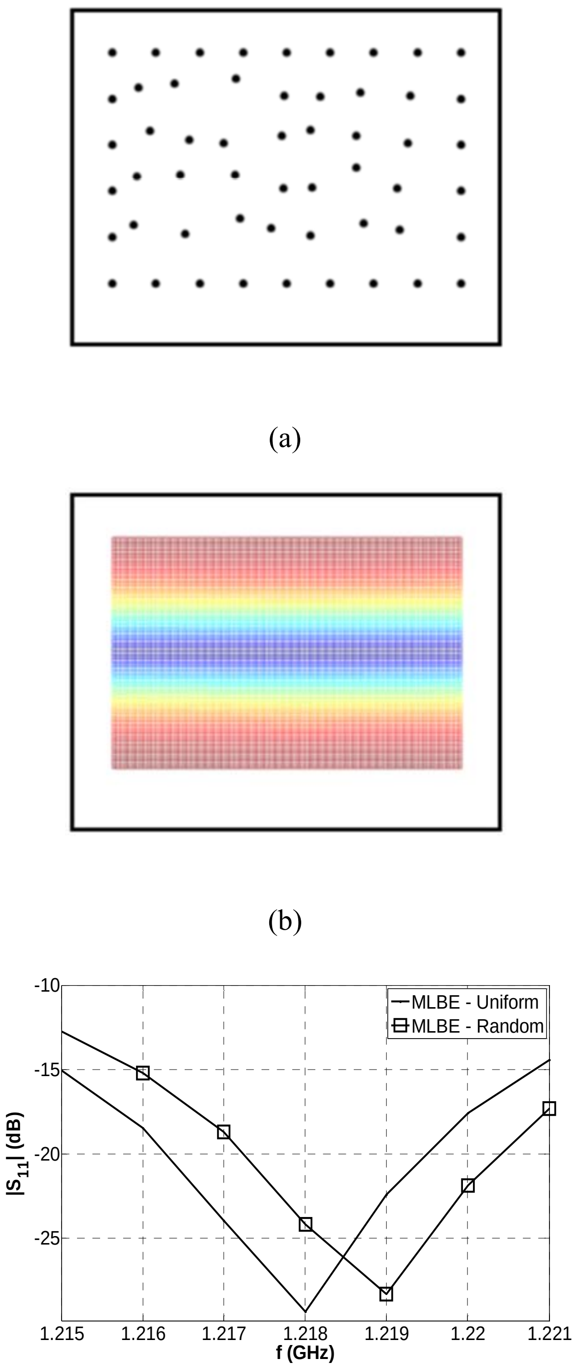

(a)

(b)

(c)

Fig. 4. Analysis of the coax-fed antenna based on random node distribution by the MLBE method: (a) node arrangement, (b) electric filed on the patch, (c) $|S_{11}|$.

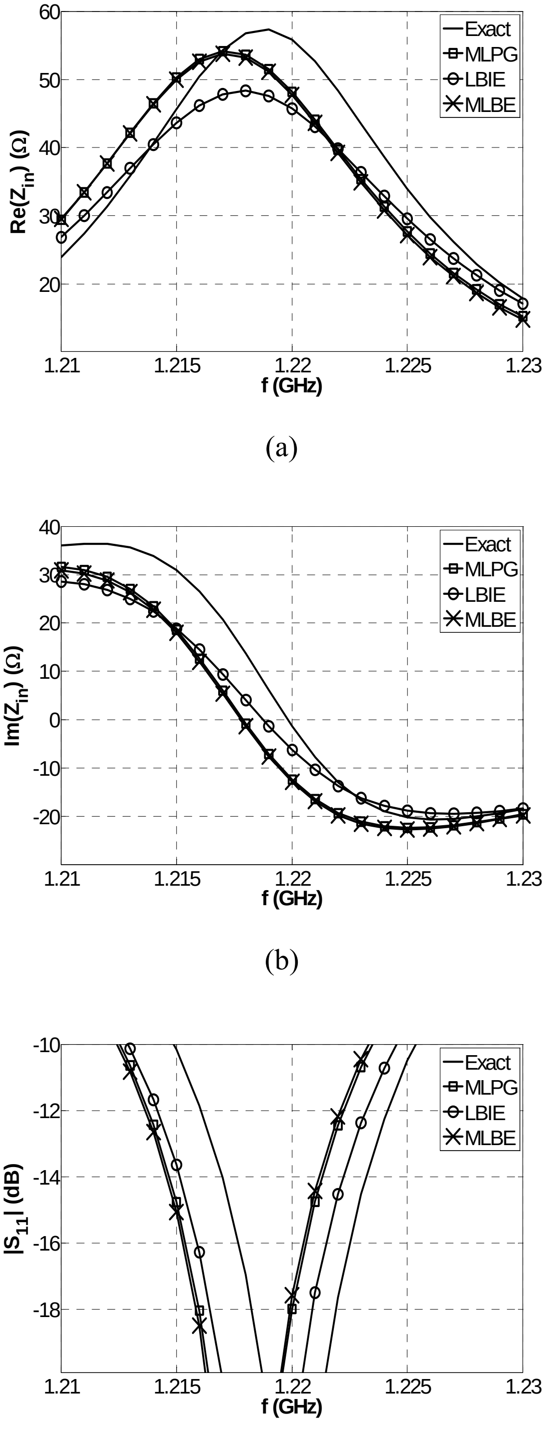

(a)

(b)

(c)

Fig. 5. Coax-fed antenna: (a) real part of input impedance, (b) imaginary part of input impedance (c) $|S_{11}|$.

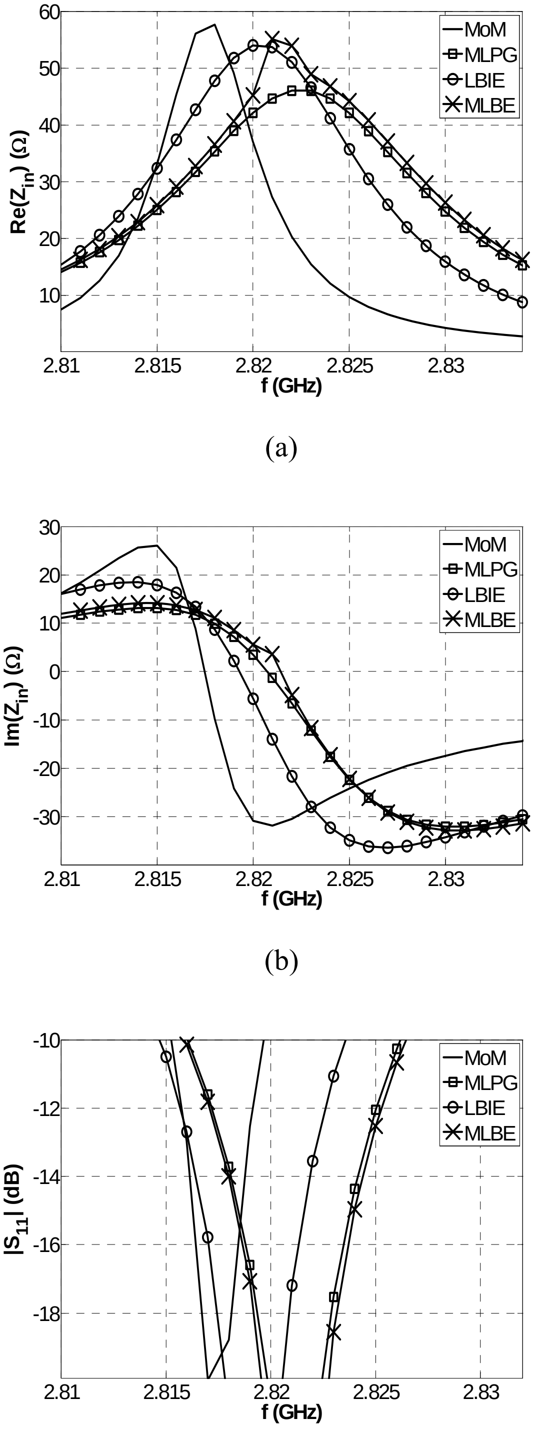

(a)

(b)

(c)

Fig. 6. Line-fed antenna: (a) real part of input impedance, (b) imaginary part of input impedance (c) $|S_{11}|$.

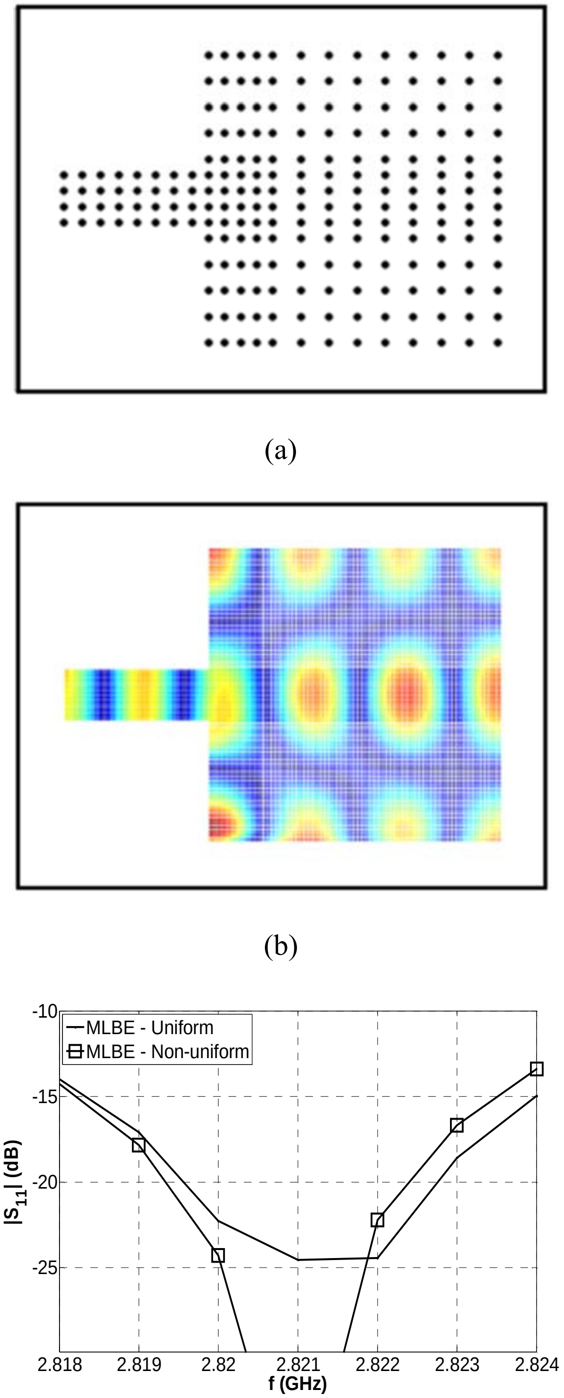

(a)

(b)

(c)

Fig. 7. Analysis of the line-fed antenna based on non-uniform node distribution by the MLBE method: (a) node arrangement, (b) electric filed on the patch, (c) $|S_{11}|$.

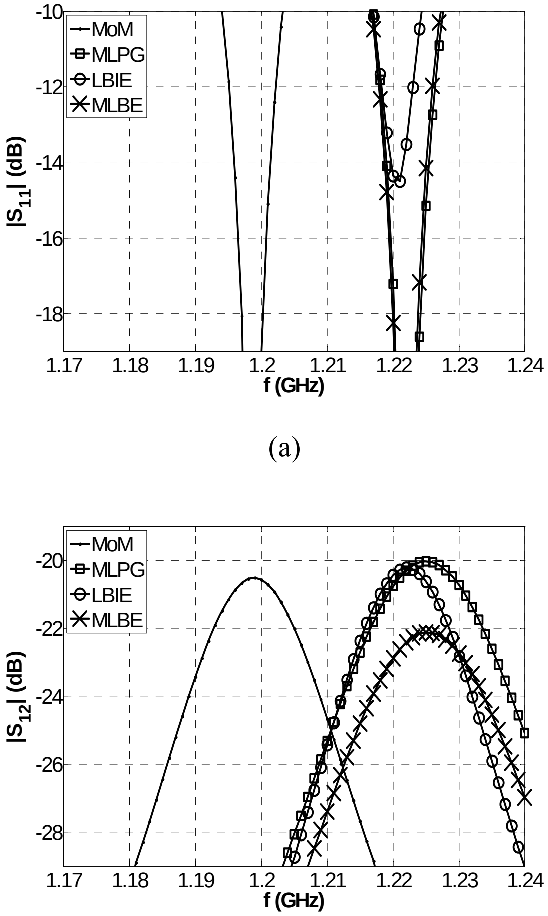

(a)

(b)

Fig. 6. Two-element array antenna: (a) $|S_{11}|$, (b) $|S_{12}|$.

REFERENCES

[1] G. R. Liu, *Mesh Free Methods*. CRC Press, 2003.

[2] Y. Marechal, "Some Meshless Methods for Electromagnetic Field Computations," *IEEE Trans. Magn.*, vol. 34, no. 5, pp. 3351-3354, 1998.

[3] C. Herault and Y. Marechal, "Boundary and Interface Conditions in Meshless Methods," *IEEE Trans. Magn.*, vol. 35, no. 3, pp. 1450-1453, 1999.

[4] S. L. Ho, S. Yang, J. M. Machado, and H. C. Wong, "Application of a Meshless Method in Electromagnetics," *IEEE Trans. Magn.*, vol. 37, no. 5, pp. 3198-3201, 2001.

[5] S. L. Ho, S. Shiyou Yang, H. C. Wong, and G. Ni, "Meshless Collocation Method Based on Radial Basis Functions and Wavelets," *IEEE Trans. Magn.*, vol. 40, no. 2, pp. 1021-1024, 2004.

[6] S. L. Ho, S. Shiyou Yang, G. Ni , H. C. Wong, and Y. Wang, "Numerical Analysis of Thin Skin Depths of 3-D Eddy-current Problems using a

Combination of Finite Element and Meshless Methods," *IEEE Trans. Magn.*, vol. 40, no. 2, pp. 1354-1357, 2004.

[7] Y. Zhang, K. R. Shao, D. X. Xie, and J. D. Lavers, "Meshless Method Based on Orthogonal Basis for Electromagnetics," *IEEE Trans. Magn.*, vol. 41, no. 5, pp. 1432-1435, 2005.

[8] Q. Li and K. Lee, "Adaptive Meshless Method for Magnetic Field Computation," *IEEE Trans. Magn.*, vol. 42, no. 8, pp. 1996-2003, 2006.

[9] F. G. Guimaraes, R. R. Saldanha, R. C. Mesquita, D. A. Lowther, and J. A. Ramirez, "A Meshless Method for Electromagnetic Field Computation Based on the Multiquadratic Technique," *IEEE Trans. Magn.*, vol. 43, no. 4, pp. 1281-1284, 2007.

[10] S. Ikuno, K. Takakura, and A. Kamitani, "Influence of Method for Imposing Essential Boundary Condition on Meshless Galerkin/Petrov-Galerkin Approaches," *IEEE Trans. Magn.*, vol. 43, no. 4, pp. 1501-1504, 2007.

[11] Y. Yu and Z. Chen, "Towards the Development of an Unconditionally Stable Time-domain Meshless Method," *IEEE Trans. Microwave Theory Tech.*, vol. 58, no. 3, pp. 578- 586, 2010.

[12] Y. Yu and Z. Chen, "A 3-D Radial Point Interpolation Method for Meshless Time-domain Modeling," *IEEE Trans. Microwave Theory Tech.*, vol. 57, no. 8, pp. 2015-202, 2009.

[13] 0T. Kaufmann, C. Fumeaux, and R. Vahldieck, "The Meshless Radial Point Interpolation Method for Time-domain Electromagnetics," *IEEE MTT-S Int. Microwave Symp. Dig.*, Atlanta, pp. 61-64, 2008.

[14] T. Kaufmann, C. Engström, C. Fumeaux, and R. Vahldieck, "Eigenvalue Analysis and Longtime Stability of Resonant Structures for the Meshless Radial Point Interpolation Method in Time Domain", *IEEE Trans. Microwave Theory Tech.*, vol. 58, no. 12, pp. 3399 - 3408, 2010.

[15] A. R. Fonseca, B. C. Correa, E. J. Silva, and R. C. Mesquita, "Improving the Mixed Formulation for Meshless Local Petrov-Galerkin Method", *IEEE Trans. Magn.*, vol. 46, no. 8, pp. 2907-2910, 2010.

[16] K. Lee, Q. Li, and H. Sun , "Effects of Numerical Formulation on Magnetic Field Computation using Meshless Methods", *IEEE Trans. Magn.*, vol. 42, no. 9, pp. 2164-2171, Sept. 2006.

[17] S. A. Viana, D. Rodger, and H. C. Lai, "Meshless Local Petrov-Galerkin Method with Radial Basis Functions Applied to Electromagnetics" , *IEE Proc.-Sci. Meas. Technol.* , vol. 151, no. 6, pp. 449- 451, 2004.

[18] S. N. Atluri and T. A. Zhu, "A New Meshless Local Petrov-Galerkin (MLPG) Approach in Computational Mechanics," *CMES*, vol. 22, pp. 117-127, 1998.

[19] T. Zhu, J.-D. Zhang, and S. N. Atluri, "A Local Boundary Integral Equation (LBIE) Method in Computational Mechanics, and a Meshless Discretization Approach," *CMES*, vol. 3, no.1, pp. 223-235, 1998.

[20] B. Honarbakhsh and A. Tavakoli, "The Meshless Local Boundary Equation Method*," Applied Computational Electromagnetics Society (ACES) Journal*, vol. 27, no. 7, pp. 550- 560, 2012.

[21] R. Sorrentino, "Planar Circuits, Waveguide Models, and Segmentation Method," *IEEE Trans. Microwave Theory Tech.*, vol. 33, no. 10, pp. 1057-1066, 1985.

[22] D. Thouroude, M. Himdi, and J. P. Daniel, "CAD-Oriented Cavity Model for Rectangular Patches," *IEE Elect. Lett.*, vol. 26, no. 13, pp. 842-844, 1990.

[23] S. N. Atluri and S. Shen, "The Meshless Local Petrov-Galerkin (MLPG) Method: a Simple & Less-costly Alternative to the Finite Element and Boundary Element Methods," CMES, vol. 3, no. 1, pp. 11-51, 2002.

[24] R. E. Collin, *Antennas and Radiowave Propagation*. McGraw-Hill, 1987.

Babak Honarbakhsh was born in Tehran, Iran. He received his B.S. and M.S. degrees in electrical engineering from Amirkabir University of Technology where he is currently working toward his Ph.D. degree. His current research interest is numerical solution of electromagnetic problems by meshfree methods.

Ahad Tavakoli was born in Tehran, Iran, on March 8, 1959. He received the B.S. and M.S. degrees from the University of Kansas, Lawrence, and the Ph.D. degree from the University of Michigan, Ann Arbor, all in electrical engineering, in 1982, 1984, and 1991, respectively.

In 1991, he joined the Amirkabir University of Technology, Tehran, Iran, where he is currently a Professor in the Department of Electrical Engineering. His research interests include EMC, scattering of electromagnetic waves and microstrip antennas.

Single Snapshot 2D-DOA Estimation in Impulsive Noise Environment using Linear Arrays

Ying Zhang[1], **Huapeng Zhao**[2], **Qun Wan**[1]

[1]College of Electronic Engineering
University of Electronic Science and Technology of China, Chengdu, 610054, China
zh0045ng@e.ntu.edu.sg, wanqun@uestc.edu.cn

[2]Institute of High Performance Computing
1 Fusionopolis Way, 138632, Singapore
zhaoh@ihpc.a-star.edu.sg

Abstract —This paper considers single snapshot two dimensional direction-of-arrival (2D-DOA) estimation in impulsive noise environment employing linear arrays. 2D-DOA estimation is realized in two steps. Firstly, the 2D-DOA estimation problem is decomposed into two independent one dimensional direction-of-arrival (1D-DOA) estimation problems. The 1D-DOA estimation is derived using the support vector regression based basis selection algorithm. Secondly, an over-complete dictionary is designed based on amplitude information of sources, and angle pairing is accomplished in perspective of basis selection. Validity and advantages of the proposed algorithm are shown through computer simulations.

Index Terms **—** 2D-DOA, basis selection, linear array, single snapshot, support vector regression.

I. INTRODUCTION

Direction-of-arrival estimation is to find the directions of sources impinging on antenna arrays [1]-[5]. Recently, a 1D-DOA estimation algorithm was proposed based on the sparse signal reconstruction [6], which renders several advantages over existing methods, including increased resolution, improved robustness against limited number of snapshots, and the capability to handle correlated sources.

Two-dimensional direction-of-arrival (2D-DOA) estimation is usually nontrivial. Although angle pairing can be accomplished by searching, such a method is computationally unattractive [7]. Based on the observation that the data matrices with the same set of eigenvectors can be diagonalized by the same similarity transform, two methods were introduced to realize angle pairing [8]. Some other methods based on eigen-structure of signals were also developed [9]. Recently, a 2D-DOA estimation algorithm has been proposed based on the support vector machine [10], whose performance is influenced by the training scenarios. When a limited number of snapshots are available, performance of the aforementioned algorithms will deteriorate. Thus, it is desirable to develop 2D-DOA estimation methods using a single snapshot. [11] and [12] presented two single snapshot 2D-DOA estimation methods, where nonuniformly spaced planar arrays were used. In [13], a uniform rectangular array is employed to realize single snapshot 2D-DOA estimation. All these algorithms are based on eigen-decomposition. Escot et.al. [14] proposed to accomplish 2D-DOA estimation by particle swarm optimization. However, it is known that evolutionary algorithms are unable to yield consistent solutions and usually suffer from high computational load. Furthermore, it has been shown that impulsive noise appears at wireless receivers in the form of impulsive bursts [15]. In this case, all second-order statistics based algorithms are unable to perform well.

In this paper, we address the problem of single snapshot 2D-DOA estimation in impulsive noise environment employing linear arrays. The rest of this paper is organized as follows. Section II

Submitted On: Nov. 20, 2011
Accepted On: Nov. 23, 2012

briefly reviews 1D-DOA estimation in perspective of basis selection. Section III describes the proposed method in detail, and Section IV presents simulation results to show the validity and advantages of the proposed method. Section V concludes the work described in this paper.

II. REVIEW OF 1D-DOA ESTIMATION IN PERSPECTIVE OF BASIS SELECTION

Generate an over-complete dictionary which consists of steering vectors from all possible directions of sources $\left\{\hat{\theta}_1,\ldots,\hat{\theta}_N\right\}$ i.e., $\overline{\mathbf{A}}=\left(\mathbf{a}(\hat{\theta}_1),\ldots,\mathbf{a}(\hat{\theta}_N)\right)$, where N denotes the number of spatial samplings. The 1D-DOA estimation problem is equivalent to solving $\bar{\mathbf{s}}$ of

$$\mathbf{x} = \overline{\mathbf{A}}\bar{\mathbf{s}} + \mathbf{n}, \tag{1}$$

where the i-th element of $\bar{\mathbf{s}}$ is nonzero if and only if a source comes from $\hat{\theta}_i$. $\mathbf{x}$ is the snapshot, and $\mathbf{n}$ denotes the noise. When the number of sensors, denoted by M, is much smaller than N, i.e., M<<N, most of entries in $\bar{\mathbf{s}}$ are zero. Solving $\bar{\mathbf{s}}$ from (1) can be formulated as a basis selection problem.

Under Gaussian noise assumption, the optimal $\bar{\mathbf{s}}$ in (1) can be found by solving the following optimization problem:

$$\min_{\bar{\mathbf{s}}} \mathrm{E}^{\mathrm{p}}(\bar{\mathbf{s}}), \tag{2a}$$

$$\text{subject to } \|\mathbf{x}-\mathbf{A}\bar{\mathbf{s}}\|_2^2 \le \varepsilon^2, \tag{2b}$$

where $\mathrm{E}^{\mathrm{p}}(\bar{\mathrm{s}})$ represents the diversity of $\bar{\mathrm{s}}$ which can be chosen according to some existing criteria [6]. There have been many algorithms to solve (2), one of which is the match pursuit [16]-[19].

III. THE PROPOSED 2D-DOA ESTIMATION ALGORITHM

A. Basis selection algorithm in impulsive noise environment

In this paper, we choose the l_p-norm as the diversity measurement [19]. In the impulsive noise environment, basis selection can be realized via solving the following problem:

$$\min_{\bar{\mathbf{s}}}\|\bar{\mathbf{s}}\|_{\mathrm{p}}^{\mathrm{p}},\ \mathrm{p}\le 1, \tag{3a}$$

$$\text{subject to } \left|\mathrm{x_i}-\mathbf{a}_\mathrm{i}^\mathrm{T}\bar{\mathbf{s}}\right| < \varepsilon, \forall i = 1,\ldots,M, \tag{3b}$$

where $\mathbf{a}_\mathrm{i}^\mathrm{T}$ denotes the i-th row of $\overline{\mathbf{A}}$, $\mathrm{x_i}$ denotes the ith element of $\mathbf{x}$, and ε represents the impulsive noise. $\|\bar{\mathbf{s}}\|_\mathrm{p}$ denotes the l_p-norm of $\bar{\mathbf{s}}$ which is computed via $\|\bar{\mathbf{s}}\|_\mathrm{p} = \left(\sum_{\mathrm{i}=1}^{\mathrm{N}}|\bar{\mathrm{s}}_\mathrm{i}|^\mathrm{p}\right)^{1/\mathrm{p}}$.

Since direct solution of (3) is difficult, the affine scaling transformation [19] is applied to transform (3) into an equivalent problem

$$\min_{\mathbf{q}}\|\mathbf{q}\|_2^2, \tag{4a}$$

$$\text{subject to } \left|\mathrm{x_i}-\mathbf{b}_\mathrm{i}^\mathrm{T}\mathbf{q}\right| < \varepsilon, \forall i = 1,\ldots,M, \tag{4b}$$

where $\mathbf{q}=\mathbf{W}^{-1}\bar{\mathbf{s}}$, $\mathbf{B}=\mathbf{AW}$, and $\mathbf{W}=\mathrm{diag}\left\{|\bar{\mathrm{s}}_\mathrm{i}|^{1-\mathrm{p}/2}\right\}$. $\mathbf{b}_\mathrm{i}^\mathrm{T}$ denotes the i-th row of $\mathbf{B}$.

Considering $\mathrm{x_i}$ as the target for the input pattern $\mathbf{b}_\mathrm{i}^\mathrm{T}$, (4) is identical to the optimization problem of SVR [20] formulated as

$$\min_{\mathbf{q},\boldsymbol{\epsilon},\boldsymbol{\epsilon}^*}\|\mathbf{q}\|_2^2 + \mathrm{C}\sum_{\mathrm{i}=1}^{\mathrm{M}}(\epsilon_\mathrm{i}+\epsilon_\mathrm{i}^*), \tag{5a}$$

$$\text{subject to } \begin{array}{c} \mathrm{x_i}-\mathbf{b}_\mathrm{i}^\mathrm{T}\mathbf{q} \le \varepsilon+\epsilon_\mathrm{i} \\ \mathbf{b}_\mathrm{i}^\mathrm{T}\mathbf{q}-\mathrm{x_i} \le \varepsilon+\epsilon_\mathrm{i}^*, \\ \epsilon_\mathrm{i},\epsilon_\mathrm{i}^* \ge 0 \end{array} \tag{5b}$$

where $\epsilon_\mathrm{i},\epsilon_\mathrm{i}^*$ are slack variables, and C>0 determines the trade-off between finding a sparse solution and retaining small residual error. The dual problem of (5) is given by

$$\min_{\boldsymbol{\alpha},\boldsymbol{\alpha}^*} -\sum_{\mathrm{i}=1}^{\mathrm{M}}\sum_{\mathrm{j}=1}^{\mathrm{M}}(\alpha_\mathrm{i}-\alpha_\mathrm{i}^*)(\alpha_\mathrm{j}-\alpha_\mathrm{j}^*)\langle \mathrm{b_i},\mathrm{b_j}\rangle -\varepsilon\sum_{\mathrm{i}=1}^{\mathrm{M}}(\alpha_\mathrm{i}+\alpha_\mathrm{i}^*) + \sum_{\mathrm{i}=1}^{\mathrm{M}}\mathrm{x_i}(\alpha_\mathrm{i}-\alpha_\mathrm{i}^*), \tag{6a}$$

$$\text{subject to } \sum_{\mathrm{i}=1}^{\mathrm{M}}(\alpha_\mathrm{i}-\alpha_\mathrm{i}^*) = 0, \alpha_\mathrm{i},\alpha_\mathrm{i}^* \in [0,\mathrm{C}], \tag{6b}$$

and $\mathbf{q}$ is given by

$$\mathbf{q} = \sum_{\mathrm{i}=1}^{\mathrm{M}}(\alpha_\mathrm{i}-\alpha_\mathrm{i}^*)\,\mathbf{b}_\mathrm{i}, \tag{7}$$

which is called support vector expansion. By solving (6), $\mathbf{q}$ can be obtained, and $\bar{\mathbf{s}}$ can be calculated using $\bar{\mathbf{s}}=\mathbf{Wq}$.

For our problem, the input pattern $\mathbf{b}_\mathrm{i}$ is unknown, we thereby propose the following iterative algorithm to solve (3):

Step 1: Initialize $\bar{\mathbf{s}}(0)$using a randomly generated vector, k=0, $\mathbf{W}(0)=\mathrm{diag}\left\{|\bar{\mathrm{s}}_\mathrm{i}(0)|^{1-\mathrm{p}/2}\right\}$, and $\mathbf{B}(0) = \mathbf{AW}(0)$.

Step 2: Solve (4) using SVR and obtain $\mathbf{q}(k)$.

Step 3: $k = k+1$, $\bar{\mathbf{s}}(k)=\mathbf{W}(k-1)\mathbf{q}(k-1)$, $\mathbf{W}(k)=\mathrm{diag}\left\{|\bar{\mathrm{s}}_\mathrm{i}(k)|^{1-\mathrm{p}/2}\right\}$, $\mathbf{B}(k) = \mathbf{AW}(k)$.

Step 4: If $\|\bar{\mathbf{s}}(k+1)-\bar{\mathbf{s}}(k)\|_2/\|\bar{\mathbf{s}}(k+1)\|_2 < \tau$, stop. Otherwise, go to *Step 2*.

In the aforementioned iterative algorithm, k is the number of iteration steps, and τ is the convergence criterion, which is chosen to be 0.01 in this paper.

B. Angle pairing using basis selection

1) Over-complete dictionary with respect to directions of sources: In this paper, three unparallel arrays A, B, and C are used. The unit direction vectors of the arrays are assumed to be $(1,0,0)$, $(\cos\theta_B, \sin\theta_B, 0)$, and $(\cos\theta_C\cos\varphi_C, \sin\theta_C\cos\varphi_c, \sin\varphi_C)$. Suppose that a narrow band source with azimuth angle θ and elevation angle φ impinges array A, B and C with 1D-DOA ϑ_a, ϑ_b and ϑ_c , respectively. The following equations can be derived:

$$\cos\vartheta_a = \cos\theta\cos\varphi, \tag{8a}$$

$$\cos\vartheta_b = \cos\theta\cos\varphi\cos\theta_B + \sin\theta\cos\varphi\sin\theta_B, \tag{8b}$$

$$\cos\vartheta_c = \cos\theta\cos\varphi\cos\theta_C\cos\varphi_C + \sin\theta\cos\varphi\sin\theta_C\cos\varphi_C + \sin\varphi\sin\varphi_C. \tag{8c}$$

From (8), we may express $\cos\vartheta_c$ in terms of $\cos\vartheta_a$ and $\cos\vartheta_b$ as

$$\cos\vartheta_c = f(\vartheta_a, \vartheta_b) = \cos\vartheta_a\cos\varphi_C\sin(\theta_B - \theta_C)/\sin\theta_B + \cos\vartheta_b \cos\varphi_C\sin\theta_C/\sin\theta_B + \sqrt{1-(1+D)\cos^2\vartheta_a}\sin\varphi_C, \tag{9}$$

where $D = \left(\frac{\cos\vartheta_b}{\cos\vartheta_a} - \cos\theta_B\right)^2 / \sin^2\theta_B$. Therefore, the steering vector of array C can be expressed in terms of ϑ_a and ϑ_b as

$$\mathbf{a}(\vartheta_c) = \left(e^{j2\pi d_1^c\cos\vartheta_c/\lambda}, \dots, e^{j2\pi d_M^c\cos\vartheta_c/\lambda}\right)^T = \left(e^{j2\pi d_1^c f(\vartheta_a,\vartheta_b)/\lambda}, \dots, e^{j2\pi d_M^c f(\vartheta_a,\vartheta_b)/\lambda}\right)^T, \tag{10}$$

where d_i^c denotes the distance between the origin and the *i*-th sensor of array C.

Denote the estimated two 1D-DOA with respect to array A and B as $\widehat{\boldsymbol{\vartheta}_a} = \left(\hat\vartheta_a^1, \dots, \hat\vartheta_a^{M_a}\right)$ and $\widehat{\boldsymbol{\vartheta}_b} = \left(\hat\vartheta_b^1, \dots, \hat\vartheta_b^{M_b}\right)$, where M_a and M_b are the number of 1D-DOA estimated with respect to array A and B, respectively. It is possible that some sources have identical 1D-DOA, thereby $M_a, M_b \le M$ holds. The equality holds only when $\hat\vartheta_a^i \ne \hat\vartheta_a^j$, $\hat\vartheta_b^i \ne \hat\vartheta_b^j$ are tenable for all $i \ne j$. Using (9) and (10), we may generate an over-complete dictionary with respect to array C in terms of ϑ_a and ϑ_b as

$$\bar{\mathbf{A}}(\vartheta_c) = \bar{\mathbf{A}}(f(\vartheta_a, \vartheta_b)) = [\bar{\mathbf{A}}_\Delta\left(\vartheta_a^1, \vartheta_b^1\right), \dots, \bar{\mathbf{A}}_\Delta\left(\vartheta_a^1, \vartheta_b^{M_b}\right), \bar{\mathbf{A}}_\Delta\left(\vartheta_a^2, \vartheta_b^1\right), \dots, \bar{\mathbf{A}}_\Delta\left(\vartheta_a^2, \vartheta_b^{M_b}\right), \dots, \bar{\mathbf{A}}_\Delta\left(\vartheta_a^{M_a}, \vartheta_b^1\right), \dots, \bar{\mathbf{A}}_\Delta\left(\vartheta_a^{M_a}, \vartheta_b^{M_b}\right)], \tag{11}$$

where $\bar{\mathbf{A}}_\Delta\left(\vartheta_a^i, \vartheta_b^j\right)$ consists of steering vectors with respect to the neighboring region of $\left(\vartheta_a^i, \vartheta_b^j\right)$, i.e.,

$$\bar{\mathbf{A}}_\Delta\left(\vartheta_a^i, \vartheta_b^j\right) = [\mathbf{a}(\vartheta_a^i - \Delta_a, \vartheta_b^j - \Delta_b), \mathbf{a}(\vartheta_a^i - \Delta_a + \delta_a, \vartheta_b^j - \Delta_b + \delta_b), \mathbf{a}(\vartheta_a^i - \Delta_a + 2\delta_a, \vartheta_b^j - \Delta_b + 2\delta_b), \dots, \mathbf{a}(\vartheta_a^i + \Delta_a, \vartheta_b^j + \Delta_b)]. \tag{12}$$

In (12), Δ_a and Δ_b denote the neighboring region of ϑ_a^i and ϑ_b^j, respectively. δ_a and δ_b denote the sampling interval of ϑ_a^i and ϑ_b^j, respectively. By introducing neighboring region, potential error in the 1D-DOA estimation can be amended so that accurate 2D-DOA estimation can be achieved.

2) Over-complete dictionary with respect to amplitudes of sources: The over-complete dictionary $\bar{\mathbf{A}}(\vartheta_c)$ given by (12) contains all the possible angle pairings. The columns of $\bar{\mathbf{A}}(\vartheta_c)$ which match the snapshot of array C (denoted by $\mathbf{x}_c$) gives the correct angle pairing result. Therefore, the angle pairing problem can be formulated as the following inverse problem which aims to compute $\bar{\mathbf{s}}_c$:

$$\mathbf{x}_c = \bar{\mathbf{A}}\bar{\mathbf{s}}_c + \mathbf{n}_c, \tag{13}$$

where $\mathbf{n}_c$ denotes the additive noise on array C. However, solving (13) directly with basis selection cannot guarantee correct angle pairing result. It is noted that if there were two angle pairs satisfying $f\left(\vartheta_a^i, \vartheta_b^j\right) = f\left(\vartheta_a^k, \vartheta_b^l\right)$, $i \ne k, j \ne l$, incorrect angle pairing occurs. In order to avoid such a problem, additional constraint should be imposed on $\bar{\mathbf{s}}_c$ when solving (13).

It is observed that incorrect angle pairing probably results in significant difference between signal amplitudes estimated from (13) and those from the 1D-DOA estimation step. Thus, constraint can be imposed on the signal amplitude to guarantee correct angle pairing result.

Suppose that the estimated amplitudes of sources from 1D-DOA estimation are $\widehat{\mathbf{s}_a} = \left(\hat s_a^1, \dots, \hat s_a^{M_a}\right)$ and $\widehat{\mathbf{s}_b} = \left(\hat s_b^1, \dots, \hat s_b^{M_b}\right)$. It is assumed that $\widehat{\mathbf{s}_a}$ and $\widehat{\mathbf{s}_b}$ should not change significantly with respect to the three arrays. The following constraints can be imposed on $\bar{\mathbf{s}}_c$:

$$\|\mathbf{B}_a\bar{\mathbf{s}}_c - \widehat{\mathbf{s}_a}\|_2^2 \le \varepsilon_a^2, \tag{14a}$$

$$\|\mathbf{B}_b\bar{\mathbf{s}}_c - \widehat{\mathbf{s}_b}\|_2^2 \le \varepsilon_b^2, \tag{14b}$$

where the elements of $\mathbf{B}_a$ and $\mathbf{B}_b$ are given by

$$b_a(i,j) = \begin{cases} 1, \text{if } \bar{\mathbf{A}}_j(\vartheta_c) \in \bar{\mathbf{A}}_\Delta\left(\vartheta_a^i, \vartheta_b^1\right), \dots, \bar{\mathbf{A}}_\Delta\left(\vartheta_a^i, \vartheta_b^{M_b}\right) \\ 0, \text{otherwise} \end{cases},$$

$$\mathrm{b_b}(\mathrm{i},\mathrm{j}) = \begin{cases} 1, \text{if } \bar{\mathbf{A}}_{\mathrm{j}}(\vartheta_{\mathrm{c}}) \in \bar{\mathbf{A}}_{\Delta}(\vartheta_{\mathrm{a}}^{1}, \vartheta_{\mathrm{b}}^{\mathrm{i}}), \dots, \bar{\mathbf{A}}_{\Delta}(\vartheta_{\mathrm{a}}^{\mathrm{M_a}}, \vartheta_{\mathrm{b}}^{\mathrm{i}}) \\ 0, \text{otherwise} \end{cases}.$$

$\bar{\mathbf{A}}_{\mathrm{j}}(\vartheta_{\mathrm{c}})$ denotes the j-th column of $\bar{\mathbf{A}}(\vartheta_{\mathrm{c}})$. With (14), angle pairing can be realized by finding a sparse solution $\bar{\mathbf{s}}_{\mathrm{c}}$ from

$$\tilde{\mathbf{x}}_{\mathrm{c}} = \tilde{\mathbf{A}}\bar{\mathbf{s}}_{\mathrm{c}} + \tilde{\mathbf{n}}_{\mathrm{c}}, \qquad (15)$$

where $\tilde{\mathbf{A}} = [\bar{\mathbf{A}}(\vartheta_{\mathrm{c}}) \quad \mathbf{B}_{\mathrm{a}} \quad \mathbf{B}_{\mathrm{b}}]^{\mathrm{T}}$ and $\tilde{\mathbf{x}}_{\mathrm{c}} = [\mathbf{x}_{\mathrm{c}} \quad \widehat{\boldsymbol{s}_{\mathrm{a}}} \quad \widehat{\mathbf{s}_{\mathrm{b}}}]^{\mathrm{T}}$.

C. Discussions on the proposed single snapshot 2D-DOA algorithm

Conventional application of SVR requires a large number of training data to derive an accurate regression model [10], [21]. Then, the derived regression model is used for online testing. The computational complexity for training is usually large. Furthermore, if the real scenario is different from the trained ones, the performance of SVR will deteriorate. On the other hand, the proposed algorithm utilizes SVR as a solver to solve (4). Therefore, offline training and online testing are not required for the proposed algorithm.

For SVR, let l be the number of training points, N_S the number of support vectors, and d_L the dimension of the input data. The complexity of SVR is $O(N_s^3 + N_s^2 l + N_s dLl)$ when $N_s/l \ll 1$ and $O(N_s^3 + N_s l + N_s d_L l)$ when $N_s/l \approx 1$ [22]. From (4), it is observed that for the proposed algorithm, the number of input patterns is L, and the dimension of the input pattern is N. Due to the property of the over-complete dictionary, $N > L$ holds, so that the computational complexity of the proposed algorithm is approximately given by $O(N_s NL)$. In order to reduce the computational complexity of the proposed algorithm, grid refining technique can be applied so that a smaller value of N can be used. It should be mentioned that compared with applying SVR for training and testing, the proposed algorithm has much less computational load, because the number of training samples is usually much larger than N.

IV. COMPUTER SIMULATIONS

Without loss of generality, we assume that three linear arrays lie in the same plane. The element spacing of each array is equal to half-wavelength with respect to the operating frequency. The azimuth angle of array B and C are assumed to be 30° and 90°, respectively. The number of sources is assumed to be 4. The angular sampling interval to generate the overcomplete dictionary $\bar{\mathbf{A}}(\vartheta_{\mathrm{c}})$ is 1°. The parameters for implementation of SVR are chosen as $\epsilon=0.001$ and C = 0.6, which are empirical values. Impulsive noise is generated as the mixture of a Gaussian process and a Bernoulli-Gaussian process [23]. The Gaussian process is with zero mean and variance σ_1^2. The impulsive bursts are generated by a Bernoulli-Gaussian process, where a Gaussian variable with zero mean and variance σ_2^2 and a Bernoulli variable with success probability p are used. The Signal-to-Noise Ratio (SNR) is computed as $10\log_{10} 1/\left((1-\mathrm{p})\sigma_1^2 + \mathrm{p}(\sigma_1^2+\sigma_2^2)\right)$ dB. In the simulations, $\sigma_2^2 = 100\sigma_1^2$ and $p = 0.1$ are assumed.

A. Sources with different 1D-DOAs

In the first simulation, the sources are assumed to be located at $(35^{\mathrm{o}}, 47^{\mathrm{o}})$, $(47^{\mathrm{o}}, 52^{\mathrm{o}})$, $(59^{\mathrm{o}}, 56^{\mathrm{o}})$, $(66^{\mathrm{o}}, 65^{\mathrm{o}})$ with unity power. The phase of each source is randomly distributed between 0 and 2π. The number of sensors is assumed to be 10.

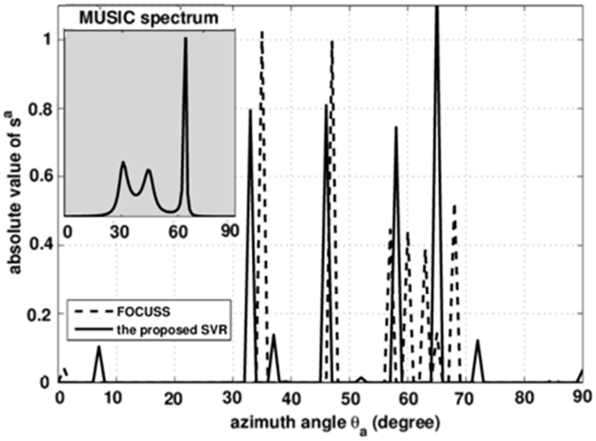

Fig. 1. The estimated spectrum for 1D-DOA estimation $\hat{\vartheta}_{\mathrm{a}}$ with SNR=20 dB and L=10.

Figures 1 and 2 show the estimated spectra for 1D-DOA estimation $\hat{\vartheta}_{\mathrm{a}}$ and $\hat{\vartheta}_{\mathrm{b}}$, respectively. It is observed from Figs. 1 and 2 that the proposed SVR based basis selection algorithm shows less spurious peaks than that of the FOCUSS algorithm. This is because the proposed SVR based algorithm is robust against the impulsive noise. Also, the MUSIC spectrum using a single snapshot [24] is plotted with the number of sensors in subarray equal to 5. It is observed that because the number of sensors is small, the single snapshot MUSIC algorithm is unable to precisely locate the four sources.

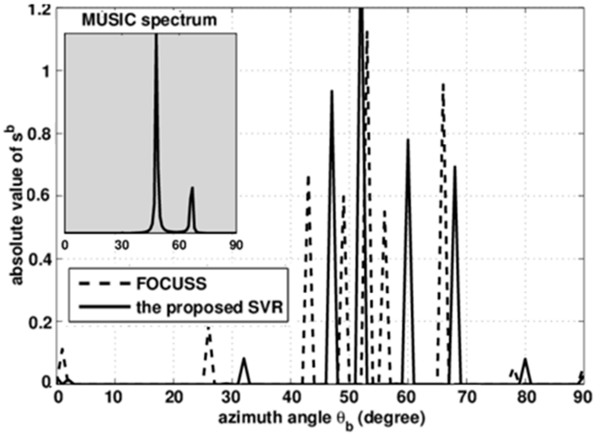

Fig. 2. The estimated spectrum for 1D-DOA estimation $\hat{\vartheta}_b$ with SNR=20 dB and L=10.

Figure 3 presents the 2D-DOA estimation results for 50 independent trials with SNR equal to 20 dB. From Fig. 3, we see that incorrect angle pairing does not occur during the 50 independent trials.

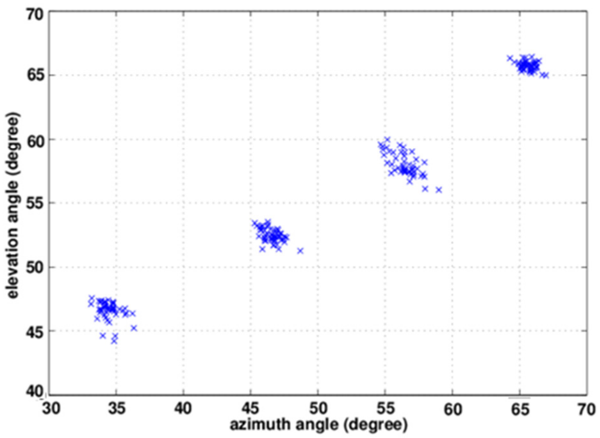

Fig. 3. 2D-DOA estimation results for 50 independent trials with SNR=20 dB and L=10.

Table 1 shows the Root-Mean-Square-Error (RMSE) of the proposed method with different SNR for 50 independent trials, and Table 2 shows the RMSE of the proposed method against the number of sensors. From Table 1 and Table 2, we see that the proposed algorithm is able to give satisfactory performance. As the value of SNR or L increases, the RMSE of estimation decreases.

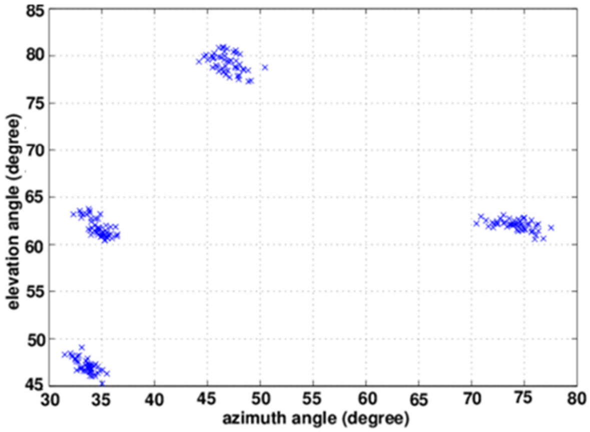

Fig. 4. 2D-DOA estimation results for 50 independent trials with SNR=20 dB and L=10.

Table 1: RMSE(degree) versus SNR for sources located at $(35^o, 47^o)$, $(47^o, 52^o)$, $(59^o, 56^o)$, $(66^o, 65^o)$.

RMSE(degree) of 2D-DOA estimations (L=10)				
SNR(dB)	$(35^o, 47^o)$	$(47^o, 52^o)$	$(59^o, 56^o)$	$(66^o, 65^o)$
10	3.9530	2.2170	2.7130	2.9181
15	2.0245	1.3396	2.0770	1.3156
20	1.4917	0.9763	1.8636	1.0039
25	0.8356	0.7345	1.2893	0.7087
30	0.6461	0.6799	1.0668	0.7038
35	0.6080	0.6406	0.7332	0.6338
40	0.5849	0.6373	0.6429	0.5703

Table 2: RMSE(degree) versus L for sources located at $(35^o, 47^o)$, $(47^o, 52^o)$, $(59^o, 56^o)$, $(66^o, 65^o)$.

RMSE(degree) of 2D-DOA estimations (SNR=20 dB)				
L	$(35^o, 47^o)$	$(47^o, 52^o)$	$(59^o, 56^o)$	$(66^o, 65^o)$
8	1.9921	1.8592	2.6749	1.8475
9	1.6292	1.3489	2.2948	1.4928
10	1.4917	0.9763	1.8636	1.0039
11	1.0192	0.8674	1.4059	0.8924
12	0.9019	0.8347	1.3873	0.7294

B. Sources with the same 1D-DOA

In this simulation, we assume that the four sources are located at $(35^o, 47^o)$, $(35^o, 62^o)$, $(50^o, 80^o)$, $(76^o, 62^o)$ with unity power. In this case, two sources have identical azimuth angle, and the other two sources have identical elevation angle.

Figure 4 shows the 2D-DOA estimation results for 50 independent trials with SNR = 20 dB and L = 10. Tables 3 and 4 show the RMSE of the proposed method with different SNR and L, respectively. When some sources have identical 1D-DOA, the number of derived 1D-DOA estimations is smaller than that of sources.

In this simulation, only three DOA are estimated in the 1D-DOA estimation step. However, using the proposed angle pairing method, the sources with the same 1D-DOA automatically split. As shown in Fig. 4, the proposed algorithm does not give incorrect angle pairing results for 50 independent trials. Tables 3 and 4 show that the performance of the proposed algorithm in this case is a little bit poorer than that in the previous simulation, but it is still satisfactory.

Table 3: RMSE (degree) versus SNR for sources located at $(35^o, 47^o)$, $(35^o, 62^o)$, $(50^o, 80^o)$, $(76^o, 62^o)$.

RMSE(degree) of 2D-DOA estimations (L=10)				
SNR(dB)	$(35^o, 47^o)$	$(35^o, 62^o)$	$(50^o, 80^o)$	$(76^o, 62^o)$
10	3.6711	2.5581	4.0508	2.6989
15	2.6146	1.9299	3.0435	2.3649
20	1.5336	1.2835	2.1237	1.9011
25	1.1902	1.0214	1.8015	1.5975
30	1.0508	0.9582	1.1362	1.1212
35	0.9112	0.9011	0.9571	0.9821
40	0.8489	0.7530	0.8960	0.9155

Table 4: RMSE (degree) versus L for sources located at $(35^o, 47^o)$, $(35^o, 62^o)$, $(50^o, 80^o)$, $(76^o, 62^o)$.

RMSE(degree) of 2D-DOA estimations (SNR=20 dB)				
L	$(35^o, 47^o)$	$(35^o, 62^o)$	$(50^o, 80^o$	$(76^o, 62^o$
8	2.5935	2.9737	2.9207	2.1537
9	2.1788	2.6361	2.3228	2.0449
10	1.5336	1.2835	2.1237	1.9011
11	1.0564	1.0190	1.8211	1.4085
12	0.9382	0.9015	1.5020	1.0349

V. CONCLUSIONS

In this paper, a new method has been described to address the problem of 2D-DOA estimation using a single snapshot in impulsive noise environment. Three unparallel linear arrays are employed. The 2D-DOA estimation problem is decomposed into two 1D-DOA estimation problems which are solved by the proposed SVR based basis selection algorithm. To realize angle pairing, an over-complete dictionary is designed using estimated amplitudes of sources. Computer simulation shows that the proposed algorithm is able to realize single snapshot 2D-DOA estimation in impulsive noise environment with satisfactory accuracy. The proposed method is especially useful for 2D-DOA estimation using a limited number of snapshots in the presence of impulsive noise. Future work is to extend the proposed method to other array structures.

ACKNOWLEDGEMENT

This work was supported by a grant from the National Natural Science Foundation for Young Scholars of China (Grant No.61101094).

REFERENCES

[1] R. O. Schmidt, “Multiple Emitter Location and Signal Parameter Estimation,” *IEEE Transactions on Antennas and Propagation*, vol. 34, no. 3, pp. 276-280, March 1986.

[2] A. Paulaj, R. Roy, and T. Kailath, “Estimation of Signal Parameters Via Rotational Invariance Techniques - ESPRIT,” *Proceeding of 19th Asilomar Conference on Signals*, *Systems and Computers*, pp. 83-89, November 1985.

[3] H. A. Abdallah, W. Wasylkiwskyj, I. Kopriva, “Equalization of Numerically Calculated Element Patterns for Root-Based Direction Finding Algorithms,” *Applied Computational Electromagnetics Society (ACES) Journal*, vol. 21, no. 1, 2006.

[4] H. Changuel, A. Changuel, A. Gharsallah, “A New Method for Estimating the Direction-of-Arrival Waves by an Iterative Subspace-based Method,” *Applied Computational Electromagnetics Society (ACES) Journal*, vol. 25, no. 5, 2010.

[5] E. M. Al-Ardi, R. M. Shubair, M. E. Al-Mualla, “Direction of Arrival Estimation in a Multipath Environment: an Overview and a New Contribution,” *Applied Computational Electromagnetics Society (ACES) Journal*, vol. 21, no. 3, pp. 226-239, November 2006.

[6] D. Malioutov, M. Cetin, and A. S. Willsky, "A Sparse Signal Reconstruction Perspective for Source Localization with Sensor Arrays," *IEEE Transactions on Signal Processing*, vol. 53, no. 8, pp. 3010-3022, August 2003.

[7] M. Zoltowski and D. Stavrinides, "Sensor Array Signal Processing Via a Procrustes Rotations Based Eigenanalysis of the ESPRIT Data Pencil," *IEEE Transactions on Acoustic, Speech, Signal Processing*, vol. 37, no. 6, pp. 832-861, June 1989.

[8] A. J. van der Veen, P. B. Ober, and E. F. Deprettere, "Azimuth and Elevation Computation in High Resolution DOA Estimation," *IEEE Transactions on Signal Processing*, vol. 40, no. 7, pp. 1828-1832, July 1992.

[9] P. B. Ober, E. F. Dprettere, and A. J. van der Veen, "Efficient Methods to Compute Azimuth and Elevation in High-Resolution DOA Estimation," *Proceedings of ICASSP*, vol. 5, pp. 3349-3352, 1991.

[10] M. Donelli, F. Viani, P. Rocca, and A. Massa, "An Innovative Multiresolution Approach for DOA Estimation based on a Support Vector Classification," *IEEE Transactions on Antennas and Propagations*, vol. 57, no. 8, pp. 2279-2293, August 2009.

[11] H. Zhang, L. Ge, and Y. Wu, "Two-Dimension Direction Finding using Single-Snapshot Data," *International Conference on Communication Technology*, vol. 5, pp. 1-4, November 2006.

[12] H. M. Elkamchouchi, D. Abdel-Aziz, and M. M. M. Omar, "Two Dimensional Direction of Arrival Estimation using Single Snapshot of Nonuniformly Spaced Planar Array," *International Conference on Communication Technology*, vol. 5, pp. 1-4, November 2006.

[13] H. Semira, H. Belkacemi, and N. Doghmane, "Single Snapshot Projection Based Method for Azimuth/Elevation Directions of Arrival Estimation," *9th International Symposium on Signal Processing and Its Applications*, ISSPA 2007, pp. 1-4, Febuary 2007.

[14] D. Escot, D. Poyatos, I. Gonzalez, F. S. de Adana, and M. Catedra, "Application of Particle Swarm Optimization (PSO) to Single-Snapshot Direction of Arrival (DOA) Estimation," *2007 IEEE Antennas and Propagation Society International Symposium*, pp. 9-15, June 2007.

[15] K. Blackard, T. Rappaport, and C. Bostian, "Measurements and Models of Radio Frequency Impulsive Noise for Indoor Wireless Communications," *IEEE Journal on Selected Areas of Communications*, vol. 11, no. 7, pp. 991-1001, September 1993.

[16] S. G. Mallat and Z. Zhang, "Matching Pursuits with Time-Frequency Dictionary," *IEEE Transactions on Signal Processing*, vol. 41, no. 12, pp. 3397-3412, Dec. 1993.

[17] S. Chen and D. Donoho, "Basis Pursuit," in *Proc. of Twenty-eighth Asilomar Conf. Signals, Systems, Computers*, vol. 1, pp. 41-44, Nov. 1994.

[18] D. P. Wipf and B. D. Rao, "Bayesian Learning for Sparse Signal Reconstruction," *in Proc. of IEEE International Conference on Acoustics, Speech, and Signal Processing*, vol. 6, pp. 601-604, Apr. 2003.

[19] I. F. Gorodnitsky and B. D. Rao, "Sparse Signal Reconstruction from Limited Data Using FOCUSS: A Re-weighted Minimum Norm Algorithm," *IEEE Transactions on Signal Processing*, vol. 45, no. 3, pp. 600-616, Mar. 2002.

[20] Vapnik, "The Nature of Statistical Learning Theory," New York: Springer, 1995.

[21] M. Pastorino and A. Randazzo, "A Smart Antenna for the doa Estimation of Impinging Signals and Passive Obstacle Detection for Homeland Security," *Proc. IEEE Int. Workshopn Measurement Systems for Homeland Security, Contraband Detection and Personal Safety (IMS 2005)*, pp.70-75, 2005.

[22] C. J. C. Burges, "A Tutorial on Support Vector Machines for Pattern Recognition," *Data Mining and Knowledge Discovery*, vol. 2, pp. 121-167, 1998.

[23] J. J. Kormylo and J. M. Mendel, "Maximum Likelihood Detection and Estimation of Bernoulli-Gaussian Processes," *IEEE Transactions on Information Theory*, vol. 28, no. 3, pp. 482-488, May 1982.

[24] Q. S. Ren and A. J. Willis, "Extending MUSIC to Single Snapshot and on Line Direction Finding Applications," *IEE Radar 1997*, no. 449, pp. 783-787, October 1997.

Ying Zhang received the B.Eng. degree from the University of Electronic Science and Technology of China (UESTC), P. R. China, and the Ph.D. degree from the Nanyang Technological University, Singapore, both in Electronic Engineering (EE), in 2004 and 2010, respectively. She is currently an Associate Professor with the School of EE, UESTC, P. R. China. Her research interests include array signal processing, sparse signal representation and wireless communication.

Huapeng Zhao received the B.Eng. and M. Eng. degrees in electronic engineering from the University of Electronic Science and Technology of China, P. R. China, and the Ph.D. degree in Communication Engineering from the Nanyang Technological University, Singapore, in 2004, 2007, and 2012, respectively. Since the September of 2011, he has been working as a Scientist with the Department of Electronics and Photonics, Institute of High Performance Computing, Singapore. His research interests include computational electromagnetics, statistical electromagnetics, signal processing techniques in electromagnetics, and measurements in electromagnetic reverberation chamber.

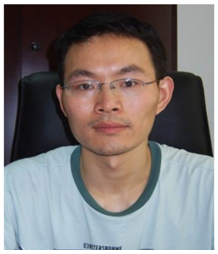

Qun Wan received the B.Sc. degree in applied physics from Nanjing University, China, in 1993. He received the M.Sc. and Ph.D. degrees in Electronic Engineering (EE) from the University of Electronic Science and Technology of China (UESTC), P. R. China, in 1996 and 2000, respectively. From 2001 to 2003, he was a Post-Doctoral Research Fellow with the Department of EE, Tinghua Univeristy, P. R. China. He is currently a professor with the School of EE, UESTC, P. R. China. His research interests include mobile localization, spectral estimation, sparse signal processing and array signal processing.

Spherical Aperture-Coupled Antennas with Parasitic Element

Javad S. Meiguni [1], Manoochehr Kamyab [1], and Ahmad Hosseinbeig [1]

[1] Faculty of Electrical and Computer Engineering
K. N. Toosi University of Technology, PO Box 16315-1355, Tehran 1431714191, Iran
meiguni@ee.kntu.ac.ir, kamyab@eetd.kntu.ac.ir, hosseinbeig@ee.kntu.ac.ir

Abstract **─** Theory and experiment of spherical aperture-coupled antennas with parasitic elements are presented in this paper. Current distributions on slot and conformal patches are calculated using spatial domain electric and magnetic Dyadic Green's Functions (DGFs). Electromagnetic fields for such a structure have been calculated with the aid of linear Rao-Wilton-Glisson (RWG) triangular basis functions and by converting spherical DGFs to Cartesian DGFs. In order to validate the proposed method, a prototype of this antenna is fabricated and tested. The effect of parasitic element on antenna characteristics such as gain and radiation pattern is investigated. Good agreement between the results shows accuracy and high convergence speed of the presented method.

Index Terms - Dyadic Green’s function, parasitic element, spherical aperture-coupled antennas, spherical to Cartesian transformation of DGFs.

I. INTRODUCTION

Aperture-coupled antennas have been investigated theoretically and experimentally over past decade. In such an antenna feed region is isolated from radiating region of the antenna due to the existence of ground plane. This property results in wide impedance matching and optimal array performance and shields the antenna elements from spurious radiation emitted by the feed line and RF devices [1-3].

Antennas mounted on multilayer spherical structures have been studied in recent years. Circular polarization can be achieved by proper design of these antennas which are suitable for satellite base stations and Line of Sight (LOS) applications [4-5]. There are several methods to analyze spherical antennas. Analysis methods based on Green's functions are more precise and faster [6-8]. In [9], a generalized method for the analysis of microstrip antennas placed on or embedded in multilayer hemispheres has been presented by using corresponding full-wave equivalent circuits. A hemispherical Dielectric Resonator Antenna (DRA) fed by a coaxial probe has been studied theoretically and experimentally in [10]. Both delta gap and magnetic frill source models have been considered to obtain the probe current from which the input impedance of the DRA has been calculated. Many investigations have been reported concerning DRAs located above slotted conducting plates [11-12]. The slot can be excited by a coaxial probe or through a microstrip line below the aperture. The existence of parasitic element improves impedance characteristics, directs antenna radiation patterns and reduces side lobes levels of patterns [13]. The use of a parasitic element in a DRA perturbs electromagnetic fields and excites two nearly degenerate orthogonal modes resulting in circular polarization [5].

In this paper, a multilayer spherical aperture-coupled antenna with a parasitic element is investigated. Due to the existence of spherical ground plane, the proposed antenna occupies less space in comparison with a DRA above a Perfect Electric Conductor (PEC) sheet. Current distribution on the narrow slot fed symmetrically by a coaxial probe is obtained by using mode-matching method and spatial domain Green's functions. Mutual couplings between slot and conformal antennas are calculated using scattering coefficients of magnetic DGFs of a multilayer sphere. A new approach is presented to convert spherical DGFs to Cartesian ones which is applied in calculation of electromagnetic fields inside and

Submitted On: July 7, 2012
Accepted On: Nov. 23, 2012

outside the antenna. The radiating elements are meshed with linear triangles. The effect of conformal patches on the slot is developed and the input impedance and radiation patterns of such an antenna are evaluated. A prototype is fabricated and tested and the measurement results are compared with those obtained from the proposed method.

II. THEORY

Figure 1 shows a spherical multilayer aperture-coupled antenna. Radiating elements may be of any arbitrary shape. Circular elements are preferred here due to their homogenous current distributions which result in lower side lobes levels in antenna radiation patterns. Each layer has permittivity and permeability of ε_i , μ_i, respectively. The conducting spherical core (layer 4) is modeled by $\varepsilon_4 \to \infty$, $\mu_4 \to 0$ in order for the propagation constant to be finite [14]. Full-wave analysis of this antenna is performed by using electric and magnetic DGFs of a four-layer sphere. The analysis based on DGFs and Method of Moments (MoM) has more calculation speed and accuracy in comparison with simulator packages. Simulator packages are highly dependent on meshing the structure, probe modeling and the size of radiation box. These limitations are not encountered in the presented analysis. Convergence speed of multilayer spherical DGFs is related to the radii of spheres and permittivities of layers. More spherical harmonic terms should be considered for greater radii and permittivities.

A. Analysis of Conformal Aperture-Coupled Antenna with Parasitic Element

Full-wave analysis of this antenna is performed by first investigating the effect of the rectangular slot by using the approach presented in [15]. Afterward, mutual couplings between the slot and conformal radiating elements are computed by using scattering DGFs of a four-layer sphere. The rectangular narrow slot can be analyzed using mode-matching method in spatial domain [15]. Based on the equivalence principle, magnetic current in the slot ($\mathbf{M}_s$) is modeled by a $2\mathbf{M}_s$ magnetic current over a whole sphere.

A delta gap source is used to model the excitation current. For a slot located between air and dielectric medium, as shown in Fig. 1, $k_e = \sqrt{(\varepsilon_r + 1)/2}\, k_0$ is the effective wave number of the slot. As this method is reported in details in [15], it will not be repeated here.

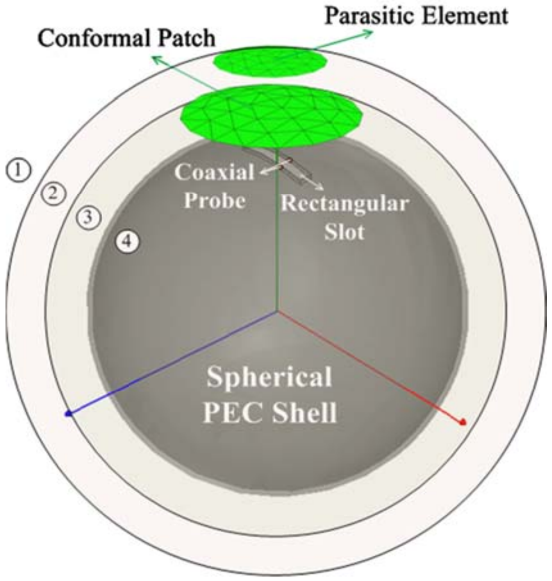

Fig. 1. Spherical aperture-coupled antenna with parasitic element.

A coaxial probe can be used to excite the slot. In this case, feed position affects the input impedance of the antenna. Regarding the input impedance diagram of the slot, the resonance frequency of the slot can be distinguished from those of the sphere due to high quality factor resonances of the sphere. If the slot is excited from its center, its second harmonic response does not affect the input impedance and subsequently the resonance frequencies of the sphere [15].

After calculating the magnetic current in the slot, magnetic fields ($\mathbf{H}$) on radiating elements are derived by using magnetic DGFs. The electric surface currents on these elements are computed from $\mathbf{J}_s = \mathbf{n} \times \mathbf{H}$, where $\mathbf{n}$ is the normal vector to the surface of the sphere. Magnetic field due to $\mathbf{M}_s$ in the slot is carried out by using the following expression:

$$\mathbf{H}(r,\theta,\varphi) = -j\omega\varepsilon_f \iint_{s'} \overline{\mathbf{G}}_M^{(fs)} . \mathbf{M}_s(\mathbf{r}'(r',\theta',\varphi'))\, ds'. \quad (1)$$

$\mathbf{r}(r,\theta,\varphi)$ and $\mathbf{r}'(r',\theta',\varphi')$ refer to field and source vectors, respectively. The surfaces of patch antenna and parasitic element are meshed by linear triangles in order to calculate current distributions. Vector currents are assigned on common edges between plus and minus triangles based on RWG method [16]. The centers of triangles are used to compute $\overline{\mathbf{G}}_M^{(fs)}$. Magnetic field of a conformal antenna can be calculated with good approximation by applying 3-point Gauss-Legendre integration. Equations of the required magnetic DGFs are presented in appendix1. The double summation in the spherical DGFs can be reduced to an expression with only a single summation by using the following relation [17]:

$$P_n(\cos\gamma) = \sum_{m=0}^{n} \left(2-\delta_m^0\right) \frac{(n-m)!}{(n+m)!} \times P_n^m(\cos\theta)\, P_n^m(\cos\theta')\cos\left(m(\varphi-\varphi')\right), \qquad (2)$$

where $\cos\gamma = \cos\theta\cos\theta' + \sin\theta\sin\theta'\cos(\varphi-\varphi')$. This technique increases the convergence speed of DGFs. In the analysis of the studied antenna, the first 25 terms in the summation are considered regarding the size and dielectric constants of layers. Dimensions of the spherical aperture-coupled antenna with radiating elements are given in Table 1.

Table 1: Dimensions of the spherical aperture-coupled antenna with radiating elements

PEC sphere radius	50 mm
Layer 2 (ε_r=1) thickness	20 mm
Layer 3 (ε_r=2.33) thickness	0.8 mm
Rectangular slot	3 mm*20 mm
Conformal patch antenna	$0^\circ < \theta_{Patch} < 20.3^\circ$
Parasitic element	$0^\circ < \theta_{Parasitic} < 7^\circ$

The input impedance of the antenna is affected by the loading of conformal radiating elements above the slot. However, the fundamental excited mode in the slot is not changed (i.e. TE$_{10}$ mode, assuming a narrow slot) and the direction of the electric field vector is transverse to the width of the slot. It can be shown that the parasitic element has negligible effect on the current distribution of conformal patch. Therefore, it is sufficient to take into account the loading effects of patch and parasitic element on the slot in the computation of the input impedance. In this case, electric field in the slot (layer 3) can be computed after calculating $\mathbf{J}_{s1}$ and $\mathbf{J}_{s2}$ which are current distributions on parasitic element and patch antenna, respectively. Then considering $\mathbf{E}^{(3)}$ as the electric field in the slot due to $\mathbf{J}_{s1}$ and $\mathbf{J}_{s2}$, the coupled magnetic current in the slot is calculated by using $\mathbf{M}_{1s} = -\mathbf{n}\times\mathbf{E}^{(3)}$, in which:

$$\mathbf{E}^{(3)} = -j\,\omega\,\mu_3 \left(\begin{array}{l} \iint_{s'} \overline{\mathbf{G}}_E^{(31)}.\mathbf{J}_{s1}(\mathbf{r}')\,ds' + \\ \iint_{s'} \overline{\mathbf{G}}_E^{(32)}.\mathbf{J}_{s2}(\mathbf{r}')\,ds' \end{array} \right), \qquad (3)$$

where $\overline{\mathbf{G}}_E^{(31)}$ and $\overline{\mathbf{G}}_E^{(32)}$ have been presented in [18].

B. Spherical to Cartesian Transformation of DGFs

In order to obtain electromagnetic field components, multiplication of DGFs and current element vector components is required in the same coordinates. If the conformal antenna surface is divided into curvilinear triangles as shown in Fig. 2 (a), θ and φ components of the current vector are considered which are in harmony with spherical components of DGFs [15]. However choosing curvilinear meshing in general can be complicated as compared with linear triangular meshing considered in this paper. As current vectors on common edges of linear meshes have Cartesian components, a new approach for dyad and vector multiplication is presented in this paper. Since J_φ and J_θ are different in each point of the edge such as $\mathbf{V}_x$ shown in Fig. 2(b), non-unique vectors are resulted from conversion of a current vector $\mathbf{V}$ from Cartesian to spherical coordinates.

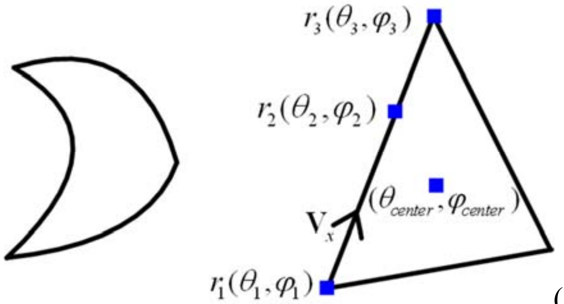

(a)

(b)

Fig. 2. (a) Curvilinear triangle, (b) Linear triangle.

The drawback stated above can be greatly reduced by employing the centers of the field and source triangles in spherical coordinates. Since there are unique transformations of vectors from spherical to Cartesian coordinates, conversion of a spherical dyad to a Cartesian dyad can be exactly implemented. As an example the conversion equation of $\hat{r}\hat{r}$ component of a spherical dyad is extracted as follows:

$$\hat{r}\hat{r} = (\sin\theta_f \cos\varphi_f \,\hat{x} + \sin\theta_f \sin\varphi_f \,\hat{y} + \cos\theta_f \,\hat{z}) \quad (4)$$
$$(\sin\theta_s \cos\varphi_s \,\hat{x} + \sin\theta_s \sin\varphi_s \,\hat{y} + \cos\theta_s \,\hat{z}),$$

in which subscripts f and s refer to field and source points, respectively. Accordingly each spherical DGFs ($\overline{\mathbf{G}}_1^{(fs)}$) can be converted to Cartesian DGFs ($\overline{\mathbf{G}}_2^{(fs)}$). Relations between Cartesian and spherical components are presented in appendix 2. The electric field vector can be expressed as:

$$\mathbf{E}^{(Cartesian)} = -j\omega\mu_f \iint_{s'} \overline{\mathbf{G}}^{(Cartesian)}.\mathbf{J}^{(Cartesian)}(\mathbf{r}')\,ds'. \quad (5)$$

Using this approach is efficient when a vector is requested as the output of an antenna problem solution. Therefore, all E_x, E_y, E_z components of electric field can be calculated to determine near and far field radiation patterns of an antenna. Far-field components can be calculated by integrating over the multiplication of the current of each source element and its corresponding DGFs and using the superposition principle. The 20 first terms in the summation of $\overline{\mathbf{G}}_E^{(11)}$ and $\overline{\mathbf{G}}_E^{(12)}$ are used to calculate electric fields due to $\mathbf{J}_{s1}$ and $\mathbf{J}_{s2}$, respectively. It should be mentioned that the algebraic conversion of nine spherical dyads to Cartesian ones requires very low time and memory (about 0.001 times the memory and time taken by calculation of 20 spherical harmonics terms for such an antenna structure). It takes about 9 minutes to compute E- or H-planes radiation patterns (with 60 divisions of θ) with a Core 2 Quad @ 2.86 GHz processor. The proposed method has more calculation speed in comparison with the CAD simulator packages and can be utilized in analysis of various spherical antennas such as a probe fed spherical microstrip antenna with radial current components.

III. RESULTS

In order to validate the proposed method, a prototype of an aperture-coupled antenna with a parasitic element is fabricated and tested. A 3mm*20mm slot is cut on a 5cm radius PEC sphere and is excited at its center through a 20cm RG-58U coaxial cable of 50Ω characteristic impedance. A circular patch has been made from a RT/duroid 5870 substrate of 0.8mm thickness and with a relative permittivity of 2.33 located above the slot. Due to the thin substrate, the whole dielectric over PEC sphere can be modeled by a partial dielectric under patch antenna. A circular parasitic element is located above the patch by using a spacer material of unit relative permittivity. The implemented aperture-coupled antenna is shown in Fig. 3.

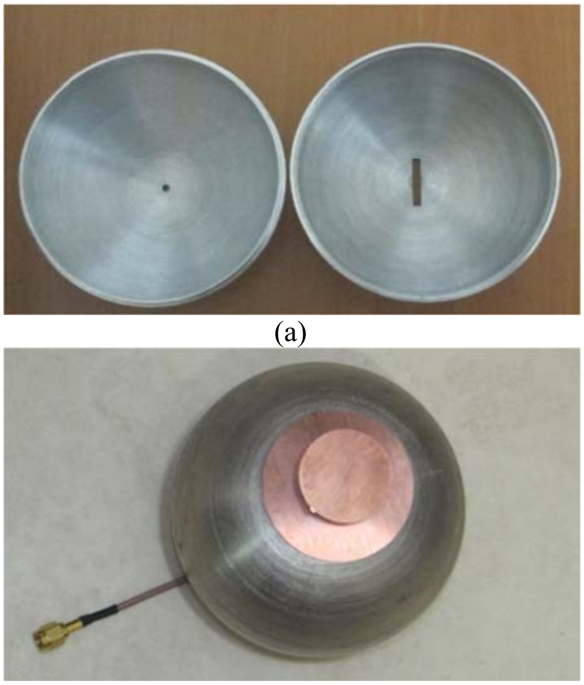
(a)

(b)

Fig. 3. Prototype of the spherical aperture-coupled antenna; (a) slotted PEC shell, (b) patch antenna with parasitic element.

The conformal patch antenna has been divided into 100 triangles yielding 140 common edges and the parasitic element has been divided into 36 triangles leading to 48 common edges. Figure 4 demonstrates the input impedance obtained from analytical solution and the measurement of the antenna. The E- and H-planes radiation patterns of the antenna are measured at 3.1GHz and are shown in Fig. 5. As it can be noticed, directed patterns with low side lobes levels are achieved from this antenna. Good agreement between the results of the proposed method and measurement is obtained. An efficiency of 87% at 3.1GHz has been obtained which is measured by Bluetest reverberation chamber. Figure 6 illustrates the antenna gain with and without the parasitic element. An increase in antenna gain is notable with the presence of the parasitic element. As shown in Fig. 7, parasitic element makes antenna radiation patterns more directive but it increases cross polarization radiations. The latter is because of electromagnetic fields perturbation due to the existence of parasitic element.

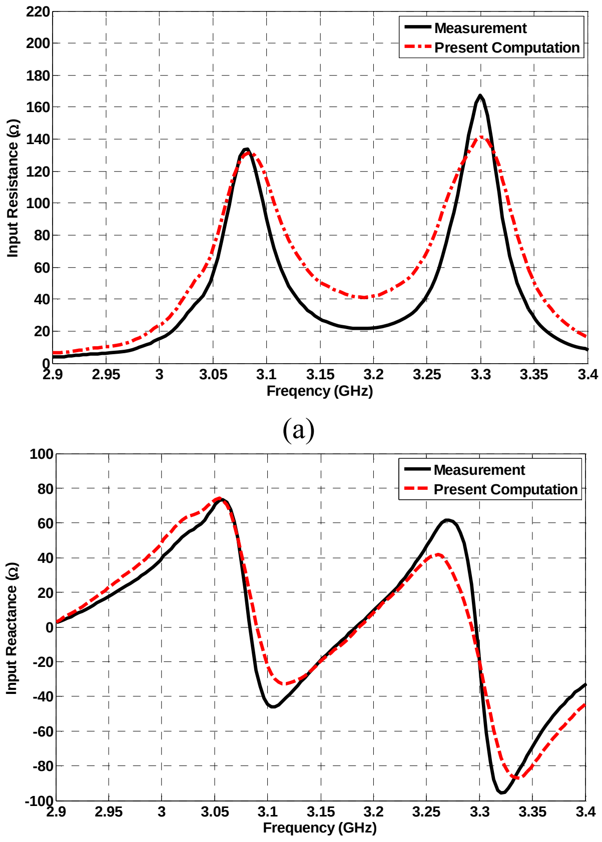

(a)

(b)

Fig. 4. Input impedance of the proposed antenna; (a) Resistance, (b) Reactance.

IV. CONCLUSION

In this paper, an efficient full-wave method has been presented to analyze spherical aperture-coupled patch antenna with parasitic element. Spatial domain DGFs in conjunction with MoM have been used in the analysis. Coupling effects between the patches and the slot have been investigated. In this method, electromagnetic fields vectors at entire medium have been computed by meshing the antenna into linear triangles in Cartesian coordinates and converting equations of dyads from spherical to Cartesian coordinates. Robustness and accuracy of the proposed method have been validated by comparing the results obtained from the proposed method with those of the measurement. Directive radiation patterns and low side lobes levels are some specific features of this antenna. The effect of the parasitic element on radiation patterns and gain of the antenna has been shown. An improvement is achieved in antenna gain and directivity due to the existence of the parasitic element.

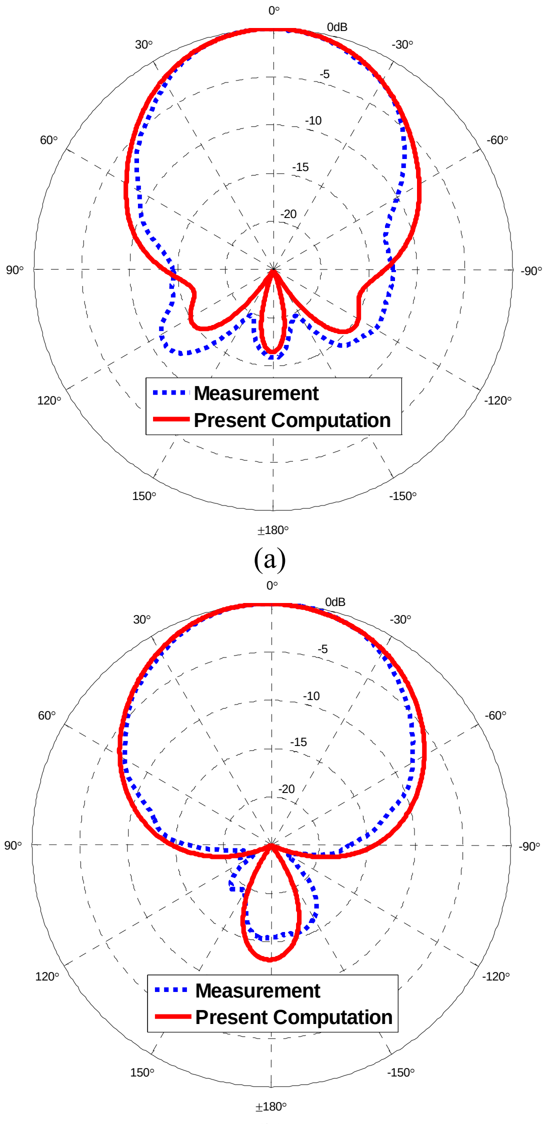

(a)

(b)

Fig. 5. Radiation patterns of the aperture-coupled antenna with parasitic element; (a) E-Plane, (b) H-Plane.

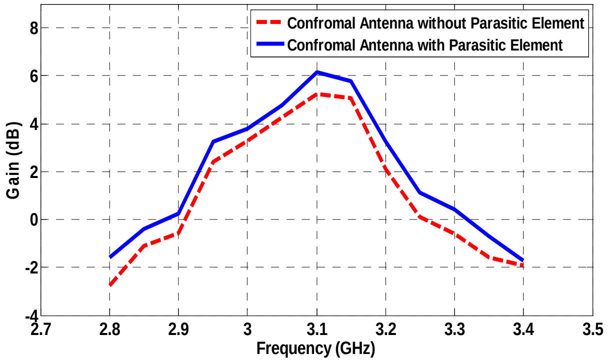

Fig. 6. Gain of the aperture-coupled antenna with and without parasitic element.

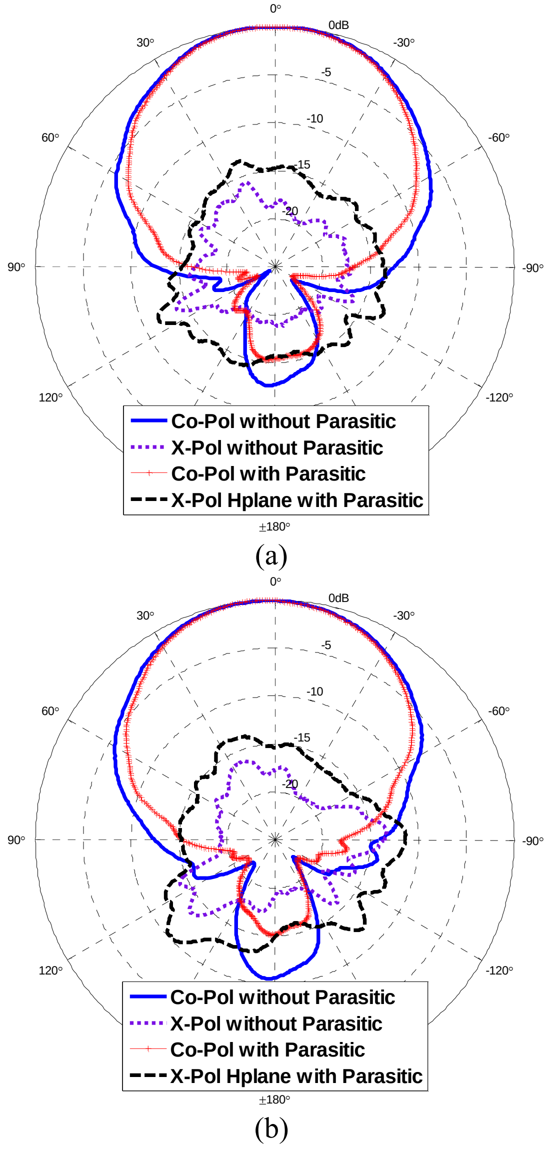

(a)

(b)

Fig. 7. Co- and cross-polar radiation (H-plane); (a) f=3.1GHz, (b) f=3.2GHz.

V. APPENDIX1

Magnetic DGFs ($\overline{\mathbf{G}}_M$) can be computed by using $\overline{\mathbf{G}}_E$ in [18] and the duality theorem. For the present antenna (Fig. 1), the scattering components of magnetic field in conformal radiating elements (layers 1, 2) due to the slot (layer 3) can be obtained by using the magnetic current source in layer *s=3* and considering the centers of triangles conformed in layers *f=1,2* as field points.

$$\overline{\mathbf{G}}_M^{(13)} = \frac{jk_3}{4\pi}\sum_{n=0}^{\infty}\sum_{m=0}^{n}\left(2-\delta_m^0\right)\frac{2n+1}{n(n+1)}\frac{(n-m)!}{(n+m)!} \times \left\{\begin{array}{l} a_M^{13}\mathbf{M}^{(2)}_{\substack{e\\o}mn}(k_f)\mathbf{M}'_{\substack{e\\o}mn}(k_3) \\ +b_M^{13}\mathbf{M}^{(2)}_{\substack{e\\o}mn}(k_f)\mathbf{M}'^{(2)}_{\substack{e\\o}mn}(k_3) \\ +a_N^{13}\mathbf{N}^{(2)}_{\substack{e\\o}mn}(k_f)\mathbf{N}'_{\substack{e\\o}mn}(k_3) \\ +b_N^{13}\mathbf{N}^{(2)}_{\substack{e\\o}mn}(k_f)\mathbf{N}'^{(2)}_{\substack{e\\o}mn}(k_3) \end{array}\right\}, \quad \text{(A1)}$$

$$\overline{\mathbf{G}}_M^{(23)} = \frac{jk_3}{4\pi}\sum_{n=0}^{\infty}\sum_{m=0}^{n}\left(2-\delta_m^0\right)\frac{2n+1}{n(n+1)}\frac{(n-m)!}{(n+m)!} \times \left\{\begin{array}{l} a_M^{23}\mathbf{M}^{(2)}_{\substack{e\\o}mn}(k_f)\mathbf{M}'_{\substack{e\\o}mn}(k_3) \\ +b_M^{23}\mathbf{M}^{(2)}_{\substack{e\\o}mn}(k_f)\mathbf{M}'^{(2)}_{\substack{e\\o}mn}(k_3) \\ +a_N^{23}\mathbf{N}^{(2)}_{\substack{e\\o}mn}(k_f)\mathbf{N}'_{\substack{e\\o}mn}(k_3) \\ +b_N^{23}\mathbf{N}^{(2)}_{\substack{e\\o}mn}(k_f)\mathbf{N}'^{(2)}_{\substack{e\\o}mn}(k_3) \\ +c_M^{23}\mathbf{M}_{\substack{e\\o}mn}(k_f)\mathbf{M}'_{\substack{e\\o}mn}(k_3) \\ +d_M^{23}\mathbf{M}_{\substack{e\\o}mn}(k_f)\mathbf{M}'^{(2)}_{\substack{e\\o}mn}(k_3) \\ +c_N^{23}\mathbf{N}_{\substack{e\\o}mn}(k_f)\mathbf{N}'_{\substack{e\\o}mn}(k_3) \\ +d_N^{23}\mathbf{N}_{\substack{e\\o}mn}(k_f)\mathbf{N}'^{(2)}_{\substack{e\\o}mn}(k_3) \end{array}\right\}, \quad \text{(A2)}$$

where δ_m^0 is the Kronecker delta, k_i is the propagation constant in i-th layer **M**, **N** and are orthogonal Eigen vectors in spherical coordinates with properties explained in [7]. The spherical Bessel or Hankel functions are of the second kind. Dyadic coefficients ($a_{M,N}$, $b_{M,N}$, $c_{M,N}$, $d_{M,N}$) can be computed by using the duality theorem.

VI. APPENDIX2

The components of the transformed spherical DGFs ($\overline{\mathbf{G}}_1^{(fs)}$) to Cartesian DGFs ($\overline{\mathbf{G}}_2^{(fs)}$) are expressed as follow:

$$\bar{\mathbf{G}}_1^{(fs)} = \begin{pmatrix} G_{rr} & G_{r\theta} & G_{r\varphi} \\ G_{\theta r} & G_{\theta\theta} & G_{\theta\varphi} \\ G_{\varphi r} & G_{\varphi\theta} & G_{\varphi\varphi} \end{pmatrix} \Rightarrow \bar{\mathbf{G}}_2^{(fs)} = \begin{pmatrix} G_{xx} & G_{xy} & G_{xz} \\ G_{yx} & G_{yy} & G_{yz} \\ G_{zx} & G_{zy} & G_{zz} \end{pmatrix} \tag{A3}$$

$$\begin{aligned} G_{xx} &= G_{rr}\sin\theta_f\cos\varphi_f\sin\theta_s\cos\varphi_s \\ &+G_{r\theta}\sin\theta_f\cos\varphi_f\cos\theta_s\cos\varphi_s - G_{r\varphi}\sin\theta_f\cos\varphi_f\sin\varphi_s \\ &+G_{\theta r}\cos\theta_f\cos\varphi_f\sin\theta_s\cos\varphi_s - G_{\varphi r}\sin\varphi_f\sin\theta_s\cos\varphi_s \\ &+G_{\theta\theta}\cos\theta_f\cos\varphi_f\cos\theta_s\cos\varphi_s - G_{\theta\varphi}\cos\theta_f\cos\varphi_f\sin\varphi_s \\ &-G_{\varphi\theta}\sin\varphi_f\cos\theta_s\cos\varphi_s + G_{\varphi\varphi}\sin\varphi_f\sin\varphi_s \end{aligned} \tag{A4}$$

$$\begin{aligned} G_{xy} &= G_{rr}\sin\theta_f\cos\varphi_f\sin\theta_s\sin\varphi_s \\ &+G_{r\theta}\sin\theta_f\cos\varphi_f\cos\theta_s\sin\varphi_s + G_{r\varphi}\sin\theta_f\cos\varphi_f\cos\varphi_s \\ &+G_{\theta r}\cos\theta_f\cos\varphi_f\sin\theta_s\sin\varphi_s - G_{\varphi r}\sin\varphi_f\sin\theta_s\sin\varphi_s \\ &+G_{\theta\theta}\cos\theta_f\cos\varphi_f\cos\theta_s\sin\varphi_s + G_{\theta\varphi}\cos\theta_f\cos\varphi_f\cos\varphi_s \\ &-G_{\varphi\theta}\sin\varphi_f\cos\theta_s\sin\varphi_s - G_{\varphi\varphi}\sin\varphi_f\cos\varphi_s \end{aligned} \tag{A5}$$

$$\begin{aligned} G_{xz} &= G_{rr}\sin\theta_f\cos\varphi_f\cos\theta_s - G_{r\theta}\sin\theta_f\cos\varphi_f\sin\theta_s \\ &+G_{\theta r}\cos\theta_f\cos\varphi_f\cos\theta_s - G_{\varphi r}\sin\varphi_f\cos\theta_s \\ &-G_{\theta\theta}\cos\theta_f\cos\varphi_f\sin\theta_s + G_{\varphi\theta}\sin\varphi_f\sin\theta_s \end{aligned} \tag{A6}$$

$$\begin{aligned} G_{yx} &= G_{rr}\sin\theta_f\sin\varphi_f\sin\theta_s\cos\varphi_s \\ &+G_{r\theta}\sin\theta_f\sin\varphi_f\cos\theta_s\cos\varphi_s - G_{r\varphi}\sin\theta_f\sin\varphi_f\sin\varphi_s \\ &+G_{\theta r}\cos\theta_f\sin\varphi_f\sin\theta_s\cos\varphi_s + G_{\varphi r}\cos\varphi_f\sin\theta_s\cos\varphi_s \\ &+G_{\theta\theta}\cos\theta_f\sin\varphi_f\cos\theta_s\cos\varphi_s - G_{\theta\varphi}\cos\theta_f\sin\varphi_f\sin\varphi_s \\ &+G_{\varphi\theta}\cos\varphi_f\cos\theta_s\cos\varphi_s - G_{\varphi\varphi}\cos\varphi_f\sin\varphi_s \end{aligned} \tag{A7}$$

$$\begin{aligned} G_{yy} &= G_{rr}\sin\theta_f\sin\varphi_f\sin\theta_s\sin\varphi_s \\ &+G_{r\theta}\sin\theta_f\sin\varphi_f\cos\theta_s\sin\varphi_s + G_{r\varphi}\sin\theta_f\sin\varphi_f\cos\varphi_s \\ &+G_{\theta r}\cos\theta_f\sin\varphi_f\sin\theta_s\sin\varphi_s + G_{\varphi r}\cos\varphi_f\sin\theta_s\sin\varphi_s \\ &+G_{\theta\theta}\cos\theta_f\sin\varphi_f\cos\theta_s\sin\varphi_s + G_{\theta\varphi}\cos\theta_f\sin\varphi_f\cos\varphi_s \\ &+G_{\varphi\theta}\cos\varphi_f\cos\theta_s\sin\varphi_s + G_{\varphi\varphi}\cos\varphi_f\cos\varphi_s \end{aligned} \tag{A8}$$

$$\begin{aligned} G_{yz} &= G_{rr}\sin\theta_f\sin\varphi_f\cos\theta_s - G_{r\theta}\sin\theta_f\sin\varphi_f\sin\theta_s \\ &+G_{\theta r}\cos\theta_f\sin\varphi_f\cos\theta_s + G_{\varphi r}\cos\varphi_f\cos\theta_s \\ &-G_{\theta\theta}\cos\theta_f\sin\varphi_f\sin\theta_s - G_{\varphi\theta}\cos\varphi_f\sin\theta_s \end{aligned} \tag{A9}$$

$$\begin{aligned} G_{zx} &= G_{rr}\cos\theta_f\sin\theta_s\cos\varphi_s - G_{r\varphi}\cos\theta_f\sin\varphi_s \\ &+G_{r\theta}\cos\theta_f\cos\theta_s\cos\varphi_s - G_{\theta r}\sin\theta_f\sin\theta_s\cos\varphi_s \\ &-G_{\theta\theta}\sin\theta_f\cos\theta_s\cos\varphi_s + G_{\theta\varphi}\sin\theta_f\sin\varphi_s \end{aligned} \tag{A10}$$

$$\begin{aligned} G_{zy} &= G_{rr}\cos\theta_f\sin\theta_s\sin\varphi_s + G_{r\varphi}\cos\theta_f\cos\varphi_s \\ &+G_{r\theta}\cos\theta_f\cos\theta_s\sin\varphi_s - G_{\theta r}\sin\theta_f\sin\theta_s\sin\varphi_s \\ &-G_{\theta\theta}\sin\theta_f\cos\theta_s\sin\varphi_s - G_{\theta\varphi}\sin\theta_f\cos\varphi_s \end{aligned} \tag{A11}$$

$$\begin{aligned} G_{zz} &= G_{rr}\cos\theta_f\cos\theta_s - G_{r\theta}\cos\theta_f\sin\theta_s \\ &-G_{\theta r}\sin\theta_f\cos\theta_s + G_{\theta\theta}\sin\theta_f\sin\theta_s \end{aligned} \tag{A12}$$

ACKNOWLEDGMENT

The authors would like to thank the Research Institute of ICT (former Iran Telecommunication Research Center) for its support.

REFERENCES

[1] D. M. Pozar, "Microstrip Antenna Aperture-Coupled to a Microstrip-Line," *Electron. Lett.*, vol. 21, no. 2, pp.49-50, Jan. 1985.

[2] W. Huang and A. Kishk, "Apertures-Coupled Multi-Layer Cylindrical Dielectric Resonator Antennas and Modal Analysis," 23rd Annual Review of Progress in *Applied Computational Electromagnetics Society (ACES) Journal*, Verona, Italy, pp. 1117-1120, March 2007.

[3] J. G. Davis, P. Shakespeare, and N. Kiley, "Evaluation of Circular Aperture Transmission Coefficients in the Presence of Obscurations," *Applied Computational Electromagnetics Society (ACES) Journal*, vol. 26, no. 9, pp. 723-728, Sep. 2011.

[4] K. W. Leung, W. C. Wong, K. M. Luk, and E. K. N. Yung, "Circular Polarized Dielectric Resonator Antenna Excited by Dual Conformal Strips," *Electron. Lett.*, vol. 36, no. 6, pp. 484-486, March 2000.

[5] K. W. Leung and H. K. Ng, "Theory and Experiment of Circularly Polarized Dielectric Resonator Antenna with a Parasitic Patch," *IEEE Trans. Antennas Propag.*, vol. 51, no. 3, pp. 405-412, March 2003.

[6] W. C. Chew, *Waves and Fields in Inhomogeneous Media*, IEEE Press Series on Electromagnetic Waves, New York, 1995.

[7] C. T. Tai, *Dyadic Green's Functions in Electromagnetics Theory*, IEEE Press Series on Electromagnetic Waves, New York, 1994.

[8] J. V. Bladel, *Electromagnetic Fields*, second edition, IEEE press, John Wiley & Sons, Inc., 2007.

[9] T. V. B. Giang, M. Thiel, and A. Dreher, "A Unified Approach to the Analysis of Radial Waveguides, Dielectric Resonators, and Microstrip Antennas on Spherical Multilayer Structures," *IEEE Trans. Microwave Theory and Techniques* , vol. 53, no. 1, pp. 404-409, Jan. 2005.

[10] K. W. Leung, K. M. Luk, K. Y. A. Lai, and D. Lin, "Theory and Experiment of a Coaxial Probe Fed Hemispherical Dielectric Resonator Antenna," *IEEE Trans. Antennas Propag.,* vol. 41, no. 10, pp. 1390-1398, Oct. 1993.

[11] K. W. Leung and H. K. Ng, "The Slot-Coupled Hemispherical Dielectric Resonator Antenna with a Parasitic Patch: Applications to the Circularly Polarized Antenna and Wide-Band Antenna," *IEEE Trans. Antennas Propag.,* vol. 53, no. 5, pp. 1762-1769, May 2005.

[12] K. K. So and K. W. Leung, "Bandwidth Enhancement and Frequency Tuning of the Dielectric Resonator Antenna using a Parasitic Slot in the Ground Plane," *IEEE Trans. Antennas Propag.,* vol. 53, no. 5, pp. 1762-1769, May 2005.

[13] J. Sun and T. Li, "Dual-Frequency Dielectric Resonator Antenna with Inverse T-shape Parasitic Strip," 23rd Annual Review of Progress in *Applied Computational Electromagnetics Society (ACES) Journal,* Honolulu, Hawaii, April 2005.

[14] J. S. Meiguni, M. Kamyab, and A. Hosseinbeig, "Electromagnetic Characteristics of Conformal Dipole Antennas over a PEC Sphere," *Progress In Electromagnetics Research M*, vol. 26, pp. 85-100, 2012.

[15] K. W. Leung, "Theory and Experiment of a Rectangular Slot on a Sphere," *IEEE Trans. Microwave Theory Tech.,* vol. MTT-46, no. 12, pp. 2117-2123, Dec. 1998.

[16] S. M. Rao, D. R. Wilton, and A. W. Glisson, "Electromagnetic Scattering by Surfaces of Arbitrary Shape," *IEEE Trans. Antennas Propag.*, vol. 30, pp. 409-418, May 1982.

[17] R. F. Harrington, *Time-Harmonic Electromagnetic Fields*, IEEE press, John Wiley & Sons Inc., 2001.

[18] L.W. Li, P. S. Kooi, M. S. Leong, and T. S. Yeo, "Electromagnetic Dyadic Green's Function in Spherically Multilayered Media," *IEEE Trans. Microwave Theory Tech.,* vol. 42, pp. 2302-2310, Dec. 1994.

Javad Soleiman Meiguni was born in 1982 in Tehran, Iran. He received his B.S. from Semnan University, Semnan, Iran and M.S. from K. N. Toosi University of Technology, Tehran, Iran in 2005 and 2008, respectively all in Electrical Engineering. He has been working towards Ph.D. in Telecommunications at K. N. Toosi University of Technology, Tehran, Iran. He has participated in many projects inside and outside the university. Currently, he is working on analysis and design of spherical aperture-coupled antennas using Dyadic Green's Functions. His research is mainly focused on the areas of antennas and EM modeling, numerical techniques in electromagnetics, antenna design and measurement, active and passive microwave and millimeter-wave circuit design.

Manoochehr Kamyab received the B.S. and M.S. from the University of Tehran, Tehran, Iran, and the PhD degree from Michigan State University, in 1982, in Electrical Engineering. His research interests include the metamaterials and their applications in antenna engineering, electrically small antennas, microwave and millimeter-wave circuits, and mobile communication systems. He is currently a professor in the Department of Electrical Engineering, K.N. Toosi University of Technology, Tehran, Iran. Professor Kamyab is leading a group of graduate students in the areas of negative-refraction metamaterials and their microwave applications, integrated antennas and components for broad-band wireless telecommunications, novel antenna beam-steering techniques, millimeter and sub-millimeter-wave circuits, as well as scattering and inverse scattering problems.

Ahmad Hosseinbeig was born in 1983 in Tehran, Iran. He received the B.S. in Electrical Engineering from Shahid Bahonar University, Kerman, Iran and M.S. in Telecommunications Engineering from K. N. Toosi University of Technology, Tehran, Iran in 2006 and 2008, respectively. He is presently studying for a Ph.D. in Telecommunications Engineering at K. N. Toosi University of Technology, Tehran, Iran. He is currently working on analysis and design of spherical aperture-coupled Dielectric Resonator Antennas (DRA) using Dyadic Green's Functions. His main research interests are in the fields of numerical techniques in electromagnetic theory, antenna design and measurement, microwave and high frequency circuit design.

Enhanced Bandwidth Ultra-Wideband Small Monopole Antenna with Variable Band-Stop Function

M. T. Partovi [1], N. Ojaroudi [2], M. Ojaroudi [3], and N. Ghadimi [3]

[1] Department of Electrical Engineering,
Aeronautical University of Science and Technology, Tehran, Iran.
partovimt@gmail.com

[2] Department of Electrical Engineering
Ardabil Branch, Islamic Azad University, Ardabil, Iran
n_ojaroudi@srttu.edu

[3] Young Researchers Club
Ardabil Branch, Islamic Azad University, Ardabil, Iran
m.ojaroudi@iauardabil.ac.ir, noradin.ghadimi@gmail.com

Abstract **─** In this paper a novel ultra wideband monopole antenna with frequency band-stop performance is designed and manufactured. The proposed antenna consists of square radiating patch with a T-shaped ring slot and ground plane with two G-shaped slots. In the proposed structure, by cutting two G-shaped slots in the ground plane, additional resonance is excited and hence much wider impedance bandwidth can be produced, especially at the higher band. In order to create band-rejected function we use a T-shaped ring slot in the radiating patch. The fabricated antenna has the frequency band of 2.95 to over 15.65 GHz with a rejection band around 5.13-5.91 GHz. Good return loss and radiation pattern characteristics are obtained in the frequency band of interest. Simulated and measured results are presented to validate the usefulness of the proposed antenna structure for UWB applications.

Index Terms **─** Frequency Band-Notch Function, G-Shaped Slot, T-Ring Slot, Ultra-Wideband (UWB).

I. INTRODUCTION

Communication systems usually require smaller antenna size in order to meet the miniaturization requirements of radio-frequency (RF) units [1]. It is a well-known fact that planar monopole antennas present really appealing physical features, such as simple structure, small size, and low cost. Due to all these interesting characteristics, planar monopoles are extremely attractive to be used in emerging UWB applications, and growing research activity is being focused on them. Consequently, a number of planar monopoles with different geometries have been experimentally characterized [2]-[3].

The frequency range for UWB systems between 3.1-10.6 GHz will cause interference to the existing wireless communication systems for example the wireless local area network (WLAN) for IEEE 802.11a operating in 5.15-5.35 GHz and 5.725-5.825 GHz bands, so the UWB antenna with a band-notch function is required. Lately to generate the frequency band-notch function, modified planar monopoles several antennas with band-notch characteristic have been reported [4-8]. In [4], [5] and [6], different shapes of the slots (i.e., W-shaped, L-shaped and folded trapezoid) are used to obtain the desired band notched characteristics. Single and multiple [7] half wavelength U-shaped slots are embedded in the radiation patch to generate the single and multiple

Submitted On: Mar. 8, 2012
Accepted On: Aug. 22, 2012

band-notched functions, respectively. Other automatic design methods have been developed to achieve band-notch performance [8].

In this paper, a simple method for designing a novel and compact microstrip-fed monopole antenna with band-notch characteristic for UWB applications has been presented. In the proposed antenna, based on defected ground structure, for bandwidth enhancement we use two G-shaped slots on the ground plane. Also by using a T-shaped ring slot with variable dimensions on the square radiating patch a band-stop performance can be created. The presented monopole antenna has a small size of $12\times 18\ \text{mm}^2$. The size of the designed antenna is smaller than the UWB antennas with band-notched function reported recently, which has at least a size reduction of 15% with respect to the previous similar antenna [4-8]. Good return loss and radiation pattern characteristics are obtained in the frequency band of interest. Simulated and measured results are presented to validate the usefulness of the proposed antenna structure for UWB applications.

In the proposed structure, by cutting the modified T-shaped ring slot of suitable dimensions at the monopole's patch a double fed structure can be constructed. This structure has a novel feeding configuration that consists of a splitting network connected to two symmetrical ports on its base. Using the Theory of Characteristic Modes it has been demonstrated that the insertion of two symmetric feed ports prevents the excitation of horizontal currents and assures that only the dominant vertical current mode is present in the structure [2]. As a result, unlike other antennas reported in the literature to date [5]-[9], the proposed antenna displays a good omni-directional with low cross-polarization level radiation pattern even at higher frequencies.

II. ANTENNA DESIGN

The presented small square monopole antenna fed by a microstrip line is shown in Fig. 1, which is printed on an FR4 substrate of thickness 1.6 mm, permittivity 4.4, and loss tangent 0.018. The basic monopole antenna structure consists of a square patch, a feed line, and a ground plane. The square patch has a width W. The patch is connected to a feed line of width of W_f and length of L_f .The width of the microstrip feed line is fixed at 2 mm. On the other side of the substrate, a conducting ground plane is placed. The proposed antenna is connected to a 50- SMA connector for signal transmission.

Regarding defected ground structures (DGS), the creating slots in the ground plane provide an additional current path. Moreover, this structure changes the inductance and capacitance of the input impedance, which in turn leads to change the bandwidth. The DGS applied to a microstrip line causes a resonant character of the structure transmission with a resonant frequency controllable by changing the shape and size of the slot [8]. Therefore, by cutting two G-shaped slots at the ground plane and carefully adjusting its parameters, much enhanced impedance bandwidth may be achieved. In addition, as illustrated in Fig. 1, a T-shaped ring slot in the radiating patch can perturb the resonant response and also acts as a half-wave resonant structure [3]-[5]. At the notch frequency, the current concentrated on the edges of the interior and exterior of the T-shaped ring slot. As a result, the desired high attenuation near the notch frequency can be produced. The final dimensions of the designed antenna are specified in Table I.

Table I: The final dimensions of the designed antenna

Param.	mm	Param.	mm	Param.	mm
W_{Sub}	10	L_{Sub}	16	L_f	6
L_V	1.5	L_S	7	L_{S2}	7
W_P	9	L	0.5	W	0.5
W_{S1}	2	L_{S1}	0.5	W_{S2}	3
W_{S3}	1	L_{S3}	2.5	W_V	2
W_{V1}	1	W_{V2}	1	L_{gnd}	1

III. RESULTS AND DISCUSSIONS

In this Section, the microstrip monopole antenna with various design parameters were constructed, and the numerical and experimental results of the input impedance and radiation characteristics are presented and discussed. The parameters of this proposed antenna are studied by changing one parameter at a time and fixing the others. The simulated results are obtained using the Ansoft simulation software high-frequency structure simulator (HFSS) [9].

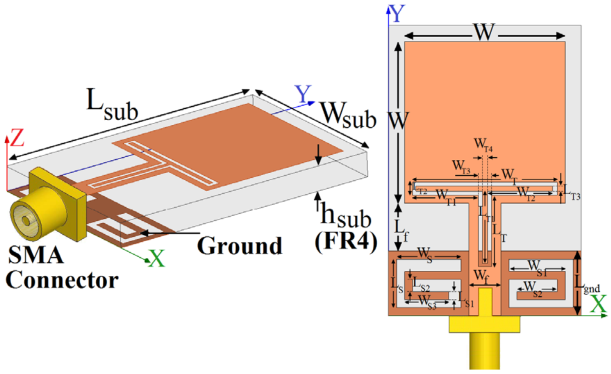

(a) **(b)**

Fig. 1. Geometry of the proposed antenna, (a) side view, (b) top view.

Figure 2 shows the structure of the various monopole antennas used for new additional resonance and band notch performance simulation studies. VSWR characteristics for ordinary square monopole antenna (Fig. 2(a)), with a pair of G-shaped slots in the ground plane (Fig. 2(b)), and the proposed antenna structure (Fig. 2(c)) are compared in Fig. 3. Fig. As shown in Fig. 3, it is found that by inserting a pair of G-shaped slots in the ground plane, the antenna can create the third resonant frequency at 13 GHz. Also as shown in Fig. 3, in this structure, Also as shown in Fig. 3, in this structure, a modified T-shaped ring slot in the square radiating patch with variable dimensions is used in order to generate the frequency band stop performance. [6]-[7]. Also the input impedance of the various monopole antenna structures that shown in Fig. 2, on a Smith Chart is shown in Fig. 4.

To understand the phenomenon behind this new additional resonance performance, the simulated current distributions on the ground plane for the proposed antenna with two G-shaped slots at 13 GHz are presented in Fig. 5 (a). It can be observed in Fig. 5 (a) that the current concentrated on the edges of the interior and exterior of the two G-shaped slots at 13 GHz. Therefore, the antenna impedance changes at these frequencies due to the resonant properties of the G-shaped slots [8]. It is found that by using these slots, third resonance at 13 GHz. Another important design parameter of this structure is the T-shaped ring slot in radiating patch. Figure 5 (b) presents the simulated current distributions on the ground plane at the notch frequency (5.5 GHz). As shown in Fig. 5 (b), at the notch frequency the current flows are more dominant around of the T-shaped ring slot. As a result, the desired high attenuation near the notch frequency can be produced [6]-[7].

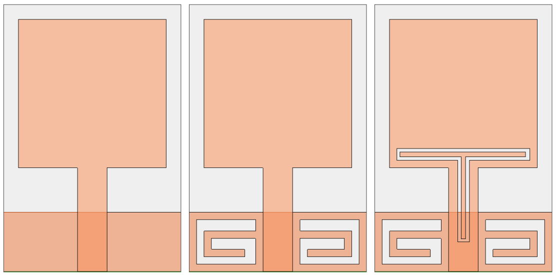

(a) **(b)** **(c)**

Fig. 2. (a) The basic structure (ordinary square antenna), (b) square antenna with two G-shaped slots, (c) the proposed antenna.

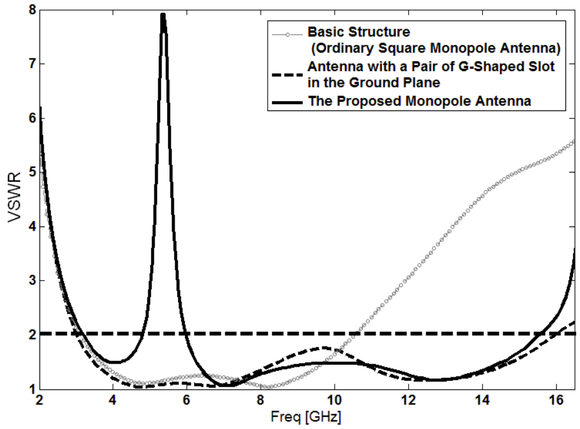

Fig. 3. Simulated VSWR characteristics for the antennas shown in Fig. 2.

In this study, the T-shaped ring slot is used in order to generate the frequency band-stop performance as displayed in Fig. 1. The simulated VSWR curves with different values of W_1 are plotted in Fig. 6. As shown in Fig. 6, when the interior width of the T-shaped ring slot increases from 1 to 2.5 mm, the center of notch frequency is increases from 4. 3 to 6.7 GHz. From these results, we can conclude that the notch frequency is controllable by changing the interior width of the T-shaped ring slot.

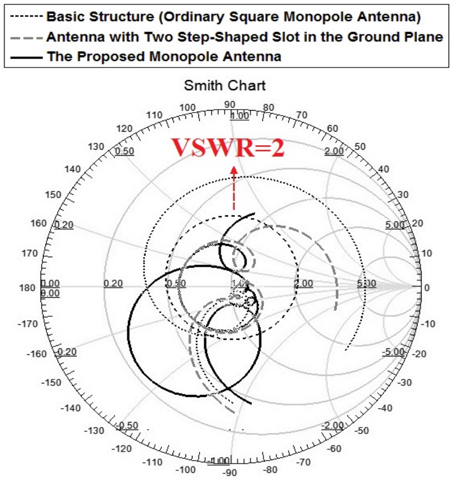

Fig. 4. The simulated input impedance on a Smith chart of the various monopole antenna structures shown in Fig. 2.

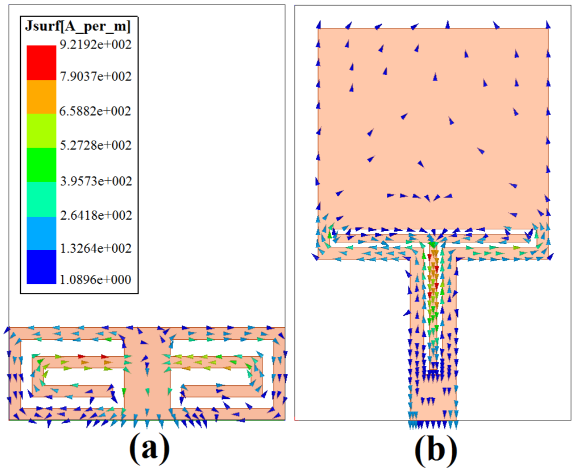

Fig. 5. Simulated surface current distributions for the proposed antenna, (a) on the ground plane at 13 GHz (third resonance frequency), (b) on the radiating patch at 5.5 GHz (notch frequency).

Another main effect of the T-shaped ring slot occurs on the filter bandwidth. In this structure, the width L_1, is the critical parameter to control the filter bandwidth. Figure 7 illustrates the simulated VSWR characteristics with various length of L_1 . As the gap distance between the T-shaped ring slot increases from 0.4 to 1.2 mm, the filter bandwidth is varied from 0.5 to 1.7 GHz. Therefore the bandwidth of notch frequency is controllable by changing the width of L_1.

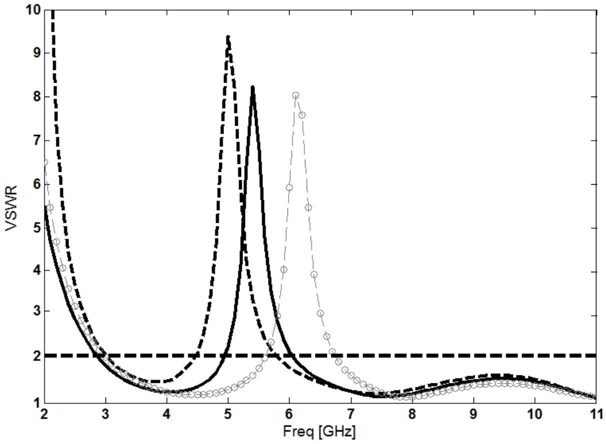

Fig. 6. Simulated VSWR characteristic with different values of W_1.

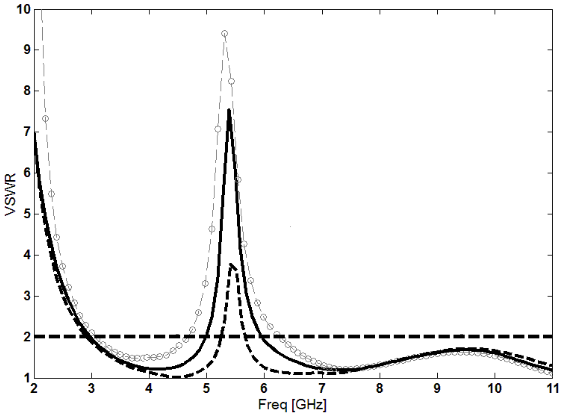

Fig. 7. Simulated VSWR characteristics for the proposed antenna with different values of L_1.

Figure 8 shows the measured and simulated VSWR characteristics of the proposed antenna. The fabricated antenna has the frequency band of 2.95 to over 15.65 GHz with a rejection band around 5.13 to 5.91 GHz. Also in order to clear show the resonance frequencies the measured and simulated return loss characteristics of the proposed antenna shown in Fig. 9. As shown in Figs. 8 and 9, there exists a discrepancy between measured data and the simulated results this could be due to the effect of the SMA port, and also the accuracy of the simulation due to the wide range of simulation frequencies. In order to confirm the accurate return loss characteristics for the designed antenna, it is recommended that the manufacturing and measurement process need to be performed carefully.

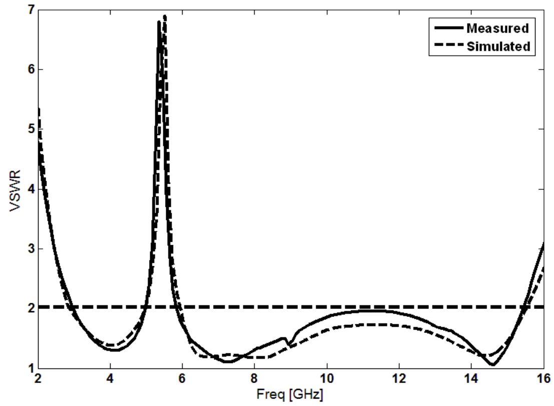

Fig. 8. Measured and simulated VSWR for the proposed antenna.

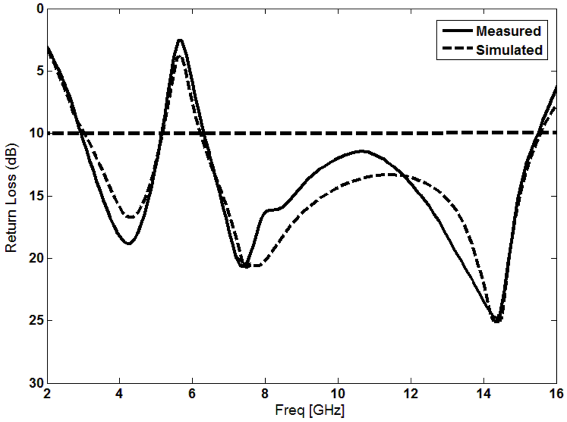

Fig. 9. Measured and simulated return loss characteristics for the proposed antenna.

Figure 10 shows the measured radiation patterns including the co-polarization and cross-polarization in the *H*-plane (*x-z* plane) and *E*-plane (*y-z* plane). It can be seen that the radiation patterns in *x-z* plane are nearly omnidirectional for the three frequencies.

Figure 11 shows the effects of the G-shaped slots and a T-shaped ring slot on the maximum gain in comparison to the ordinary square antenna without them. As shown in Fig. 11, the ordinary square antenna has a gain that is low at 3 GHz and increases with frequency. It is found that the gain of the square antenna is decreased with the use of the G-shaped slots in the ground plane and the T-shaped ring slot the square radiating patch of the antenna. It can be observed in Fig. 11 that by using these structures, a sharp decrease of maximum gain in the notched frequency band at 5.5 GHz is shown. For other frequencies outside the notched frequencies band, the antenna gain with the filter is similar to those without it.

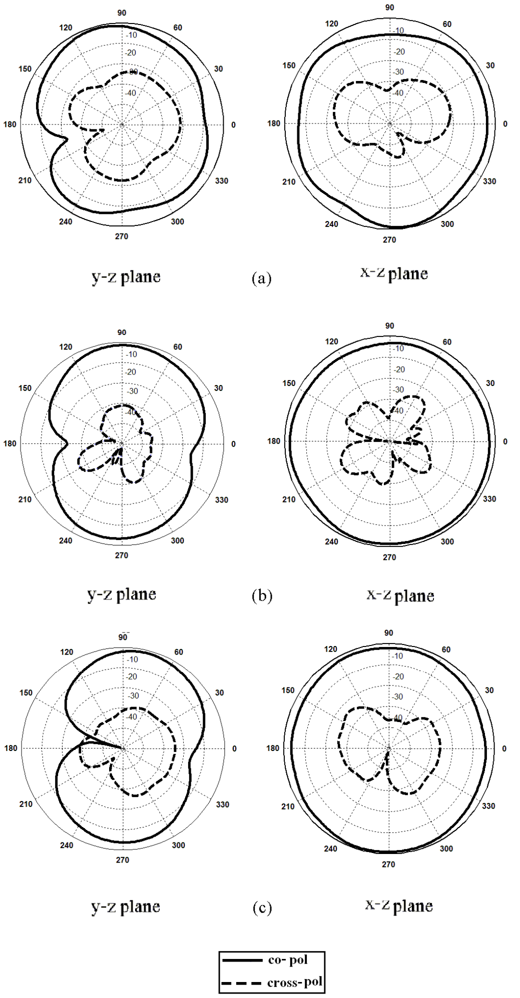

Fig. 10. Measured radiation patterns of the proposed antenna. (a) 4GHz, (b) 7 GHz, and (c) 10 GHz.

V. CONCLUSION

In this paper, a novel small square slot antenna with variable band-stop characteristic for UWB applications has been proposed. In this design, the proposed antenna can operate from 2.95 to 15.65 GHz with VSWR < 2 with a rejection band around 5.13 to 5.91 GHz. and unlike other antennas reported in the literature to date, the proposed antenna displays a good omni-directional radiation pattern even at higher frequencies. Good return loss and radiation pattern characteristics are obtained in the frequency band of interest. The designed antenna has a small size. Simulated and experimental results show that the proposed antenna could be a good candidate for UWB application.

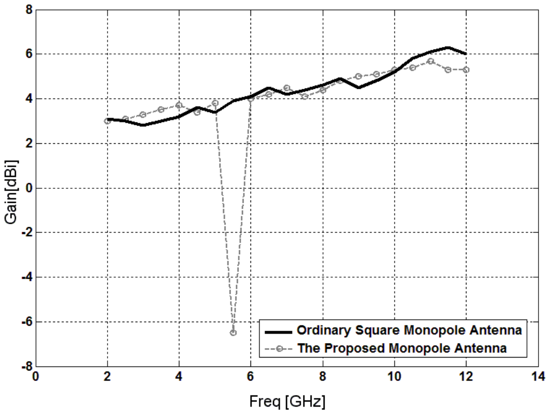

Fig. 11. Maximum gain comparisons for the ordinary square antenna (simulated), and the proposed antenna (measured).

ACKNOWLEDGMENT

The authors are thankful to Microwave Technology (MWT) Company staff for their beneficial and professional help (www.microwave-technology.com).

REFERENCES

[1] Schantz H., The Art and Science of Ultra wideband antennas, Artech House 2005.

[2] M. Ojaroudi, Sh. Yzdanifard, N. Ojaroudi, and M. Nasser-Moghaddasi, "Small Square Monopole Antenna with Enhanced by Using Inverted T-Shaped Slot and Conductor-Backed Plane", *IEEE Transactions on Antenna and Propagation*, vol. 59, no. 2, pp. 670-674, February 2011.

[3] R. Azim, M. T. Islam, N. Misran, "Design of a Planar UWB Antenna with New Band Enhancement Technique," *Applied Computational Electromagnetics Society (ACES) Journal*, vol. 26, no. 10, pp. 856-862, October 2011.

[4] D. S. Javan, O. H. Ghouchani, "Cross Slot Antenna with U-Shaped Tuning Stub for Ultra Wideband Applications," *Applied Computational Electromagnetics Society (ACES) Journal*, vol. 24, no. 4, pp. 427-432, August 2009.

[5] D. S. Javan, O. H. Ghouchani, "Cross Slot Antenna with U-Shaped Tuning Stub for Ultra Wideband Applications," *Applied Computational Electromagnetics Society (ACES) Journal*, vol. 24, no. 4, pp. 427-432, August 2009.

[6] M. Ojaroudi, Gh. Ghanbari, N. Ojaroudi, and Ch. Ghobadi, "Small Square Monopole Antenna for UWB Applications with Variable Frequency Band-Notch Function," *IEEE Antennas and Wireless Propagation Letters*, vol. 8, pp. 1061-1064, 2009.

[7] R. Rouhi, Ch. Ghobadi, J. Nourinia and M. Ojaroudi, "Ultra-Wideband Small Square Monopole Antenna with Band Notched Function, Accepted on *Microwave and Optical Tech. Letters*, vol. 52, no. 9, pp. 2065-2069, September 2010.

[8] J. William, R. Nakkeeran, "A New UWB Slot Antenna with Rejection of WiMax and WLAN Bands," *Applied Computational Electromagnetics Society (ACES) Journal*, vol. 25, no. 9, pp. 787-793, September 2010.

[9] M. Naghshvarian-Jahromi, N. Komjani-Barchloui, "Analysis of the Behavior of Sierpinski Carpet Monopole Antenna," *Applied Computational Electromagnetics Society (ACES) Journal*, vol. 24, no. 1, pp. 32-36, February 2009.

[10] Ansoft High Frequency Structure Simulation (HFSS), Ver. 13, Ansoft Corporation, 2010.

Mohammad-Taghi Partovi was born on 1973 in Mianeh Iran. He received his B.Sc. degree in Control Engineering from University of Science and Technology, and M.Sc. degree in Industrial Engineering from University of Science and Technology, Mazandaran, Iran. Since March 2001, he has been a Research Fellow and a Teaching Assistant with the Department of Electrical Engineering, Aeronautical University of Science and Technology, Tehran, Iran. His research interests include design and modeling of microwave structures, radar systems, and RFID systems.

Nasser Ojaroudi was born on 1986 in Germi, Iran. He received his B.Sc. degree in Electrical Engineering from Azad University, Ardabil Branch. From 2011, he is working toward the M.Sc. degree in Telecommunication Engineering at Shahid Rajaee Teacher Training University. Since March 2008, he has been a Research Fellow in the Microwave Technology Company (MWT), Tehran, Iran. His research interests include monopole antenna, slot antennas, microstrip antennas for radar systems, ultra-wideband (UWB) and small antennas for wireless communications, microwave passive devices and circuits, and microwave/millimeter systems.

Mohammad Ojaroudi was born on 1984 in Germi, Iran. He received his B.Sc. degree in Electrical Engineering from Azad University, Ardabil Branch and M.Sc. degree in Telecommunication Engineering from Urmia University. From 2010, he is working toward the Ph.D. degree at Shahid Beheshti University. From 2007 until now, he is an Teaching Assistant with the Department of Electrical Engineering, Islamic Azad University, Ardabil Branch, Iran. Since March 2008, he has been a Research Fellow (Chief Executive Officer) in the Microwave Technology Company (MWT), Tehran, Iran. His research interests include analysis and design of microstrip antennas, design and modeling of microwave structures, radar systems, and electromagnetic theory. He is author and coauthor of more than 80 journal and international conference papers.

Noradin Ghadimi was born in ardabil-Iran in 1985, and received the B.Sc. degree in electrical engineering from the Islamic Azad University, Ardabil Branch, Ardabil, Iran, in 2009 and the M.Sc. degree in electrical engineering from the Islamic Azad University Ahar Branch, Ahar, Iran, in 2011.
His research interests include Power System Protection, modeling and analysis of Distributed Generations, renewable energy and communications systems.

A Novel Compact UWB Antenna with Triple Band-Notches for WiMAX/ WLAN/ ITU Bands

M. M. Abdollahi [1], H. R. Dalili Oskouei [2], M. Akbari [1], and M. Mighani [2]

[1] Faculty of Eng., Department of Electrical Engineering
Urmia University, Urmia, Iran
farhood_abdollahi@yahoo.com, akbari.telecom@gmail.com

[2] Faculty of Eng., Department of Electrical Engineering
Aeronautical University, Tehran, Iran
h_oskouei@yahoo.com, mojtaba.mighani@gmail.com

Abstract — A novel compact Ultra-Wideband (UWB) antenna with triple band-notched characteristics is presented. The antenna patch consists of several circular rings and a small circle. The antenna has a compact size of 25 × 20 mm^2, which has been printed on a Rogers RO4003 substrate. Moreover, the proposed antenna has been successfully fabricated and measured, showing broadband matched impedance (2.8 up to more than 20GHz, VSWR$\leq$ 2); almost stable gain and good omnidirectional radiation patterns.

Index Terms — Triple Band-Notches, Ultra Wideband (UWB), WiMAX, WLAN, ITU, microstrip antenna.

I. INTRODUCTION

After allocation of the frequency band of 3.1-10.6 GHz (UWB) for commercial that is used by the FCC (Federal Communication Commission) [1], Ultra Wideband systems have received phenomenal gravitation in wireless communication. The UWB technology provides promising solutions for the future communication systems because of different advantages such as small emission power, low cost for short range access and remote sensing applications, high data rate and large bandwidth. On the other hand, the frequency range for UWB systems will cause interference with existing narrow band wireless communication systems. For instance, The wireless local area network (WLAN) for IEEE 802.11a operating at 5.15-5.35 and 5.725-5.825 GHz, the Worldwide Interoperability for microwave access (WiMAX) for IEEE 802.16 operating at 3.4-3.69, 5.25-5.85 GHz, and ITU Band (8.025-8.4 GHz). Therefore, UWB antennas with band-notched characteristics to filter the potential interference are desirable. Nowadays, many UWB antennas without and with various band-notched properties have developed [2-12]. The proposed antenna can be used in UWB systems which need no filters to suppress dispensable bands. The both Ansoft High Frequency Simulation Structure (HFSS) [13] and computer Simulation Technology (CST) [14] Three-dimensional (3-D) electromagnetic EM simulators are used to optimize the presented design. The proposed antenna with three tuneable narrow notched bands, which capability of its increasing exists, is proposed. The triple-band notch was successfully implemented and the simulated results show reasonable agreement with the measured results. Rest of the paper describes the antenna design in Section II, discussions on results is presented in Section III and followed by conclusive comments and further scope in Section IV.

II. ANTENNA DESIGN

The geometry of the proposed CPW-fed antenna for UWB applications is depicted in Fig. 1; also the optimized values of parameters are listed in Table 1.

Submitted On: May 6, 2012
Accepted On: Nov. 8, 2012

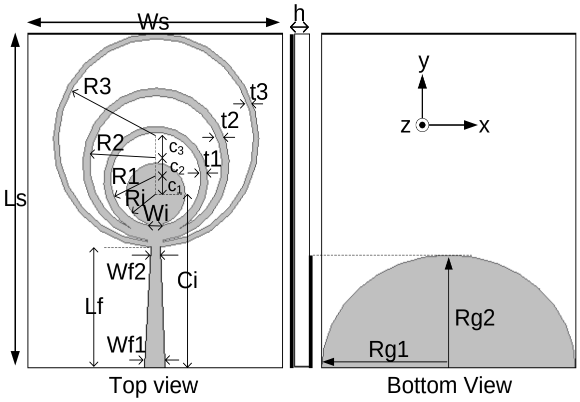

Fig. 1. Geometry of the proposed antenna.

Table 1: Optimal parameter values of the antenna and scale of the parameters (mm)

L_S	W_S	L_f	W_{f1}	W_{f2}	W_i	C_i
25	20	9	1.6	0.7	1.2	13
C_1	C_2	C_3	R_i	R_1	R_2	R_3
1.1	1.1	1.8	2.3	3.5	5.2	7.8
t_1	t_2	t_3	R_{g1}	R_{g2}	ε_r	h
0.5	0.5	0.2	9.9	8.5	3.55	0.8

The antenna is printed on a 25 × 20 mm^2 Rogers RO4003 substrate with relative permittivity 3.55, thickness 0.8mm, and loss tangent 0.0027. The antenna consists of three rings with radiuses R_1, R_2, R_3 and thicknesses of t_1, t_2, t_3 respectively, a small circle with radius R_i in front of the side, and one nearly semicircular ground on the back side. Besides, the antenna feed line is in the form of trapezium with parameters W_{f1}, W_{f2}, and L_f which is connected to a SMA connector 50Ω from Gigalane company with part number of PSF-S02 Series1. Presentation of a novel technique to obtain the controllable notches is the most advantage of the antenna. By enhancing the number of circular rings, the number of notched bands can be easily increased. Figure 2 exhibits Photograph of the fabricated antenna.

The next section is about the antenna design process and the effect of various parameters on VSWR.

III. ANTENNA PERFORMANCE AND DISCUSSION

In this section, the design procedure of the triple band-notches antenna by VSWR curves is demonstrated. Note that the simulated results are obtained using the HFSS and CST software's.

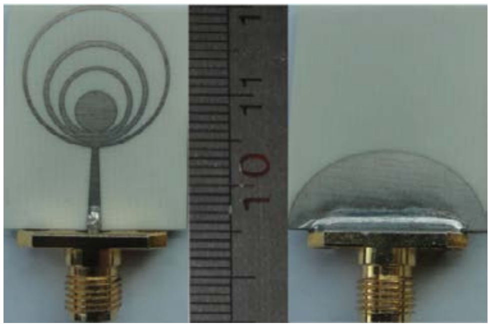

Fig. 2. Photograph of the fabricated antenna and scale of the ruler (cm).

A. Full-Band Design

The main reference or primary shape of the triple band-notches antenna was in the form of circular monopole with radius R_3+t_3 which is shown in Fig. 3.

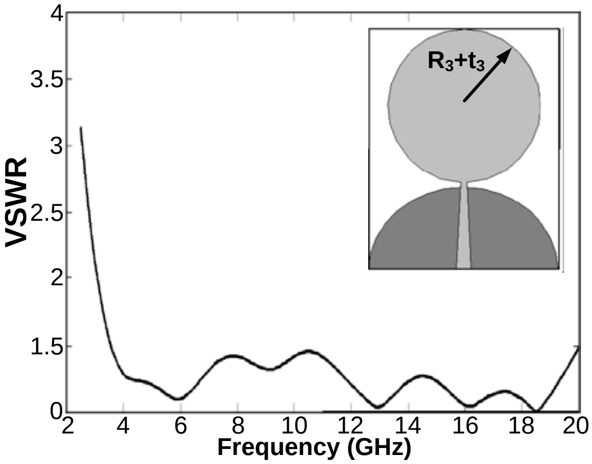

Fig. 3. Simulated VSWR of the referenced antenna.

Also, in this Figure VSWR can be seen in a way that the bandwidth for VSWR ≤ 2 is from 3.1 up to more than 20 GHz. Meanwhile, structure of the ground and feed line are similar to the proposed antenna structure.

B. Triple band-notches Design

In this section, the design procedure of the notches and the effect of varying the major parameters on lower, middle, and finally upper notched band are examined. The main idea of the proposed antenna has come from [2-3].The Proposed antenna has plenty of benefits related to these references. According to it, size of the proposed antenna has been fallen 74% and 44% related to [2], [3] respectively. It is also noticeable that bandwidth of the proposed antenna has been risen 20% and 50% related to [2], [3] in order. The last advantage of the antenna is three notches that in both of the references is a notch. At first, the effect of varying radius R_3 on VSWR for three cases is studied. Figures 4a to 4c illustrate the effect of varying radius R_3 on VSWR in the form of a notch (a), two notches (b), and three notches (c) respectively. From Figs. 4 can be concluded parameter R_3 which has an independent effect on lower notched band. On the other hand, other notches have not major effect on the first notched band and this subject makes easy design of the antenna. As previously expected, by increasing radius R_3 the notched-band frequency is decreased and vice versa. Last point in Figs. 4 is related to amount of frequency shift in a way that for Fig. 4a, in case of one notch, by varying R_3 frequency shift is more than 1GHz, while in Figs. 4b and 4c is not same. The best value to filter WiMAX band interference, 3.4 up to 3.69 GHz, is 7.8 mm.

In Fig. 5 the design procedure of notch on middle band in two cases (a), and (b) has been exhibited. As shown in Fig. 5, it is found that the second notch on middle band is independent from other notches; it means that by varying R2 the second notch is just shifted, while other notches on lower and upper band are constant. Amount of frequency shift for proposed antenna in case (b) is more than case (a). The desired value to filter WLAN and WiMAX bands interference, 5.15 up to 5.85 GHz, is 5.2mm.

Figure 6 exhibits VSWR for different values of R_1. The best value R_1 to filter ITU band interference, 8.025-8.4 GHz, is 3.5mm. The proposed antenna has been implemented based on the dimensions presented in Table I. The VSWR of the proposed antenna has been measured using an Agilent E8362B network analyzer in its full operational span (10 MHz-20 GHz). The simulated and measured VSWR of the fabricated antenna are depicted in Fig. 7.

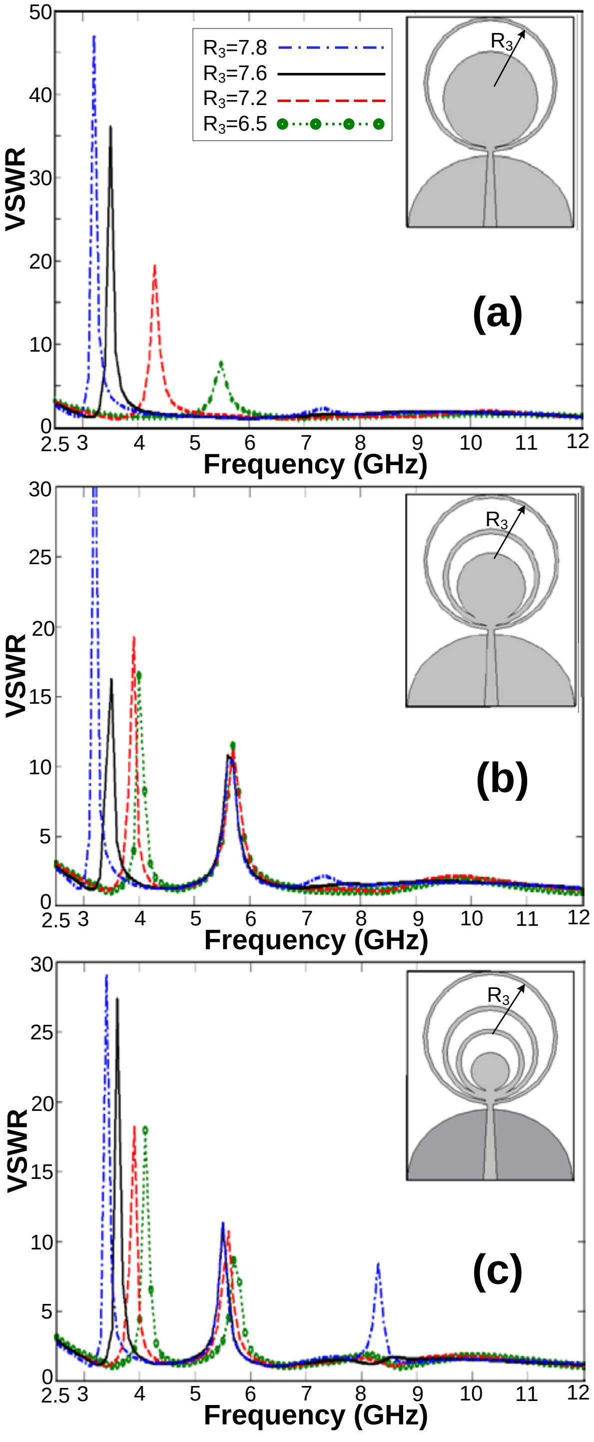

Fig. 4. The design procedure of the notch on lower band and Simulated VSWRs for different values of R_3 in three cases (a), (b) and (c).

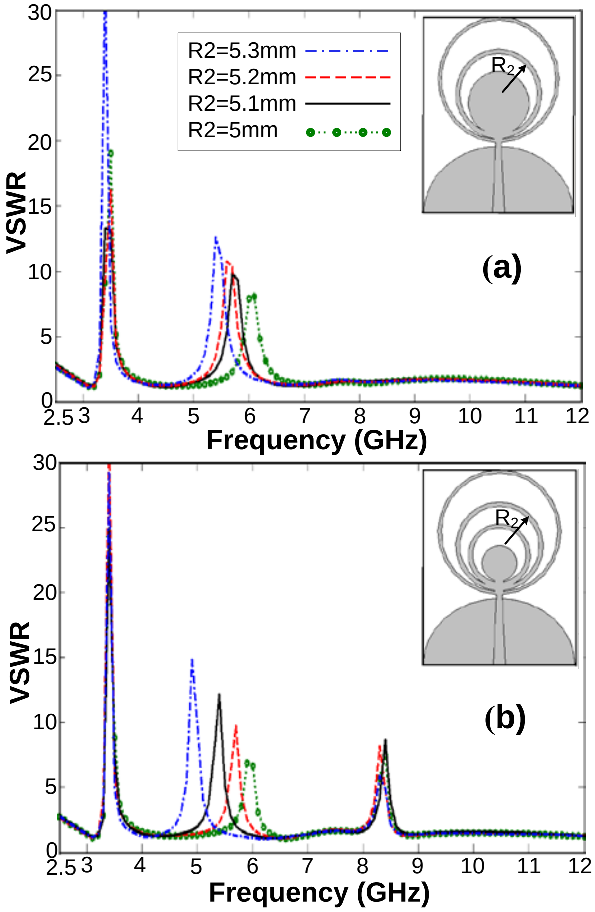

Fig. 5. The design procedure of notch on middle band and Simulated VSWRs for different values of R_2 in two cases (a), and (b).

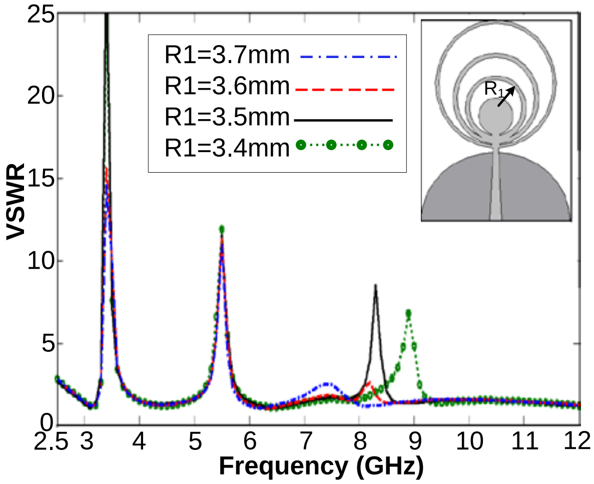

Fig. 6. Simulated VSWR for different values of R_1.

Moreover, Fig. 7 to compare the VSWR results between the proposed antenna and referenced circular monopole antenna has been presented. This point should be again repeated which each circular ring corresponds to a notch. It can be observed that the antenna has a wideband performance of 3.05 to more than 20GHz for VSWR≤ 1.7. Besides, the impedance bandwidth consists of three notched bands of 3.26-3.76, 5.14-5.87, and 8-8.5 GHz. It is apparent that the presented antenna can be used for higher frequencies above the FCC band. This behavior almost was predicted from HFSS based on the finite element method (FEM). Good agreement between simulated and measured results is observed and a bit difference between them is attributed to factors such as inappropriate quality of the microwave substrate effects, fabrication imperfections, and SMA connector.

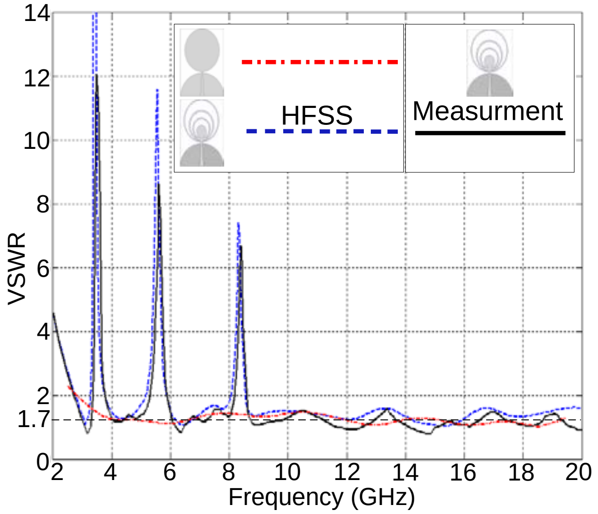

Fig. 7. Measured and simulated VSWRs of the proposed antenna.

C. Time-Domain Analysis

In this portion, more is used from CST software to analyse the antenna in time domain. In UWB systems, the information is transmitted using short pulses. Hence, it is important to study the temporal behavior of the transmitted pulse. The communication system for UWB pulse transmission must limit distortion, spreading and disturbance as much as possible. Group delay is an important parameter in UWB communication, which represents the degree of distortion of pulse signal. The key in UWB antenna design is to obtain a good linearity of the phase of the radiated field because the antenna should be able to transmit the electrical pulse with minimal distortion. The group delay is usually used to evaluate the phase response of the transfer function because it is defined as the rate of change of the total phase shift with respect to angular frequency. Ideally, when the phase response is strictly linear, the group delay is constant.

$$\text{group delay} = -\frac{d\theta(w)}{dw} \qquad (1)$$

As depicted from Fig. 8, the group delay variation is less than 1ns over the frequency band without notched bands which ensure us pulse transmitted or received by the antenna will not distort seriously and will retain its shape.

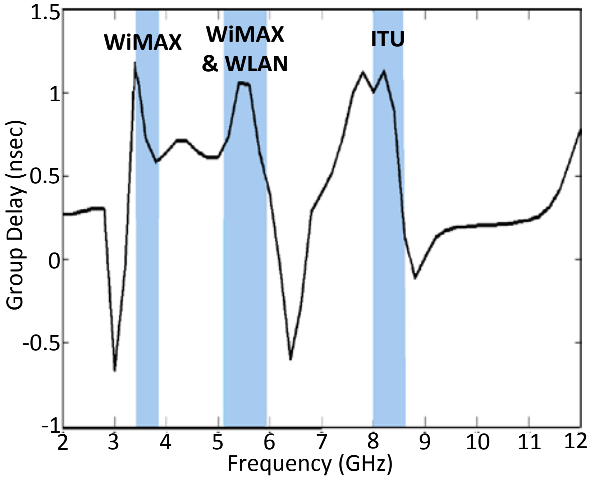

Fig. 8. Simulated group delay versus frequency for the proposed antenna.

As expected before, the groups delay variation at notches from 3.4-3.69GHz, 5.15-5.85GHz, and 8.025-8.4 GHz for WiMAX, WLAN, and ITU bands with respect to other frequencies is much. In spite of it, therefore, the proposed antenna is suitable for modern UWB communication systems. Transient response of the antenna is studied by modeling the antenna by its transfer function. The transmission coefficient S_{21} was simulated in the frequency domain for the face-to-face orientation. Figure 9 shows the magnitude of measured S_{21} for the face-to-face and side by side orientations. As it is apparent, S_{21} plot is almost flat with variation less than 15dB in the operating band. The reason of three tangible resonances in S_{21} plot is due to three notches WiMAX, WLAN, and ITU bands.

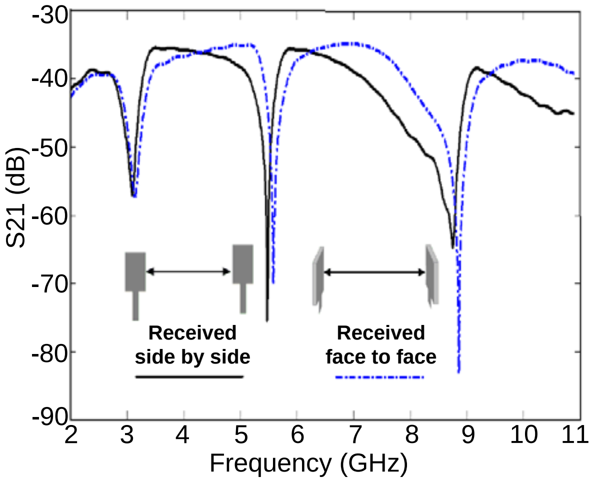

Fig. 9. Simulated S_{21} with a pair of identical antennas for face to face and side by side orientations.

Phase of S_{21} the face to face and side by side orientations has been plotted, also and is shown in the Fig. 10. As previously expected, the plot shows a linear variation of phase in the total operating band except notched bands.

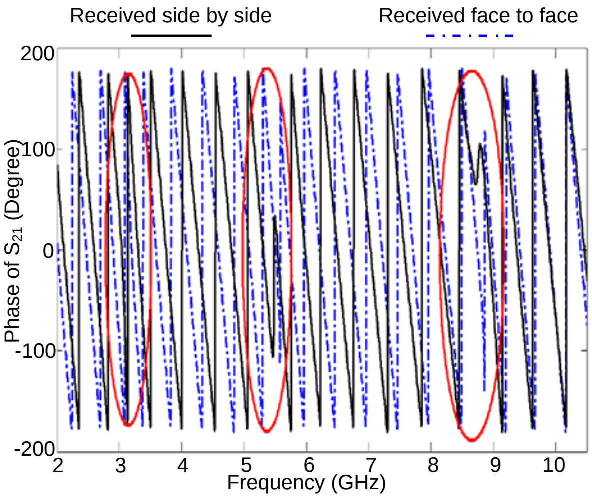

Fig. 10. Simulated Phase of S_{21} for face to face and side by side orientations.

The transfer function is transformed to time domain by performing the inverse Fourier transform. Fourth derivative of a Gaussian function is selected as the transmitted pulse.

Therefore the output waveform at the receiving antenna terminal can be expressed by convoluting the input signal and the transfer function. The input and received wave forms for the face-to-face and side-by-side orientations of the antenna are shown in Fig. 11.

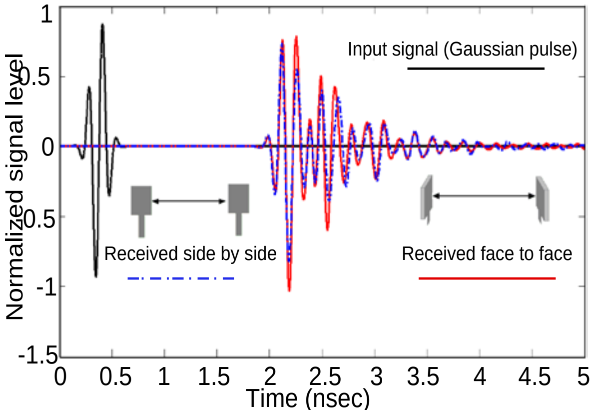

Fig. 11. Simulated transmitted and received pulses by the simulator CST.

It can be seen that the shape of the pulse is preserved in all the cases. Only due to being three notches, there is a bit distortion on received pulses which it was predictable. Using the reference and received signals, it becomes possible to quantify the level of similarity between signals. In telecommunication systems, the correlation between the transmitted (TX) and received (RX) signals is evaluated using the fidelity factor (1)

$$F = max_{\tau}\left|\frac{\int_{-\infty}^{+\infty} S(t)r(t-\tau)dt}{\sqrt{\int_{-\infty}^{+\infty} S(t)^2 \cdot \int_{-\infty}^{+\infty} r(t)^2\, dt}}\right| \qquad (2)$$

Where S(t) and r(t) are the TX and RX signals, respectively. For impulse radio in UWB communications, it is necessary to have a high degree of correlation between the TX and RX signals to avoid losing the modulated information. However for most other telecommunication systems, the fidelity parameter is not that relevant. In order to evaluate the pulse transmission characteristics of the proposed UWB antenna with triple band-notches, two configurations (side-by-side and face-to-face orientations) were chosen. The transmitting and receiving antennas were placed in a d=0.5 m distance from each other. As shown in Fig. 11, although the received pulses in each of two orientations are broadened, a relatively good similarity exists between the RX and TX pulses. Using (1), the fidelity factor for the face-to-face and side-by-side configurations were obtained equal to 0.72 and 0.7, respectively. Values the fidelity factor show that the antenna imposes negligible effects on the transmitted pulses. The pulse transmission results are obtained using CST.

D. Radiation Characteristics

The y-z plane and the x-z plane are selected to show the antenna radiation patterns referred to as E-plane and H-plane, respectively. Figure 12 illustrates the antenna normalized radiation pattern at E-plane and H-plane at 4.2, 7, and 9 GHz.

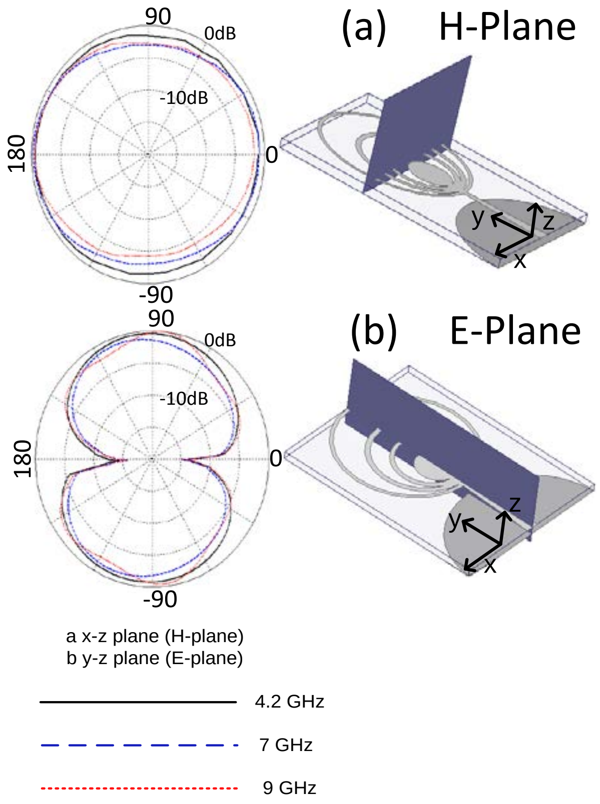

Fig. 12. Measured normalized radiation pattern of the antenna.

It can be seen that the antenna has a nearly omni-directional radiation pattern in the H-plane and a dipole-like radiation pattern in the E-plane in the very wide frequency band. Figure 13 exhibits the measured gain of the antenna. It is quite clear that the antenna gain decreases down to -4 dBi at three WLAN, WiMAX, and ITU bands indicating the effect of the notched bands clearly.

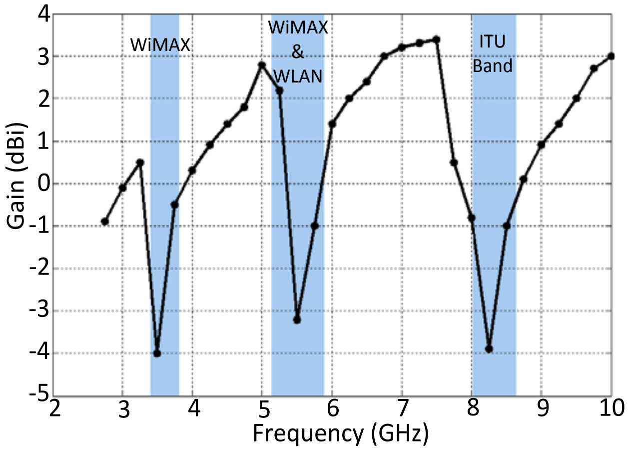

Fig. 13. Measured gain versus frequency for the proposed antenna.

IV. CONCLUSION

A novel compact UWB printed monopole antenna with triple notched bands has been proposed. Three band-notching structures, including three circular rings, are exploited to obtain the aimed for rejection bands. By enhancing the number of circular rings, the number of notched bands can be increased easily. In addition, by changing the thickness of rings, the bandwidth of notched bands can be tuned. Moreover, sufficient bandwidth and good monopole-like radiation patterns are observed.

REFERENCES

[1] Federal Communications Commission, First report and order on Ultra-Wideband technology, FCC 02-48, compact UWB planar antenna with band-notch characterization. Washington, DC, 22nd April, 2002.

[2] R. Kumar, “Design of Non-Concentric Circular UWB Fractal Antenna for Wireless Communication,” *Int. J. of Recent Trends in Engineering and Technology*, vol. 4, no. 3, p. 125ff, Nov 2010.

[3] Ayman A. R. Saad, Elsayed E. M. Khaled, and Deena A. Salem, “Novel Design of Proximity-fed Ultra-wide Band Annular Slot Antenna,” *Progress In Electromagnetics Research Symposium Proceedings*, Suzhou, China, p.1429ff, Sept. 12-16, 2011.

[4] Li, L., Zhou, Z.-L., Hong, J.-S., “Compact UWB Antenna with Four Band-Notches for UWB Applications,” *Electron. Lett.*, vol. 47, no. 22, pp. 1211-1212, 2011.

[5] Almalkawi, M.J., Devabhaktuni, V.K., “Quad Band-Notched UWB Antenna Compatible with WiMAX/INSAT/ Lower-Upper WLAN Applications,” *Electron. Lett.*, vol. 47, no. 19, pp. 1062-1063, 2011.

[6] Li, Y.S., Yang, X.D., Liu, C.Y., Jiang, T., “Compact CPW-fed Ultra-Wideband Antenna with Dual Band-Notched Characteristics,” *Electron. Lett.*, vol. 46, no. 14, pp. 967-968, 2010.

[7] Thomas, K.G., Sreenivasan, M., “Compact CPW-Fed Dual-Band Antenna,” *Electron. Lett.*, vol. 46, no. 1, pp.13-14, 2010.

[8] R. Azim, M. T. Islam, N. Misran, “Design of a Planar UWB Antenna with New Band Enhancement Technique,” *Applied Computational Electromagnetics Society (ACES) Journal*, vol. 26, no. 10, pp. 856-862, October 2011.

[9] J. William, R. Nakkeeran, “A New UWB Slot Antenna with Rejection of WiMax and WLAN Bands,” *Applied Computational Electromagnetics Society (ACES) Journal*, vol. 25, no. 9, pp. 787-793, September 2010.

[10] D. S. Javan, O. H. Ghouchani, “Cross Slot Antenna with U-Shaped Tuning Stub for Ultra Wideband Applications,” *Applied Computational Electromagnetics Society (ACES) Journal*, vol. 24, no. 4, pp. 427-432, August 2009.

[11] M. Naghshvarian-Jahromi, N. Komjani-Barchloui, “Analysis of the Behavior of Sierpinski Carpet Monopole Antenna,” *Applied Computational Electromagnetics Society (ACES) Journal*, vol. 24, no. 1, pp. 32-36, February 2009.

[12] M. Mighani, M. Akbari, and N. Felegari, “A Novel SWB Small Rhombic Microstrip Antenna with Parasitic Rectangle into Slot of the Feed Line,” *Applied Computational Electromagnetics Society (ACES) Journal*, vol. 27, no. 1, pp. 74-79, January 2012.

[13] Ansoft HFSS User’s manual, Ansoft Corporation, Beta Release 11.0, April 2007.

[14] CST Microwave studio, ver. 2008. Computer simulation technology, Framingham, MA, 2008.

Mohammad Mehdi Abdollahi was born in Shiraz, Iran 1985. He received his B.S. degree of Electronic Engineering from university of Tarbiat Moallem, Sabzevar, Iran and M.S. degree of communication engineering from the Urmia University, Iran. His primary research interests are in antenna design.

Hamid Reza Dalili Oskouei received his BSc and MSc degrees in electrical engineering from the University of Aeronautical Science & Technology and the Trabiat Modares University, Iran in 2002 and 2004, respectively. He obtained his PhD degree in electrical engineering from Trabiat Modares University, Tehran, Iran. He then joined the University of Aeronautical Science & Technology, Tehran, Iran, as an assistant professor in 2006, his research areas are Communication, Radar,Microwave component, Antenna and wave propagation. Dr. Oskouei has served as a reviewer for a number of journals and conferences.

Mohammad Akbari was born on February 3, 1983 in Tehran, Iran; He received his B.Sc. degree in Engineering-Telecommunication from University of Bahonar, Kerman, Iran, in 2007 and M.Sc. degrees in Electrical Engineering-Telecommunication from University of Urmia, Urmia, Iran, in 2011. His primary research interests are in antenna design, filters, and microwave components. Since 2011 He has taught courses in microwave engineering, antenna theory, and Fields & Waves, and electromagnetic in Aeronautical University, Tehran, Iran.

Mojtaba Mighani was born in Mashhad, Iran, in September 23, 1983. He received B.Sc. degree in Electrical and Electronic Engineering from Aeronautical University, Tehran, Iran, in 2005 and M.Sc. degrees in RF & microwave engineering from K.N.Toosi University of Technology, Tehran, Iran. He is currently working toward the PhD degree in communication Engineering. Since 2007 He has taught courses in communication circuits, microwave engineering, antenna theory, RADAR and Fields & Waves in Aeronautical University, Tehran, Iran. Also he is working in some projects in PMS & RAMTec co as project manager and RF designer. His research interests include antenna theory, microwave active circuits and RF communication links.

Band-Notched Small Monopole Antenna using Triple E-Shaped Structures for UWB Systems

N. Ojaroudi [1], Sh. Amiri [2], F. Geran [1], and M. Ojaroudi [3]

[1] Faculty of Electrical & Computer Engineering
Shahid Rajaee Teacher Training University, Tehran, Iran
n_ojaroudi@srttu.edu, geran_e@yahoo.com

[2] Scientific Member of Electrical Engineering Department
Iranian Research Organization for Science and Technology (IROST), Tehran, Iran
amiri@irost.org

[3] Young Research Group
Ardabil Branch, Islamic Azad University, Ardabil, Iran
m.ojaroudi@iauardabil.ac.ir

Abstract **─** In this letter, a novel ultra wideband monopole antenna with frequency band-stop performance is designed and manufactured. The proposed antenna consists of two E-shaped structures in the radiating patch with a rotated E-shaped slot in the ground plane. The rotated E-shaped slot increases the bandwidth that provides a wide usable fractional bandwidth of more than 110% (3.05-11.50 GHz). In order to create band-rejected function, we use an E-shaped structure in the radiating patch and also by inserting a rotated coupled E-shaped strip we can improve band-notched performance and a frequency notch band of 5.07–5.92 GHz has been achieved. Good return loss and radiation pattern characteristics are obtained in the frequency band of interest. Simulated and measured results are presented to validate the usefulness of the proposed antenna structure for UWB applications.

Index Terms **─** Band-Notched Function, E-Shaped Structure, Printed Monopole Antenna (PMA), Ultra-Wideband (UWB) Communications.

I. INTRODUCTION

Communication systems usually require smaller antenna size in order to meet the miniaturization requirements of radio-frequency (RF) units [1]. It is a well-known fact that planar monopole antennas present really appealing physical features such as simple structure, small size, and low cost. Due to all these interesting characteristics, planar monopole antennas are extremely attractive to be used in emerging UWB applications, and growing research activity is being focused on them. Consequently, a number of planar monopoles with different geometries have been experimentally characterized [2]-[5].

The frequency range for UWB systems between 3.1–10.6 GHz will cause interference to the existing wireless communication systems for example the wireless local area network (WLAN) for IEEE 802.11a operating in 5.15–5.35 GHz and 5.725–5.825 GHz bands, so the UWB antenna with a band-notched function is required. Lately to generate the frequency band-notched function, several modified planar antennas with band-stop characteristic have been reported [6]-[11]. In [6]-[9], different shapes of the slots (i.e., rectangular, square ring, W-shaped and folded trapezoid) are used to obtain the desired band-notched characteristics. Single and multiple [10] half-wavelength U-shaped to generate the frequency band-notched function, modified planar slits are embedded in the radiation patch to generate the single and multiple band-notched functions,

Submitted On: July 25, 2012
Accepted On: Oct. 24, 2012

respectively. In [11], band-stop function is achieved by using a T-shaped coupled parasitic element in the ground plane.

In this letter, a different method for designing a novel and compact microstrip-fed monopole antenna with band-notched characteristic for UWB applications has been presented. In the proposed antenna for bandwidth enhancement, we use a rotated E-shaped slot in the ground plane and by using two E-shaped structures with variable dimensions in the radiating patch a band-stop performance can be created. The presented monopole antenna has a small size of 12×18 mm^2.

II. ANTENNA DESIGN

The presented small monopole antenna fed by a microstrip line is shown in Fig. 1, which is printed on an FR4 substrate of thickness 1.6 mm, permittivity 4.4, and loss tangent 0.018. The basic monopole antenna structure consists of a square patch, a feed line, and a ground plane. The square patch has a width W. The patch is connected to a feed line of width W_f and length $L_f + L_{gnd}$. Width of the microstrip feed line is fixed at 2 mm, as shown in Fig. 1. On the other side of the substrate, a conducting ground plane of width and length is placed. The proposed antenna is connected to a 50Ω SMA connector for signal transmission.

In this study, based on defected ground structure (DGS), a rotated E-shaped slot in the ground plane is used to perturb an additional resonance at higher frequencies and increase the bandwidth [12]. Also, based on electromagnetic coupling theory (ECT), for generating band-stop performance we use two E-shaped structures in the radiating patch. In this structure, the coupled E-shaped strip is playing an important role in the band rejected characteristics of this antenna [13]. By inserting the coupled E-shaped strip, the desired high attenuation near the notch frequency can be produced.

The final values of proposed antenna design parameters are as follows: $W_{sub} = 12mm$, $L_{sub} = 18mm$, $h_{sub} = 1.6mm$, $W_f = 2mm$, $L_f = 3.5mm$, $W = 10mm$, $W_S = 4mm$, $L_s = 1.5mm$, $W_{S1} = 1.25mm$, $L_{S1} = 1mm$, $W_{S2} = 0.5mm$, $L_{S2} = 1.75mm$, $W_e = 1.5mm$, $L_e = 4.75mm$, $W_{e1} = 0.25mm$, $L_{e1} = 4.75mm$, $W_P = 6.5mm$, $L_P = 8mm$, $W_{P1} = 1.5mm$, $L_{P1} = 6mm$, $W_{P2} = 1.5mm$, $L_{P2} = 2mm$, $W_d = 1.2mm$, and $L_{gnd} = 3.5mm$.

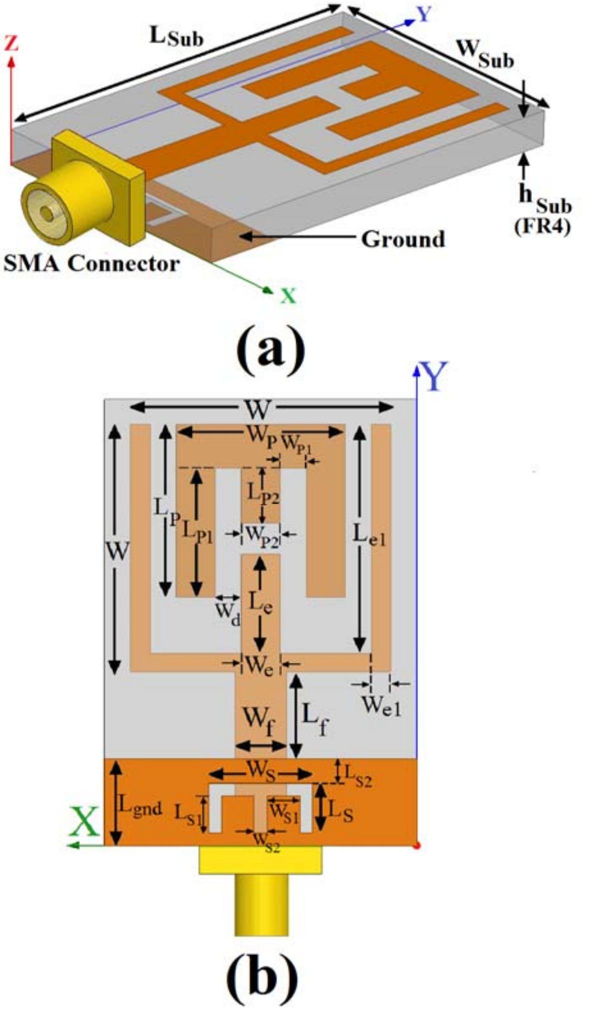

Fig. 1. Geometry of proposed slot antenna, (a) side view, (b) bottom view.

III. RESULTS AND DISCUSSIONS

The proposed microstrip Monopole antenna with various design parameters were constructed, and the numerical and experimental results of the input impedance and radiation characteristics are presented and discussed. The proposed microstrip-fed monopole antenna was fabricated and tested. The parameters of this proposed antenna are studied by changing one parameter at a time and fixing the others. The simulated results are obtained using the Ansoft simulation software high-frequency structure simulator (HFSS) [14]. The configuration of the presented monopole antenna was shown in Fig. 1. Geometry for the ordinary square antenna (Fig. 2(a)), with a rotated E-shaped slot in the ground plane (Fig. 2(b)), E-shaped antenna with a rotated E-shaped slot in the ground plane (Fig. 2(c)) and the proposed antenna (Fig. 2(d)) structures are compared in Fig. 2.

Return loss characteristics for the structures that were shown in Fig. 2 are compared in Fig. 3. As shown in Fig. 3, it is observed that the upper frequency bandwidth is affected by using the rotated E-shaped slot in the ground plane and the notched frequency bandwidth is sensitive to the coupled E-shaped strip on the radiating patch. Also the input impedance of the various monopole antenna structures that studied on Fig. 3, on a Smith Chart is shown in Fig. 4.

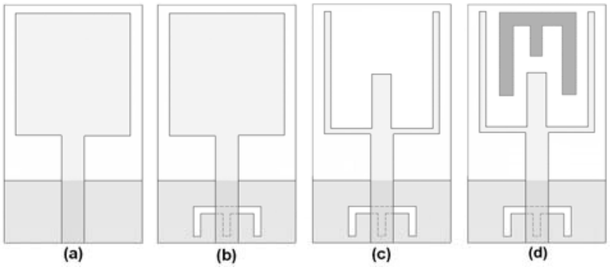

Fig. 2. (a) Ordinary square antenna, (b) with a rotated E-shaped slot in the ground plane, (c) E-shaped antenna with a rotated E-shaped slot in the ground plane, and (d) the proposed antenna structure.

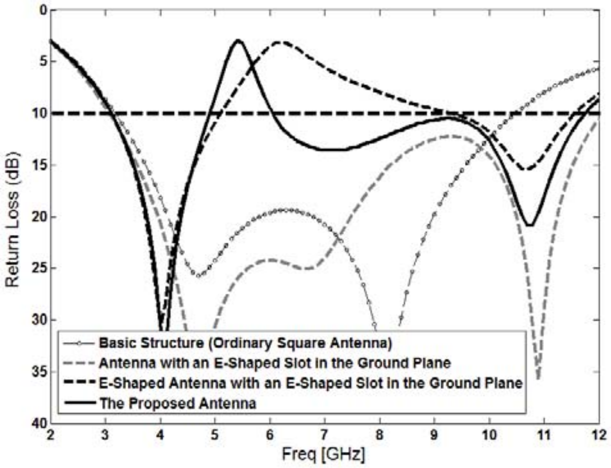

Fig. 3. Simulated return loss characteristics for the antennas shown in Fig. 2.

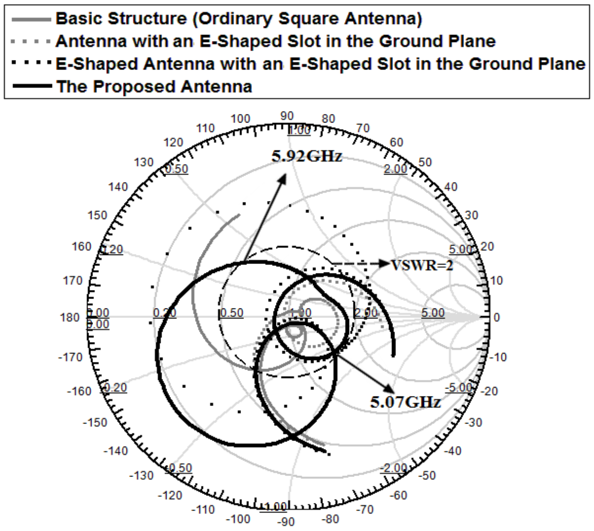

Fig. 4. The simulated input impedance on a Smith chart of the various monopole antennas structures shown in Fig. 2.

In order to understand the phenomenon behind this additional resonance performance, the simulated current distributions on the ground plane for the proposed antenna at 10.9 GHz are presented in Fig. 5(a). It is found by cutting a rotated E-shaped slot in the ground plane, third resonance at 10.9 GHz can be achieved.

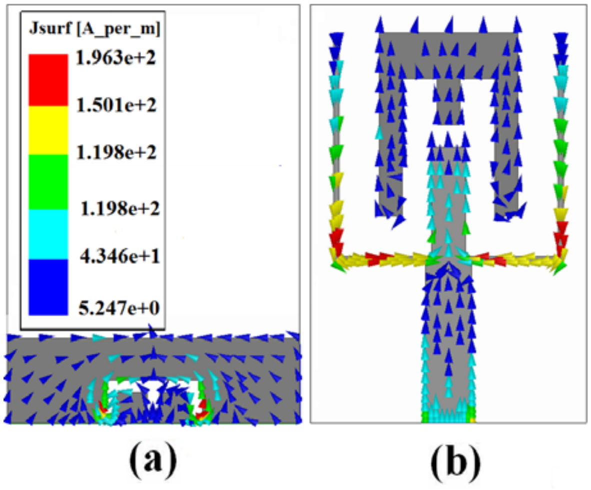

Fig. 5. Simulated surface current distributions for the proposed monopole antenna, (a) in the ground plane at 3.5 GHz, and (b) on the radiating patch at 5.5 GHz.

Other important design parameters of this structure are E-shaped structures on the radiating patch. Fig. 5(b) presents the simulated current distributions on the radiating patch at the notched frequency (5.5 GHz). As shown in Fig. 5(b), at the notched frequency the current flows are more dominant around of the E-shaped strip structures.

Figure 6 shows the simulated VSWR curves with different values of L_P. As shown in Fig. 6, when the exterior length of the coupled E-shaped strip increases from 5.5 to 9.5 mm, the center of notched frequency is decreases from 6.1 to 4.9 GHz. From these results, we can conclude that notched frequency is controllable by changing the exterior length of the coupled E-shaped strip.

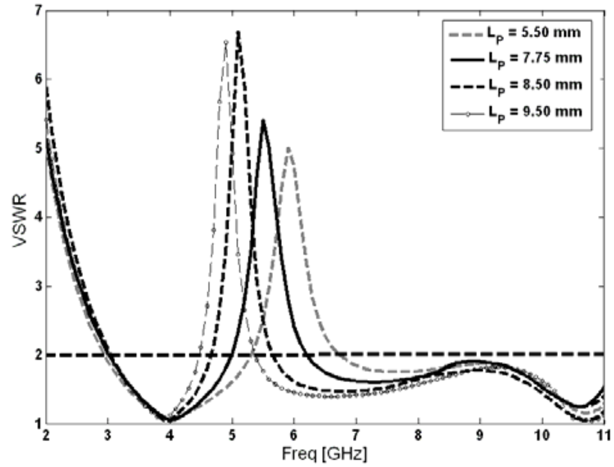

Fig. 6. Simulated VSWR characteristics for the proposed antenna with different values of L_P.

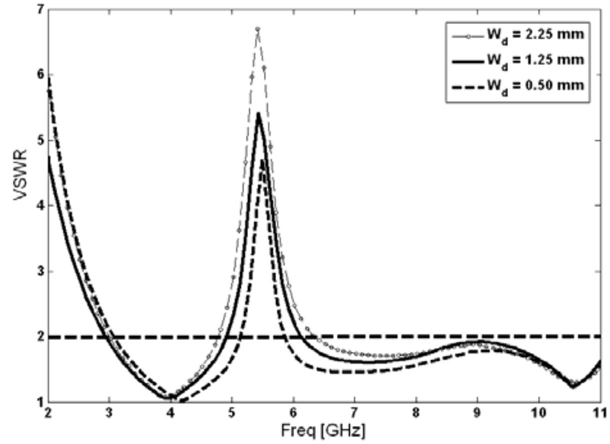

Fig. 7. Simulated VSWR characteristics for the proposed antenna with different values of W_d.

Another main effect of the coupled E-shaped strip occurs on the filter bandwidth. In this structure, the width of W_d is a critical parameter to control the filter bandwidth. Figure 7 illustrates the simulated VSWR characteristics with various length of W_d .When the width of W_d increases from 0.5 to 2.25 mm, the filter bandwidth is varied from 0.7 to 1.9 GHz. Therefore the bandwidth of notched frequency is controllable by changing the width of W_d.

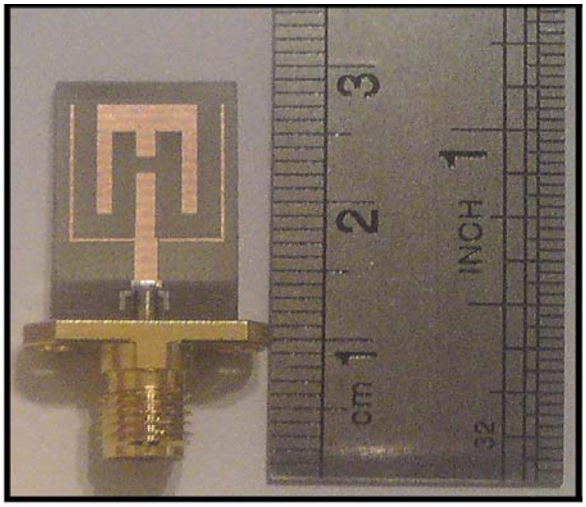

Fig. 8. Photograph of the realized printed monopole antenna.

The proposed antenna with final design, as shown in Fig. 8 was built and tested. Measured and simulated VSWR characteristics of the proposed antenna were shown in Fig. 9. The fabricated antenna has the frequency band of 3.05 to 11.5 GHz with a bad-stop function aroud of 5-6 GHz.

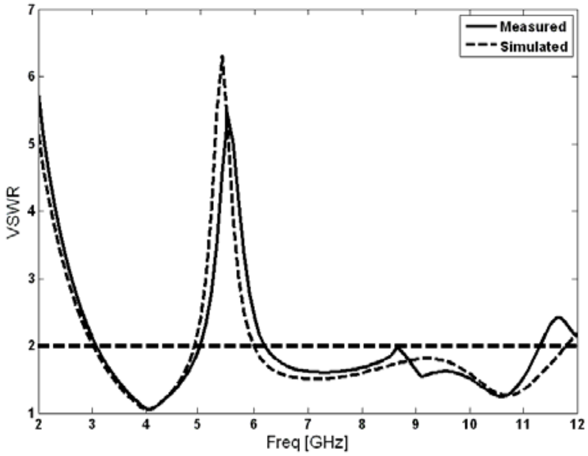

Fig. 9. Measured and simulated VSWR characteristics for the proposed antenna.

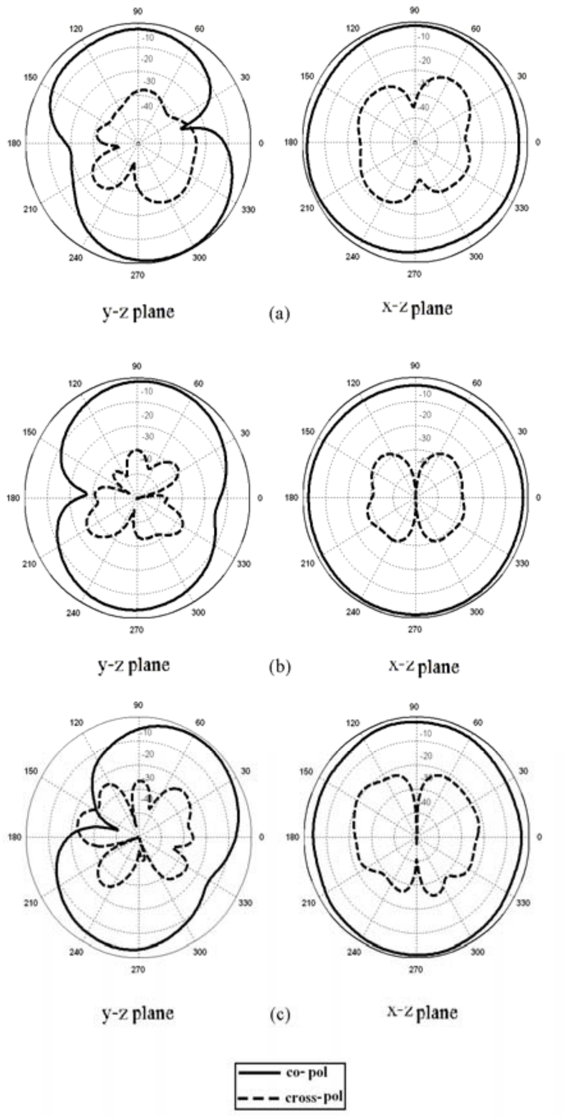

Fig. 10. Measured radiation patterns of the proposed antenna (a) 4 GHz, (b) 7 GHz, and (c) 10 GHz.

Figure 10 illustrates the measured radiation patterns, including co-polarization and cross-polarization in the H–plane (x-z plane) and E-plane (y-z plane). It can be seen that the radiation patterns in *x-z* plane are nearly omnidirectional for the three frequencies. The maximum gain of the proposed antenna was shown in Fig. 11. A sharp decrease of maximum gain in the notched frequency band at 5.5 GHz is shown in Fig. 11. For other frequencies outside the notched frequency band, the antenna gain with the filter is similar to those without it.

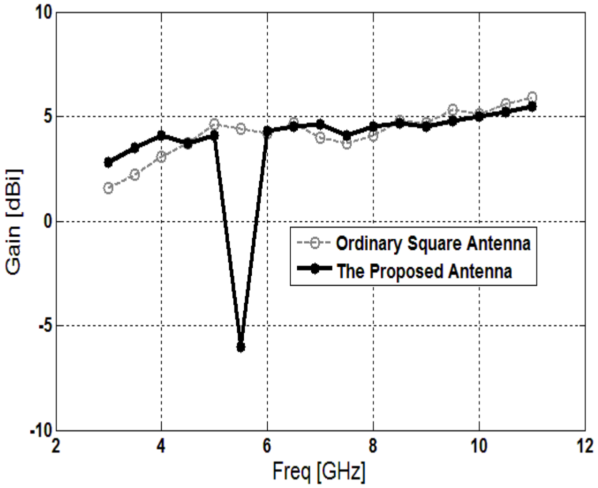

Fig. 11. Gain comparisons for the ordinary square antenna (simulated), and the proposed antenna (measured).

V. CONCLUSION

A new small printed monopole antenna (PMA) with band-notched function for UWB applications presented, in this paper. The proposed antenna can operate from 3.05 to 11.80 GHz with WLAN rejection band around 5.07–5.92 GHz. In order to enhance bandwidth, we cut a rotated E-shaped slot in the ground plane and also by using two E-shaped structures at the radiating patch a frequency band-notched function can be achieved and improved. The designed antenna has a small size of 12×18 mm^2. Simulated and experimental results show that the proposed antenna could be a good candidate for UWB applications.

ACKNOWLEDGMENT

The authors are thankful to Microwave Technology (MWT) company staff for their beneficial and professional help (www.microwave-technology.com).

REFERENCES

[1] H. Schantz, The art and science of ultra wideband antennas, Artech House, 2005.

[2] M. Ojaroudi, Sh. Yzdanifard, N. Ojaroudi, and M. Nasser-Moghaddasi, "Small Square Monopole Antenna with Enhanced by Using Inverted T-Shaped Slot and Conductor-Backed Plane", *IEEE Transactions on Antenna and Propagation*, vol. 59, no. 2, pp. 670-674, February 2011.

[3] R. Azim, M. T. Islam, N. Misran, "Design of a Planar UWB Antenna with New Band Enhancement Technique," *Applied Computational*

Electromagnetics Society (ACES) Journal, vol. 26, no. 10, pp. 856-862, October 2011.

[4] M. N.-Jahromi, N. K.-Barchloui, “Analysis of the Behavior of Sierpinski Carpet Monopole Antenna,” *Applied Computational Electromagnetics Society (ACES) Journal*, vol. 24, no. 1, pp. 32-36, February 2009.

[5] W. C. Weng, “Optimal Design of an Ultra-Wideband Antenna with the Irregular Shape on Radiator using Particle Swarm Optimization,” *Applied Computational Electromagnetics Society (ACES) Journal,* vol. 27, no. 5, pp. 427-434, May 2012.

[6] M. Ojaroudi, N. Ojaroudi, Y. Ebazadeh, “Dual Band-notch Small Square Monopole Antenna with Enhanced Bandwidth Characteristics for UWB Applications,” *Applied Computational Electromagnetics Society (ACES) Journal*, vol. 27, no. 5, pp. 420-426, May 2012.

[7] M. Ojaroudi, Sh. Yzdanifard, N. Ojaroudi, and R. A. Sadeghzadeh, " Band-Notched Small Square-Ring Antenna with a Pair of T-Shaped Strips Protruded Inside the Square Ring for UWB Applications”, *IEEE Antennas and Wireless Propagation Letters*, vol. 10, pp. 227-230, 2011.

[8] M. Ojaroudi, "Printed Monopole Antenna with a Novel Band-Notched Folded Trapezoid for Ultra-Wideband Applications", *Journal of Electromagnetic Waves and Application (JEMWA)*, vol. 23, pp. 2513–2522, 2009.

[9] Sh. Yazdanifard, R. A. Sadeghzadeh, and M. Ojaroudi, “UltraWideband Small Square Monopole Antenna with Variable Frequency Band-Notch Function", *Progress In Electromagnetic Research C*, vol. 15, pp. 133-144, 2010.

[10] M. Ojaroudi, Gh. Ghanbari, N. Ojaroudi, and Ch. Ghobadi, “Small Square Monopole Antenna for UWB Applications with Variable Frequency Band-Notch Function,” *IEEE Antennas and Wireless Propagation Letters*, vol. 8, pp. 1061-1064, 2009.

[11] R. Rouhi, Ch. Ghobadi, J. Nourinia and M. Ojaroudi, “Ultra-Wideband Small Square Monopole Antenna with Band Notched Function,” *Microwave and Optical Tech. Letters*, vol. 52, no. 8, August 2010.

[12] M. Mighani, M. Akbari, N. Felegari, “A CPW Dual Band Notched UWB Antenna,” *Applied Computational Electromagnetics Society (ACES) Journal*, vol. 27, no. 4, pp. 352-359, April 2012.

[13] G. Zhang, J. S. Hong, B. Z. Wang, G. Song, “Switched Band-notched UWB/ WLAN Monopole Antenna,” *Applied Computational Electromagnetics Society (ACES) Journal*, vol. 27, no. 3, pp. 256-260, March 2012.

[14] Ansoft High Frequency Structure Simulation (HFSS), ver. 13, Ansoft Corporation, 2010.

Nasser Ojaroudi was born on 1986 in Germi, Iran. He received his B.Sc. degree in Electrical Engineering from Azad University, Ardabil Branch. From 2011, he is working toward the M.Sc. degree in Telecommunication Engineering at Shahid Rajaee Teacher Training University. Since March 2008, he has been a Research Fellow in the microwave technology company (MWT), Tehran, Iran. His research interests include ultra-wideband (UWB) and small microstrip antennas for wireless communications, microwave passive devices and circuits, and microwave/millimeter systems.

Shervin Amiri was born in Tehran, Iran, in 1966. He received his B.Sc., M.Sc. and Ph.D. from Iran University of Science & Technology (IUST) in communication systems. Now he is a Scientific Member of Electrical Engineering Department in Iranian Research Organization for Science and Technology (IROST). His research interest fields are Antenna and RF subsystems in Microwave and mm-wave Bands and Radar systems. He is supervisor of many Ph.D. and M.Sc. students in the fields of communication system and subsystems.

Fatemeh Geran was born in Ghaemshar, Iran in 1977. She received her B.Sc. degree in Electrical Engineering (Telecommunication) from Tehran University, Tehran, Iran in 1999. Also, she received her M.Sc. and PHD degrees in Electrical Engineering (Telecommunication) from Tarbiat Modares University, Tehran, Iran, in 2003 and 2009, respectively. She is currently as an assistant Professor in Electrical Engineering at Shahid Rajaee Teacher training University, Tehran, Iran. Her research interest fields are Antenna and RF subsystems in Microwave and mm-wave Bands.

Mohammad Ojaroudi was born on 1984 in Germi, Iran. He received his B.Sc. degree in Electrical Engineering from Azad University, Ardabil Branch and M.Sc. degree in Telecommunication Engineering from Urmia University. From 2010, he is working toward the Ph.D. degree at Shahid Beheshti University. From 2007 until now, he is a Teaching Assistant with the Department of Electrical Engineering, Islamic Azad University, Ardabil Branch, Iran. Since March 2008, he has been a Research Fellow (Chief Executive Officer) in the microwave technology company (MWT), Tehran, Iran. His research interests include analysis and design of microstrip antennas, design and modeling of microwave structures, radar systems, and electromagnetic theory.

2012 INSTITUTIONAL MEMBERS

DTIC-OCP LIBRARY
8725 John J. Kingman Rd, Ste 0944
Fort Belvoir, VA 22060-6218

AUSTRALIAN DEFENCE LIBRARY
Northcott Drive
Canberra, A.C.T. 2600 Australia

BEIJING BOOK CO, INC
701 E Linden Avenue
Linden, NJ 07036-2495

DARTMOUTH COLLEGE
6025 Baker/Berry Library
Hanover, NH 03755-3560

DSTO EDINBURGH
AU/33851-AP, PO Box 830470
Birmingham, AL 35283

SIMEON J. EARL – BAE SYSTEMS
W432A, Warton Aerodome
Preston, Lancs., UK PR4 1AX

ENGINEERING INFORMATION, INC
PO Box 543
Amsterdam, Netherlands 1000 Am

ETSE TELECOMUNICACION
Biblioteca, Campus Lagoas
Vigo, 36200 Spain

GA INSTITUTE OF TECHNOLOGY
EBS-Lib Mail code 0900
74 Cherry Street
Atlanta, GA 30332

TIMOTHY HOLZHEIMER
Raytheon
PO Box 1044
Rockwall, TX 75087

HRL LABS, RESEARCH LIBRARY
3011 Malibu Canyon
Malibu, CA 90265

IEE INSPEC
Michael Faraday House
6 Hills Way
Stevenage, Herts UK SG1 2AY

INSTITUTE FOR SCIENTIFIC INFO.
Publication Processing Dept.
3501 Market St.
Philadelphia, PA 19104-3302

LIBRARY – DRDC OTTAWA
3701 Carling Avenue
Ottawa, Ontario, Canada K1A OZ4

LIBRARY of CONGRESS
Reg. Of Copyrights
Attn: 407 Deposits
Washington DC, 20559

LINDA HALL LIBRARY
5109 Cherry Street
Kansas City, MO 64110-2498

MISSOURI S&T
400 W 14th Street
Rolla, MO 56409

MIT LINCOLN LABORATORY
Periodicals Library
244 Wood Street
Lexington, MA 02420

NATIONAL CHI NAN UNIVERSITY
Lily Journal & Book Co, Ltd
20920 Glenbrook Drive
Walnut, CA 91789-3809

JOHN NORGARD
UCCS
20340 Pine Shadow Drive
Colorado Springs, CO 80908

OSAMA MOHAMMED
Florida International University
10555 W Flagler Street
Miami, FL 33174

NAVAL POSTGRADUATE SCHOOL
Attn:J. Rozdal/411 Dyer Rd./ Rm 111
Monterey, CA 93943-5101

NDL KAGAKU
C/0 KWE-ACCESS
PO Box 300613 (JFK A/P)
Jamaica, NY 11430-0613

OVIEDO LIBRARY
PO BOX 830679
Birmingham, AL 35283

DAVID PAULSEN
E3Compliance
1523 North Joe Wilson Road
Cedr Hill, TX 75104-1437

PENN STATE UNIVERSITY
126 Paterno Library
University Park, PA 16802-1808

DAVID J. PINION
1122 E Pike Street #1217
SEATTLE, WA 98122

KATHERINE SIAKAVARA
Gymnasiou 8
Thessaloniki, Greece 55236

SWETS INFORMATION SERVICES
160 Ninth Avenue, Suite A
Runnemede, NJ 08078

YUTAKA TANGE
Maizuru Natl College of Technology
234 Shiroya
Maizuru, Kyoto, Japan 625-8511

TIB & UNIV. BIB. HANNOVER
DE/5100/G1/0001
Welfengarten 1B
Hannover, Germany 30167

UEKAE
PO Box 830470
Birmingham, AL 35283

UNIV OF CENTRAL FLORIDA
4000 Central Florida Boulevard
Orlando, FL 32816-8005

UNIVERSITY OF COLORADO
1720 Pleasant Street, 184 UCB
Boulder, CO 80309-0184

UNIVERSITY OF KANSAS – WATSON
1425 Jayhawk Blvd 210S
Lawrence, KS 66045-7594

UNIVERSITY OF MISSISSIPPI
JD Williams Library
University, MS 38677-1848

UNIVERSITY LIBRARY/HKUST
Clear Water Bay Road
Kowloon, Honk Kong

CHUAN CHENG WANG
8F, No. 31, Lane 546
MingCheng 2nd Road, Zuoying Dist
Kaoshiung City, Taiwan 813

THOMAS WEILAND
TU Darmstadt
Schlossgartenstrasse 8
Darmstadt, Hessen, Germany 64289

STEVEN WEISS
US Army Research Lab
2800 Powder Mill Road
Adelphi, MD 20783

YOSHIHIDE YAMADA
NATIONAL DEFENSE ACADEMY
1-10-20 Hashirimizu
Yokosuka, Kanagawa,
Japan 239-8686

APPLIED COMPUTATIONAL ELECTROMAGNETICS SOCIETY JOURNAL
http://aces.ee.olemiss.edu

INFORMATION FOR AUTHORS

PUBLICATION CRITERIA

Each paper is required to manifest some relation to applied computational electromagnetics. **Papers may address general issues in applied computational electromagnetics, or they may focus on specific applications, techniques, codes, or computational issues.** While the following list is not exhaustive, each paper will generally relate to at least one of these areas:

1. **Code validation.** This is done using internal checks or experimental, analytical or other computational data. Measured data of potential utility to code validation efforts will also be considered for publication.

2. **Code performance analysis.** This usually involves identification of numerical accuracy or other limitations, solution convergence, numerical and physical modeling error, and parameter tradeoffs. However, it is also permissible to address issues such as ease-of-use, set-up time, run time, special outputs, or other special features.

3. **Computational studies of basic physics.** This involves using a code, algorithm, or computational technique to simulate reality in such a way that better, or new physical insight or understanding, is achieved.

4. **New computational techniques** or new applications for existing computational techniques or codes.

5. **"Tricks of the trade"** in selecting and applying codes and techniques.

6. **New codes, algorithms, code enhancement, and code fixes.** This category is self-explanatory, but includes significant changes to existing codes, such as applicability extensions, algorithm optimization, problem correction, limitation removal, or other performance improvement. **Note: Code (or algorithm) capability descriptions are not acceptable, unless they contain sufficient technical material to justify consideration.**

7. **Code input/output issues.** This normally involves innovations in input (such as input geometry standardization, automatic mesh generation, or computer-aided design) or in output (whether it be tabular, graphical, statistical, Fourier-transformed, or otherwise signal-processed). Material dealing with input/output database management, output interpretation, or other input/output issues will also be considered for publication.

8. **Computer hardware issues.** This is the category for analysis of hardware capabilities and limitations of various types of electromagnetics computational requirements. Vector and parallel computational techniques and implementation are of particular interest.

Applications of interest include, but are not limited to, antennas (and their electromagnetic environments), networks, static fields, radar cross section, inverse scattering, shielding, radiation hazards, biological effects, biomedical applications, electromagnetic pulse (EMP), electromagnetic interference (EMI), electromagnetic compatibility (EMC), power transmission, charge transport, dielectric, magnetic and nonlinear materials, microwave components, MEMS, RFID, and MMIC technologies, remote sensing and geometrical and physical optics, radar and communications systems, sensors, fiber optics, plasmas, particle accelerators, generators and motors, electromagnetic wave propagation, non-destructive evaluation, eddy currents, and inverse scattering.

Techniques of interest include but not limited to frequency-domain and time-domain techniques, integral equation and differential equation techniques, diffraction theories, physical and geometrical optics, method of moments, finite differences and finite element techniques, transmission line method, modal expansions, perturbation methods, and hybrid methods.

Where possible and appropriate, authors are required to provide statements of quantitative accuracy for measured and/or computed data. This issue is discussed in "Accuracy & Publication: Requiring, quantitative accuracy statements to accompany data," by E. K. Miller, *ACES Newsletter,* Vol. 9, No. 3, pp. 23-29, 1994, ISBN 1056-9170.

SUBMITTAL PROCEDURE

All submissions should be uploaded to ACES server through ACES web site (http://aces.ee.olemiss.edu) by using the upload button, journal section. Only pdf files are accepted for submission. The file size should not be larger than 5MB, otherwise permission from the Editor-in-Chief should be obtained first. Automated acknowledgment of the electronic submission, after the upload process is successfully completed, will be sent to the corresponding author only. It is the responsibility of the corresponding author to keep the remaining authors, if applicable, informed. Email submission is not accepted and will not be processed.

EDITORIAL REVIEW

In order to ensure an appropriate level of quality control, papers are peer reviewed. They are reviewed both for technical correctness and for adherence to the listed guidelines regarding information content and format.

PAPER FORMAT

Only camera-ready electronic files are accepted for publication. The term **"camera-ready" means that the material is neat, legible, reproducible, and in accordance with the final version format listed below.**

The following requirements are in effect for the final version of an ACES Journal paper:

1. The paper title should not be placed on a separate page.

The title, author(s), abstract, and (space permitting) beginning of the paper itself should all be on the first page. The title, author(s), and author affiliations should be centered (center-justified) on the first page. The title should be of font size 16 and bolded, the author names should be of font size 12 and bolded, and the author affiliation should be of font size 12 (regular font, neither italic nor bolded).

2. An abstract is required. The abstract should be a brief summary of the work described in the paper. It should state the computer codes, computational techniques, and applications discussed in the paper (as applicable) and should otherwise be usable by technical abstracting and indexing services. The word “Abstract” has to be placed at the left margin of the paper, and should be bolded and italic. It also should be followed by a hyphen (—) with the main text of the abstract starting on the same line.

3. All section titles have to be centered and all the title letters should be written in caps. The section titles need to be numbered using roman numbering (I. II. ….)

4. Either British English or American English spellings may be used, provided that each word is spelled consistently throughout the paper.

5. Internal consistency of references format should be maintained. As a guideline for authors, we recommend that references be given using numerical numbering in the body of the paper (with numerical listing of all references at the end of the paper). The first letter of the authors’ first name should be listed followed by a period, which in turn, followed by the authors’ complete last name. Use a coma (,) to separate between the authors’ names. Titles of papers or articles should be in quotation marks (“ ”), followed by the title of journal, which should be in italic font. The journal volume (vol.), issue number (no.), page numbering (pp.), month and year of publication should come after the journal title in the sequence listed here.

6. Internal consistency shall also be maintained for other elements of style, such as equation numbering. Equation numbers should be placed in parentheses at the right column margin. All symbols in any equation have to be defined before the equation appears or right immediately following the equation.

7. The use of SI units is strongly encouraged. English units may be used as secondary units (in parentheses).

8. Figures and tables should be formatted appropriately (centered within the column, side-by-side, etc.) on the page such that the presented data appears close to and after it is being referenced in the text. When including figures and tables, all care should be taken so that they will appear appropriately when printed in black and white. For better visibility of paper on computer screen, it is good to make color figures with different line styles for figures with multiple curves. Colors should also be tested to insure their ability to be distinguished after black and white printing. Avoid the use of large symbols with curves in a figure. It is always better to use different line styles such as solid, dotted, dashed, etc.

9. A figure caption should be located directly beneath the corresponding figure, and should be fully justified.

10. The intent and meaning of all text must be clear. For authors who are not masters of the English language, the ACES Editorial Staff will provide assistance with grammar (subject to clarity of intent and meaning). However, this may delay the scheduled publication date.

11. Unused space should be minimized. Sections and subsections should not normally begin on a new page.

ACES reserves the right to edit any uploaded material, however, this is not generally done. It is the author(s) responsibility to provide acceptable camera-ready files in pdf and MSWord formats. Incompatible or incomplete files will not be processed for publication, and authors will be requested to re-upload a revised acceptable version.

COPYRIGHTS AND RELEASES

Each primary author must execute the online copyright form and obtain a release from his/her organization vesting the copyright with ACES. Both the author(s) and affiliated organization(s) are allowed to use the copyrighted material freely for their own private purposes.

Permission is granted to quote short passages and reproduce figures and tables from and ACES Journal issue provided the source is cited. Copies of ACES Journal articles may be made in accordance with usage permitted by Sections 107 or 108 of the U.S. Copyright Law. This consent does not extend to other kinds of copying, such as for general distribution, for advertising or promotional purposes, for creating new collective works, or for resale. The reproduction of multiple copies and the use of articles or extracts for commercial purposes require the consent of the author and specific permission from ACES. Institutional members are allowed to copy any ACES Journal issue for their internal distribution only.

PUBLICATION CHARGES

All authors are allowed for 8 printed pages per paper without charge. Mandatory page charges of $75 a page apply to all pages in excess of 8 printed pages. Authors are entitled to one, free of charge, copy of the printed journal issue in which their paper was published. Additional reprints are available for $ 50. Requests for additional re-prints should be submitted to the managing editor or ACES Secretary.

Corresponding author is required to complete the online form for the over page charge payment right after the initial acceptance of the paper is conveyed to the corresponding author by email.

ACES Journal is abstracted in INSPEC, in Engineering Index, DTIC, Science Citation Index Expanded, the Research Alert, and to Current Contents/Engineering, Computing & Technology.